

Parametric Investigation of the Combustor-Turbine Interface

Leakage Geometry

by

Daniel G. Knost

Dissertation submitted to the Faculty of the
Virginia Polytechnic Institute and State University
in Partial Fulfillment of the Requirements for the Degree of

Doctor of Philosophy

in

Mechanical Engineering

Dr. Karen Thole, Chair

Dr. Kenneth Ball, Co-chair

Dr. Wing Ng

Dr. Andrew Duggleby

Dr. Mark Stremler

September 19, 2008

Blacksburg, Virginia

Keywords: gas turbine, endwall cooling, secondary flows, optimization

© 2008, Daniel G. Knost

Parametric Investigation of the Combustor-Turbine Interface

Leakage Geometry

by

Daniel G. Knost

Abstract

Engine development has been in the direction of increased turbine inlet temperatures to improve efficiency and power output. Secondary flows develop as a result of a near-wall pressure gradient in the stagnating flow approaching the inlet nozzle guide vane as well as a strong cross-passage gradient within the passage. These flow structures enhance heat transfer and convect hot core flow gases onto component surfaces. In modern engines it has become critical to cool component surfaces to extend part life.

Bypass leakage flow emerging from the slot between the combustor and turbine endwalls can be utilized for cooling purposes if properly designed. This study examines a three-dimensional slot geometry, scalloped to manipulated leakage flow distribution. Statistical techniques are used to decouple the effects of four geometric parameters and quantify the relative influence of each on endwall cooling levels and near-wall total pressure losses. The slot geometry is also optimized for robustness across a range of inlet conditions.

Average upstream distance to the slot is shown to dominate overall cooling levels with nominal slot width gaining influence at higher leakage flow rates. Scalloping amplitude is most influential to near-wall total pressure loss as formation of the horseshoe vortex and cross flow within the passage are affected. Scalloping phase alters local cooling levels as leakage injection is shifted laterally across the endwall.

Acknowledgments

I would like to take the opportunity to thank a few of the many people who have encouraged and supported me through this process. Much is owed to my advisor, Dr. Karen Thole, who has been my mentor for many years. I appreciate her bringing me into her research group and her willingness to extend a helping hand when I was in need. I would also like to thank Dr. Andrew Duggleby who took a particular interest in my research and academic growth. He spent much time explaining things to me and was always there to offer words of advice and encouragement. Many thanks as well to my remaining committee members, Dr. Ken Ball, Dr. Wing Ng, and Dr. Mark Stremmer who offered valuable advice and support. Without naming everyone, I would like to extend my sincere thanks to the many professors, lab-mates, and friends I have had during my time at Virginia Tech. I will always look back on my years in Blacksburg fondly. I would also like to extend the same gratitude to the professors, teachers, coaches and friends I have had at N.C. State and Providence Day School. They helped build the foundation for much that I have achieved.

On a personal note, I would like to thank my parents, Jack and Susan Knost, and my sister Melissa for their love, support, and sacrifices through the years. I love you all. I wish to give special recognition to my long-time companion Nicole. She has pushed, motivated, and supported me in pursuit of my dreams even when I didn't think they were possible. I could never have achieved so much without you and I love you. Finally, I would like to thank my beagle Katie who gives me unconditional love and enthusiasm. If only we all had someone to greet us with a tail wag and a kiss at the end of every day. I love you hound dog!

Table of Contents

Abstract	ii
Acknowledgments	iii
Table of Contents	iv
List of Tables	vii
List of Figures	ix
1 Introduction	1
1.1 Introduction	1
1.2 Dissertation Outline	3
2 Evaluating a Three-Dimensional Slot Design for the Combustor-Turbine Interface - <i>Journal of Turbomachinery</i>, in submission	4
Abstract	5
2.1 Introduction	5
2.2 Summary of Past Literature	5
2.3 Endwall Cooling Configuration	7
2.3.1 Three-Dimensional Slot Geometry	7
2.4 Computational Domain and Methods	9
2.4.1 Boundary Specification	9
2.4.2 Meshing and Grid Error Study	9
2.4.3 Solution Procedure	10
2.5 Inlet Conditions	11
2.6 Discussion of Results	12

2.6.1	Primary Effects of 3-D Parameters	12
2.7	Conclusions	15
	Nomenclature	15
	References	16
3	Parametric Investigation of the Combustor-Turbine Interface	
	Leakage Geometry: Part I - Thermal Optimization - <i>Journal of Turbomachinery</i>, in submission	17
	Abstract	18
3.1	Introduction	18
3.2	Literature Summary	18
3.3	Combustor-Turbine Junction Parameters	19
3.4	Computational Methods	20
3.5	Design of Experiments	21
3.6	Inlet Conditions	21
3.7	Performance Evaluation Metric	22
3.8	Discussion of Results	22
	3.8.1 Case #1 Inlet Conditions	23
	3.8.2 Case #2 Inlet Conditions	24
	3.8.3 Case #3 Inlet Conditions	25
	3.8.4 Signal-to-Noise Ratio Analysis	27
	3.8.5 Validation Simulations	28
3.9	Conclusions	28
	Nomenclature	30
	References	30
4	Parametric Investigation of the Combustor-Turbine Interface	
	Leakage Geometry: Part II - Secondary Flows - <i>Journal of</i>	

<i>Turbomachinery, in submission</i>	31
Abstract	32
4.1 Introduction	32
4.2 Relevant Past Studies	32
4.3 Three Dimensional Slot Geometry	33
4.4 Inlet Conditions	33
4.5 Performance Evaluation Metric	34
4.6 Discussion of Results	34
4.6.1 Case #1 Inlet Conditions	34
4.6.2 Case #2 Inlet Conditions	35
4.6.3 Case #3 Inlet Conditions	36
4.6.4 Signal-to-Noise Ratio	37
4.6.5 Validation Simulations	38
4.7 Secondary Flow and Thermal Fields	38
4.8 Conclusions	43
Nomenclature	43
References	44
5 Conclusions and Recommendations	45
5.1 Primary Effects of Three-Dimensional Parameters	45
5.2 Thermal Optimization	46
5.3 Secondary Flows	47
5.4 Recommendations for Further Investigation	47
Appendix A Performance Evaluation Metrics and Statistics	49
Appendix B Endwall Adiabatic Effectiveness Contours	54
Appendix C Secondary Flow Fields and Thermal Fields	76

List of Tables

2.1	Summary of Cooling Geometry Features	7
2.2	Typical Cell Counts for Geometry Features	10
2.3	Inlet Conditions for Various Cases	11
3.1	Trial Parameter Configurations	21
3.2	Inlet Conditions for Various Cases	21
3.3	Momentum Flux Ratios (I) for Case-Geometry Combinations . .	23
3.4	Parameter Levels for Factor Effects Plots	23
3.5	Estimated Thermal Contribution of Parameters at Optimal Con- figuration for Case #1 Inlet Conditions	24
3.6	Thermal ANOVA - Case #1	24
3.7	Expected Value of Optimal Configuration RMS Adiabatic Effec- tiveness for All Inlet Conditions	24
3.8	Estimated Thermal Contribution of Parameters at Optimal Con- figuration for Case #2 Inlet Conditions	25
3.9	Thermal ANOVA - Case #2	25
3.10	Estimated Thermal Contribution of Parameters at Optimal Con- figuration for Case #3 Inlet Conditions	26
3.11	Thermal ANOVA - Case #3	26
3.12	Estimated S/N contribution of parameters at optimal configuration	28
3.13	Thermal ANOVA - Signal-to-Noise Ratio	28
3.14	Performance Characteristics of Optimal Thermal Configuration from Validation Simulations	28
4.1	Inlet Conditions for Various Cases	33
4.2	Parameter Levels for Factor Effects Plots	34
4.3	Estimated Contribution of Parameters at Optimal Configuration for Case #1 Boundary Conditions	35

4.4	Expected Value of Optimal Configuration Total Pressure Loss Coefficient for All Inlet Conditions	35
4.5	Estimated Contribution of Parameters at Optimal Configuration for Case #2 Boundary Conditions	36
4.6	Estimated Contribution of Parameters at Optimal Configuration for Case #3 Boundary Conditions	37
4.7	Estimated Contribution of Optimal Parameter Levels to S/N . .	38
4.8	Performance Characteristics of Optimal Aerodynamic Configu- ration from Validation Simulations	38
4.9	Baseline and Optimized Slot Configurations	38

List of Figures

1.1	Endwall secondary flow model for a turbulent boundary layer presented by Langston. The horseshoe vortex develops at the leading edge and the passage vortex results from strong cross-passage flows along the endwall.	2
2.1	The baseline cooling configuration featured a two-dimensional slot and 51 film-cooling holes.	7
2.2	A three-dimensional slot with variable wave amplitude and phase, average width, and upstream distance was investigated.	8
2.3	Total open area of the slot is independent of waveform phase and amplitude.	8
2.4	The computational domain featured a single passage modeled to midspan.	9
2.5	Each grid was sampled uniformly throughout the domain for error evaluation.	10
2.6	Grid error was evaluated for convergence and uniformity with increasing cell count.	10
2.7	Normalized inlet profiles.	11
2.8	Moving the slot upstream yields more uniform injection but reduces effectiveness levels within the passage. All configurations are shown at momentum flux ratio $I=0.03$ for the case #1 inlet conditions.	12
2.9	Waveform amplitude concentrates coolant injection while phase shifts coverage area laterally ($I=0.03$, $A=0.9W$, $x/C_{ax} = -1.0$).	13
2.10	Pitchwise adiabatic effectiveness levels at $x/C_{ax} = -0.25$ (top) and slot geometry profiles (bottom) for $I=0.03$ cases.	14

2.11	Contracting the slot improves coverage area at the leading edge and within the passage for a fixed leakage flow rate ($A=0.5W$, $x/C_{ax} = -0.71$, $\dot{m}_c=1.0\%\dot{m}_{ex}$).	15
3.1	The three-dimensional slot was flush and defined by four parameters: amplitude, phase, width, and upstream distance.	19
3.2	Grid error was reduced as cell resolution increased.	20
3.3	Three inlet velocity profiles were simulated including a turbulent boundary layer, uniform profile, and a near-wall peaked profile. .	22
3.4	Area averages were computed from immediately upstream of the leading row of film-cooling holes to 50% axial chord within the passage.	22
3.5	Mean parameter thermal effects for case #1.	23
3.6	Mean parameter thermal effects for case #2.	25
3.7	Mean parameter thermal effects for case #3.	26
3.8	Parameter effects on signal-to-noise ratio.	27
3.9	Contours of adiabatic effectiveness for the baseline, two-dimensional configuration at all cases.	29
3.10	Contours of adiabatic effectiveness for the optimal thermal configuration at all cases.	29
4.1	Four parameters, amplitude, phase, average width, and upstream distance, were investigated.	33
4.2	Three inlet total pressure profiles were simulated.	34
4.3	Mean parameter aerodynamic effects for case #1.	34
4.4	Mean parameter aerodynamic effects for case #2.	35
4.5	Mean parameter aerodynamic effects for case #3.	36
4.6	Mean parameter signal-to-noise ratios for all inlet condition cases.	37

4.7	Thermal and secondary flow fields in the stagnation plane for case #1 inlet conditions.	40
4.8	Thermal and secondary flow fields in plane SS2 for case #1 inlet conditions.	40
4.9	Thermal and secondary flow fields the stagnation plane for case #2 inlet conditions.	41
4.10	Thermal and secondary flow fields in plane SS2 for case #2 inlet conditions.	41
4.11	Thermal and secondary flow fields in the stagnation plane for case #3 inlet conditions.	42
4.12	Thermal and secondary flow fields in plane SS2 for case #3 inlet conditions.	42

1 Introduction

1.1 Introduction

Combustion turbine engines have become an integral part of our daily lives propelling aircraft, tanks, and large naval ships and providing peaking power on the electrical grid. The technology of the turbine engine must continue to grow to provide more power at a higher efficiency in today's more environmentally conscious, yet energy thirsty, world. The power output and efficiency of a turbine engine are dependent upon the temperature of the fluid entering the turbine and as such engine development has been towards increasing turbine inlet temperatures.

As turbine inlet temperatures have risen to levels exceeding the metallurgical limits of the machine, it has become necessary to provide cooling to components to extend operating life. Commonly high pressure gas is extracted from the compressor, bypasses the combustor, and is then injected through discrete holes in component surfaces known as film-cooling holes, or channeled through internal passages.

Turbines are typically manufactured as many components and then assembled to form the turbine disk. The manufacturing process results in inherent gaps between components. Examples of these gaps are the combustor-turbine interface and the junction between adjacent airfoil components in the turbine disk. The gaps typically have a seal but are always supplied with high pressure bypass gas to prevent ingestion of hot mainstream gases into the wheel house. Resulting gas leakage rates can be upwards of 5% of the core flow. If properly designed the high pressure gas emerging from these leakage paths might be used to effectively cool component surfaces.

As the working fluid approaches the first stage stator, used to accelerate and direct the flow into the first stage rotor bucket, secondary flows develop.

A classic secondary flow model for a turbulent boundary layer, presented by Langston [2.1], is shown in Figure 1.1. A vortex develops at the vane leading edge with legs extending into the passage around both the pressure and suction sides. This structure is called the horseshoe vortex. Within the passage another vortex, known as the passage vortex, develops because of strong cross-passage currents generated by the sharp pressure gradient across the passage. These secondary flows enhance heat transfer and can collect the coolant layer developed by film-cooling and leakage flows and entrain hot mainstream gases convecting them down onto the metal surfaces leading to component burnout. Additionally secondary flows generate aerodynamic losses reducing engine efficiency and work output.

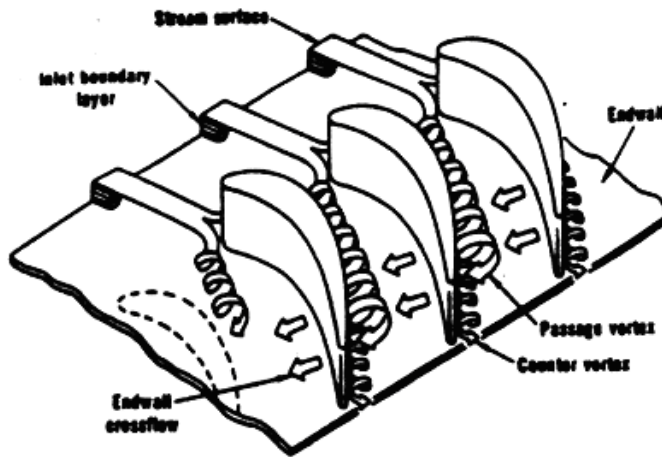


Figure 1.1: Endwall secondary flow model for a turbulent boundary layer presented by Langston. The horseshoe vortex develops at the leading edge and the passage vortex results from strong cross-passage flows along the endwall.

The focus of this work was to understand how leakage flow from the combustor-turbine interface could be most effectively used to cool the endwall surface. The influence on secondary flow development and total pressure loss in the near-wall region was also investigated.

1.2 Dissertation Outline

This dissertation is presented as a series of three papers, each of which is to be submitted to the ASME International Gas Turbine Institute. Each paper is intended as a stand alone document complete with abstract, introduction, literature review, conclusions, and references.

The first paper, listed as chapter two, presents a detailed description of a scalloped slot geometry. The computational modeling techniques used in this work are discussed as well as a summary of the grid error study. The primary effects of four parameters defining the slot geometry are illustrated with sample configurations.

Chapter three is the first of a two part series where statistical methods were employed to quantify the effect of the slot geometry parameters on endwall cooling levels. The mean effects of each parameter are estimated and analysis of variance is used to identify those parameters which have significant influence on endwall cooling levels. Signal-to-noise ratio analysis is used to select an optimal configuration based upon robustness. Slot leakage coverage and cooling levels are compared to a conventional two-dimensional slot.

The statistical techniques discussed in the second paper are utilized in the third paper to evaluate the influence of slot geometry on secondary flows. An optimal slot configuration is selected to minimize total pressure losses through the passage in the near-wall region. Secondary flow fields and thermal fields are compared in the stagnation plane and a plane near the passage throat for the aerodynamically optimized configuration as well as the baseline and thermally optimized slot geometries.

Finally, the conclusions from each paper in the series are summarized in chapter five. Suggestions are also given for further investigation .

2 Evaluating a Three-Dimensional Slot Design for the
Combustor-Turbine Interface - *Journal of Turbomachinery*, in
submission

GT2009-60168

EVALUATING A THREE-DIMENSIONAL SLOT DESIGN FOR THE COMBUSTOR-TURBINE INTERFACE

D.G. Knost*

Mechanical Engineering
Virginia Tech
Blacksburg, Virginia 24060

K.A. Thole

Mechanical and Nuclear Engineering
The Pennsylvania State University
State College, Pennsylvania 16802

A. Duggleby

Mechanical Engineering
Texas A&M University
College Station, Texas 77843

ABSTRACT

As turbine inlet temperatures push ever higher in an attempt to improve efficiency and power, it has become critical to cool component surfaces. One surface that is particularly difficult to treat because of the complex flow field that surrounds it is the nozzle guide vane endwall. Past studies have indicated that leakage bypass flow emerging from the combustor-turbine junction may be effectively harnessed for cooling purposes. When combined with endwall film-coolant injection, component service life may be significantly extended.

This paper presents results from a computational study investigating a three-dimensional slot geometry at the combustor-turbine interface. The downstream edge of the slot was scalloped using a simple periodic function intended to enhance thermal benefit to the endwall by manipulating coolant distribution. Effects of varying the slot geometry amplitude and phase were investigated along with the slot nominal width and upstream distance from the vane. Initial results indicate dramatic effects can be realized depending upon the scalloping used.

2.1 INTRODUCTION

Over the course of turbine technology development, inlet temperatures have increased well in excess of component thermal limits in the pursuit of improved performance and efficiency. Typically, relatively cool air is bled off of the compressor discharge, bypassing the combustor, and is used in internal cooling passages as well as injected through holes in component surfaces. Some bypass leakage flow escapes through gaps between components as a result of high pressure necessary to seal the wheelhouse and prevent hot core flow ingestion. Past studies demonstrate that leakage flow through the combustor-turbine endwall

junction is useful for cooling, providing a buffer between the vane endwall surface and the hot combustor exit flow.

For traditional two-dimensional slots, the leakage flow emerges primarily between the airfoils and is typically swept toward the suction side of the passage leaving uncooled regions at the vane leading edge and along the pressure side. This paper introduces a three-dimensional slot geometry intended to influence leakage flow discharge and alter coolant coverage area and effectiveness. Effects of varying several geometric parameters are explored and results are related to a conventional, two-dimensional configuration. This paper precedes a statistical analysis and optimization of the parameters and highlights first order effects.

2.2 SUMMARY OF PAST LITERATURE

The endwall flowfield of a first stage turbine vane consists of unique features that contribute to high heat transfer and aerodynamic losses. Although there are slight differences in detail, flowfield studies by Langston et al. [1], Sharma and Butler [2], Goldstein and Spores [3], and others concur on the dominant structures in the endwall region for an approach flow that is uniform with a two-dimensional boundary layer. The incoming boundary layer on the endwall rolls up into a horseshoe vortex at the leading edge of the vane. The horseshoe vortex splits into suction and pressure side legs where the pressure side leg develops into a passage vortex as a result of the strong cross passage pressure gradient. These vortical structures and their interaction (generally termed "secondary flows") are sources of aerodynamic loss in the cascade; furthermore they sweep coolant from the endwall and increase endwall heat transfer coefficients.

Several studies have measured endwall heat transfer as a result of injection from a two-dimensional, flush slot upstream of the vane. Blair [4] measured adiabatic effectiveness levels and

*Address all correspondence to this author.

heat transfer coefficients for a range of blowing ratios through a flush slot placed just upstream of the leading edges of a single passage channel. One of the key findings was that the endwall adiabatic effectiveness distributions showed extreme variations across the vane gap. Much of the coolant was swept across the endwall toward the suction side corner resulting in reduced coolant near the pressure side. As the blowing ratio was increased, he found that the extent of the coolant coverage also increased. Measured heat transfer coefficients were similar between no slot and slot injection cases. In a later study by Granser and Schulenberg [5] similar adiabatic effectiveness results were reported with higher values occurring near the suction side of the vane.

A series of experiments report the results of various injection schemes upstream of a nozzle guide vane with a contoured endwall (Burd and Simon [6], Burd et al. [7], Oke, et al. [8, 9], and Oke and Simon [10]). In the studies presented by Burd and Simon [6], Burd et al. [7] and Oke, et al. [8] coolant was injected from an interrupted, flush slot that was inclined at 45° just upstream of their vane. Similar to others, they found that most of the slot coolant was directed toward the suction side at low slot flow conditions. As they increased the percentage of slot flow to 3.2% of the exit flow, measurements indicated increased coverage between the airfoils. In contrast, the study by Oke et al. [9] used a double row of film-cooling holes that were aligned with the flow direction and inclined at 45° with respect to the surface while maintaining nearly the same optimum 3% bleed flow of their previously described studies. They found that the jets lifted off the surface producing more mixing thereby resulting in a poorer thermal performance than the single slot. Oke and Simon [10] presented results from two upstream film-cooling rows with sections blocked to promote discharge in certain areas. They showed a vortex formed near the edge of the upstream film hole and moved toward the pressure side. The vortex was strengthened by increasing mass flow rate, impacting the pressure side of the vane farther upstream. An upstream hole configuration featuring a linear taper on the pressure and suction sides toward the center of the passage provided coolant to the leading edge at all blowing conditions while injection from a single row of holes with a linear taper on the suction side improved coolant supply to the pressure side at all blowing conditions. Pressure side coverage was higher than for the suction side at high mass flow ratios.

Roy et al. [11] compared their experimental measurements and computational predictions for a flush cooling slot that extended over only a portion of the pitch directly in front of the vane stagnation. Contrary to the previously discussed studies, their adiabatic effectiveness measurements showed that the coolant migrated toward the pressure side of the vane. Measurements indicated reduced values of local heat transfer coefficients at the leading edge when slot cooling was present relative to no slot cooling.

Lynch and Thole [12] presented measurements of adiabatic effectiveness and endwall shear stress as well as heat transfer coefficients for a flush slot with the vane geometry used in this work. The slot was moved upstream and contracted simulating

axial thermal expansion. Results showed that coolant coverage area was similar for a fixed coolant mass flow rate at varying slot axial locations as the coverage area was dictated by secondary flows. However effectiveness levels within the passage were lowered for the slot further upstream as the coolant had longer to mix with the hot mainstream gases. Increasing coolant mass flow rate for a given slot width improved adiabatic effectiveness levels but also slightly increased heat transfer coefficients. More uniform coolant injection was also achieved with increased blowing as coolant momentum flux increased. This effect was amplified by reducing the slot width while maintaining a fixed coolant mass flow rate and resulted in broader coolant coverage within the passage. Overall, results indicated that for low slot momentum endwall secondary flows dictated coverage area while high momentum slot flow penetrated significantly downstream of the endwall separation line. Heat transfer coefficient augmentation was less severe for the contracted slot when compared with the nominal geometry. Net heat flux to the endwall was also reduced for the contracted slot compared to the nominal slot injecting at the same rate.

Colban et al. [13, 14] reported flow field and endwall effectiveness contours for a backward-facing slot with several different coolant exit conditions. Their measurements identified the presence of a tertiary vortex that developed in the vane passage due to a peaked total pressure profile in the near-wall region. For all of the conditions simulated, the effectiveness contours indicated the coolant from the slot was swept towards the suction surface.

Some studies have combined an upstream slot with film-cooling holes in the downstream endwall. Kost and Nicklas [15] and Nicklas [16] presented aerodynamic, heat transfer, and film-cooling effectiveness measurements from a transonic cascade. One of the most interesting results from this study was that they found for the slot flow alone, which was 1.3% of the passage mass flow, the horseshoe vortex became more intense. This increase in intensity resulted in the slot coolant being moved off of the endwall surface and heat transfer coefficients that were over three times that measured for no slot flow injection. They attributed the strengthening of the horseshoe vortex to the fact that for injection with no slot the boundary layer was already separated with fluid being turned away from the endwall at the injection location $0.2C_{ax}$. Given that the slot had a normal component of velocity, injection at this location promoted the separation and enhanced the vortex. Their adiabatic effectiveness measurements showed higher values near the suction side of the vane due to the slot coolant migration. Kost and Mullaert [17] studied the same airfoil geometry, but moved the flush slot to $0.3C_{ax}$ upstream of the vane. They found for this configuration that slot flow stayed closer to the endwall and provided better cooling than flow from the slot located at $0.2C_{ax}$ upstream of the vane.

Knost and Thole [18, 19] presented computational and experimental results for combined slot flow and passage film-cooling. Increased blowing from the slot had a strong effect on the near-wall streamlines altering direction of injection from the film-cooling holes. This effect was particularly pronounced near

Table 2.1. Summary of Cooling Geometry Features

Feature	Scale 9x
Slot width [cm]	1.48
Slot length to width	1.8
Slot injection angle	45°
Upstream slot location	$-0.42C_{ax}$
Cooling hole diam [cm]	0.46
Cooling hole L/D	8.3
Hole injection angle	30°
p/d for leading edge holes	4/3
p/d for passage holes	3

the stagnation point and along the upstream portion of the pressure side. Higher flow turning was also exhibited within the passage.

Cardwell et al. [20] showed that coolant coverage area from the upstream slot leakage was dictated by coolant-to-mainstream momentum flux ratio with higher momentum flux leading to more uniform slot injection and coverage at the leading edge and along the pressure side. Local adiabatic effectiveness levels were demonstrated to be a strong function of coolant-to-mainstream mass flow ratio with adiabatic effectiveness levels improving at higher blowing rates.

While many have studied the effects of varying inlet conditions from fixed geometries, few have investigated varying the slot leakage geometry to manipulate coolant coverage and effectiveness. This work seeks to explore the possibilities for affecting leakage flow by varying parameters of a three-dimensional leakage geometry.

2.3 ENDWALL COOLING CONFIGURATION

The baseline endwall cooling configuration for this study, outlined in Table 2.1 and shown in Figure 2.1, is the same as presented by Knost and Thole [18]. It was developed with input from industrial partners. The scheme featured a flush upstream slot, simulating bypass leakage flow through the junction between the combustor and turbine endwalls, and 51 film-cooling holes. The original slot was two-dimensional and injected downstream in the axial direction at an inclination angle of 45 degrees with respect to the endwall. The slot centerline was stationed 0.42 axial chords upstream of the vane dynamic stagnation location to accommodate variations in the proposed new geometry without interfering with the film-cooling pattern.

Film-cooling holes were positioned along the vane endwall at the leading edge and in a pitchwise row upstream of the vane passage. Holes were arranged in axial rows within the passage along the vane pressure side and near the shoulder of the suction side. Holes at the leading edge and within the passage were

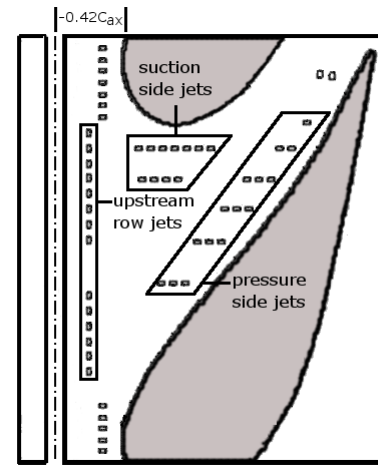


Figure 2.1. The baseline cooling configuration featured a two-dimensional slot and 51 film-cooling holes.

spaced three hole diameters apart and injected downstream in the axial direction, while holes in the upstream row were spaced four hole diameters apart and directed toward the suction side injecting at 90 degrees with respect to the flow inlet direction. Two film-cooling holes near the pressure side trailing edge were directed at a compound angle of 45 degrees with respect to the axial direction. All film-cooling holes injected at a 30 degree inclination with respect to the endwall.

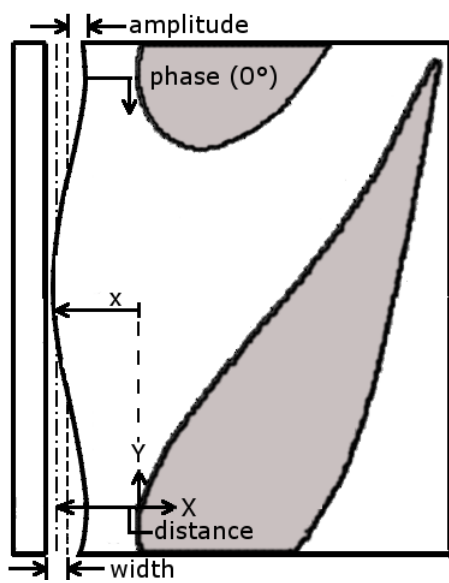
2.3.1 Three-Dimensional Slot Geometry

Traditionally the combustor-turbine slot geometry in published studies has been two-dimensional with the downstream edge of the combustor endwall and the upstream edge of the vane endwall flush and parallel. A three-dimensional combustor-turbine slot was investigated in this study utilizing a scalloped downstream edge intended to provide variable leakage flow metering across the vane pitch. As defined in Eq. 2.1 and illustrated in Figure 2.2(a), the downstream edge of the slot featured a cosine wave with four parameters: waveform amplitude, waveform phase, average slot width, and slot centerline upstream distance.

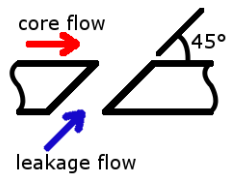
$$x = A \cos(2\pi y/P + \phi) + \text{upstream dist} + \text{width}/2 \quad (2.1)$$

A cosine was selected because of its smooth and continuous properties. As with the baseline geometry, the three-dimensional slot was flush and injected downstream at 45 degrees with respect to the endwall, illustrated in Figure 2.2(b). The film-cooling pattern remained unchanged from the baseline configuration and was included because film-holes are generally present within the passage and have been shown previously to have significant impact on endwall coolant distribution.

As mentioned in the literature review, previous studies have shown coolant from the slot to inject primarily near the center of the passage with little coolant emerging upstream of the



(a) plan view



(b) slot side view

Figure 2.2. A three-dimensional slot with variable wave amplitude and phase, average width, and upstream distance was investigated.

vane stagnation. This leads to over-cooling in the center and under-cooling at the leading edge and on the pressure side of the passage. The slot waveform amplitude was intended to restrict coolant mass flow in areas of low pressure through reduced flow area to moderate over-cooling. Additionally, it was thought that concentrating the slot open area near typical regions of low cooling would increase leakage flow over portions of the upstream endwall that are more difficult to cool. The waveform amplitude was also expected to have some effect on secondary flow development as less slot injection in low pressure areas may reduce the sink effect influence of the slot flow seen in previous studies [19] while more coolant injection should energize the boundary layer in areas where the flow stagnates. Amplitude was measured from the average upstream edge of the vane endwall, indicated by a dash-dash line in Figure 2.2(a), and expressed as a fraction of the average slot width.

The phase of the slot waveform was also investigated. Varying the waveform phase was expected to alter the leakage flow distribution shifting the slot coolant laterally across the endwall. Shifting phase was also expected to have some effect on secondary flow development as blowing non-uniformity was adjusted across the vane pitch. Phase was measured from a zero degree reference directly upstream of the vane stagnation.

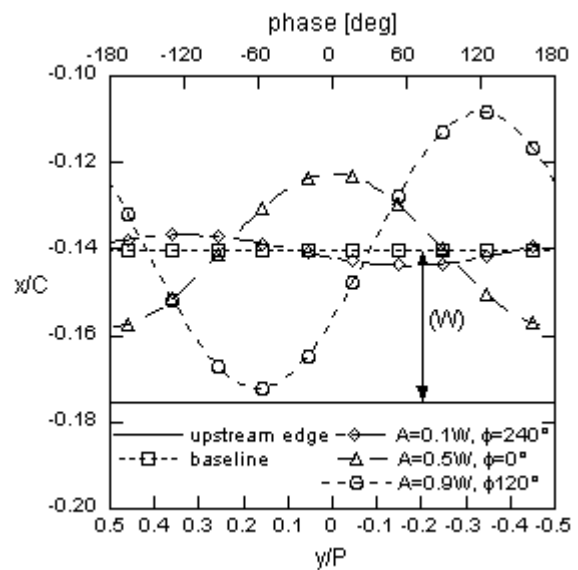


Figure 2.3. Total open area of the slot is independent of waveform phase and amplitude.

Average slot width was varied as a global means of altering the coolant momentum flux ratio. The average slot width was computed as the distance between the upstream edge of the leakage geometry and the centerline of the downstream edge formed by the waveform, indicated by a dash-dash line in Figure 2.2(a). As shown in Figure 2.3, amplitude and phase have no net effect on total open area as the positive and negative areas about the waveform centerline cancel. Cardwell et al. [20] showed that varying slot width for a fixed coolant mass flow rate affected coolant coverage as higher momentum leakage flow penetrated beyond the endwall separation line of the horseshoe vortex yielding more uniform coolant coverage. A narrower average slot width with an open area concentration near the leading edge was expected to improve coolant coverage in difficult areas at the leading edge and along the pressure side for a fixed leakage rate and scale cooling levels for a fixed momentum flux ratio.

The final parameter under investigation was upstream distance to the nominal slot centerline. Upstream distance was measured from the axial location of the stagnation point to the centerline between the slot upstream edge and average downstream edge. The upstream distance location is shown as a dash-dot line in Figure 2.2(a). Previous studies indicated that coolant exits the slot in a non-uniform manner. This occurs because of the varying static pressure distribution over the endwall due to the presence of the downstream vanes. Lynch and Thole [12] showed that moving the slot further upstream improved slot coolant injection uniformity as the influence of the vane was reduced, but cooling levels within the passage were diminished as the coolant had longer to mix with the hot core flow. Varying upstream slot distance was intended to balance these effects to achieve coverage uniformity and adequate cooling levels.

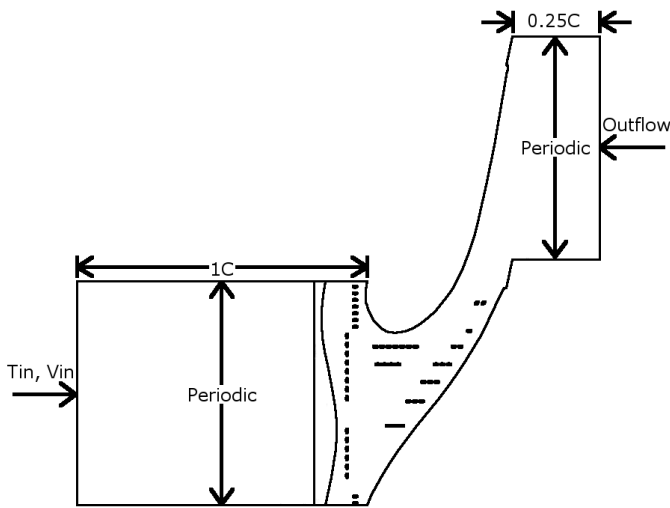


Figure 2.4. The computational domain featured a single passage modeled to midspan.

2.4 COMPUTATIONAL DOMAIN AND METHODS

A plan view of the computational domain for this study is shown in Figure 2.4. The vane used was a commercial nozzle guide vane originally described by Radomsky and Thole [21]. It was two-dimensional with the midspan cross section modeled along the entire span. The vane and all other geometries in this study were scaled up by a factor of nine to allow comparison of results with any data acquired in the large-scale wind tunnel test section previously described by Knost and Thole [19]. The exit Reynolds number based on chord was matched to the engine.

2.4.1 Boundary Specification

The vane was divided at the dynamic stagnation location and trailing edge with a single passage modeled between. A velocity inlet boundary was specified one chord upstream of the passage. The domain was extended $0.1C$ beyond the trailing edge in the flow exit direction followed by an axial length of $0.25C$ to an outflow boundary. These locations were determined by Hermanson and Thole [22] to be free of pressure effects from the vane. Periodic boundary conditions were specified in the stagnation plane and beyond the trailing edge. The passage was modeled to midspan with an imposed symmetry condition to allow greater cell resolution within the domain. The slot and film-cooling holes were supplied from below by separate plenums with coolant mass flow rate and temperature imposed at mass flow inlets. All walls were modeled as adiabatic with no slip except for the vertical plenum walls which were shear free. This was done to avoid viscous effects in the corners of the plenums.

2.4.2 Meshing and Grid Error Study

The solution domain was divided into multiple volumes to improve meshing ease. The mesh was a hybrid scheme incorporating structured hexahedral bricks, unstructured hexahedral

bricks, pyramids, and tetrahedrons. Structured bricks were used from the velocity inlet to $0.3C$ upstream of the slot upstream edge and in the majority of the axial extension downstream of the trailing edge. This was done to conserve elements in areas where the flow was expected to be less complex. The passage was split at 30% span with unstructured bricks above this station and tetrahedrons below. The 30% span location was selected because it allowed an ample buffer above the secondary flows which were expected to reside below 15% span based upon previous calculations and measurements. This strategy allowed much higher cell density in the lower portion of the passage with a more efficient hexahedral structure near midspan where the flow was expected to be largely two-dimensional. The slot and film-cooling holes were meshed individually with a minimum of approximately ten cells across any face where flow injected into the main passage. In addition the angle between outward facing normals of any two adjacent cells was limited to less than five degrees and the cell expansion rate was limited to ten percent between adjacent cells.

Five grids were initially evaluated to determine necessary mesh resolution in different parts of the passage. These grids were approximately 7 million, 8.7 million, 9.1 million, 15.8 million, and 22.8 million cells respectively. The 22.8 million cell grid served as a reference for error evaluation of the other four grids. The 8.7 million cell grid was adapted from the 7.0 million cell grid based upon computed values of y^+ . The time required for this operation was prohibitive while the average error was still greater than for the similarly sized 9.1 million cell grid. This indicated that grid adaption was computationally inefficient compared to generating an initially finer grid.

Each grid was uniformly sampled in three dimensions at a spacing of approximately two film-cooling hole diameters as shown in Figure 2.5. The error at each location in temperature, pressure, velocity, and shear stress was computed with respect to the 22.8 million cell reference grid and the magnitude summed over the entire domain. The total error was then averaged and normalized to allow evaluation.

The thermal error, presented as average normalized temperature error, and the velocity component and magnitude errors are shown in Figure 2.6(a). It is seen that total grid error decreased as cell count (resolution) increased. Also, as stated previously, error was reduced more for the initially finer 9.1 million cell grid than for the similarly sized 8.7 million cell grid which was solution adapted from the coarsest grid. The average thermal error at a single sample location for the finest grid was less than 0.2% of the driving temperature difference ($\partial\eta, \partial\theta < 0.002$). The average velocity magnitude error was 2.5% of the inlet velocity while the z-component velocity errors were approximately an order of magnitude smaller than the x and y-component errors.

Average error magnitude was also computed in each spanwise sample plane to evaluate cell growth rate near the endwall as well as the division between tetrahedral and hexahedral cells at $z/S = 0.3$. The spanwise error summary for velocity magnitude is shown in Figure 2.6(b). Upon examination of the 7.0 million and 8.7 million cell grids it is clear that grid adaption occurred only below 10% span, where the complex secondary

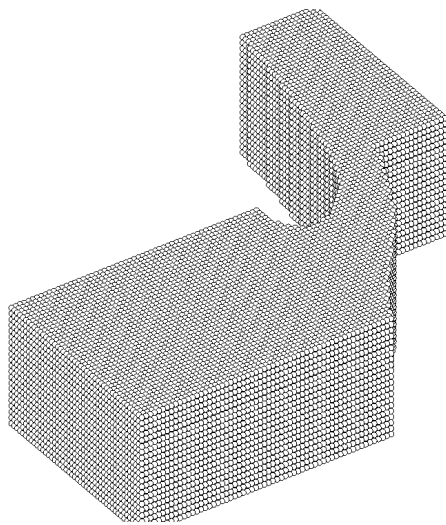


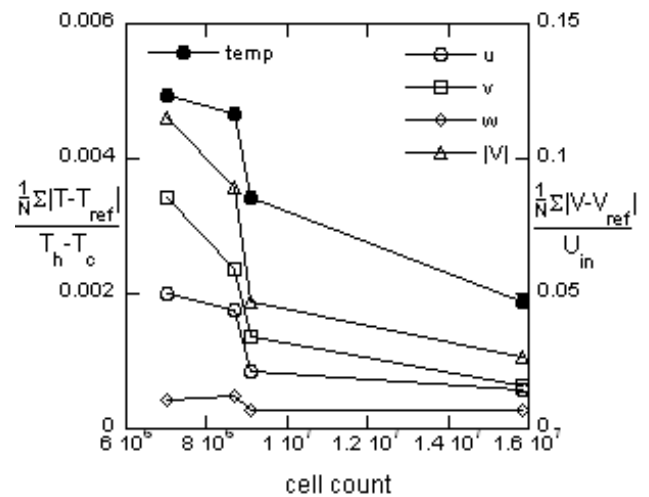
Figure 2.5. Each grid was sampled uniformly throughout the domain for error evaluation.

Table 2.2. Typical Cell Counts for Geometry Features

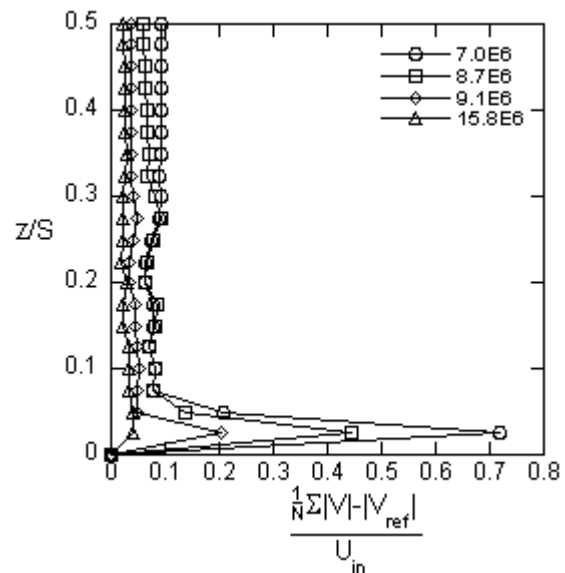
Feature	Cells
Inlet	38,000
Outlet	16,000
Film-cooling hole	45,000
Slot	300,000
Passage $z/S > 0.3$	33,000
Passage $z/S < 0.3$	8,000,000
Total	15,000,000

flows and coolant injection reside, and above 30% span where the cell type transition occurred. Initial grid refinement to 9.1 million cells showed less error at all spanwise locations than the solution adapted grid but still an error spike at 2.5%span. This location typically coincides with the core of the secondary flows. Finally increasing the grid size to 15.8 million cells further reduced error at all spanwise locations and yielded a more uniform error distribution with an average velocity magnitude error of approximately 3% of the inlet velocity at all spanwise stations.

Error reduction was evaluated between meshes. The scheme yielding the greatest relative gains and uniformity was selected for each sub-volume within the domain. Nominal cell counts for various features of the resulting production run grids are listed in Table 2.2. Production grids typically ranged from 14.5 to 16 million cells and fit comfortably on computing clusters with 32 GB of RAM.



(a) total error



(b) spanwise error

Figure 2.6. Grid error was evaluated for convergence and uniformity with increasing cell count.

2.4.3 Solution Procedure

The incompressible Reynolds-Averaged Navier-Stokes (RANS), energy, and turbulence equations were computed using the Fluent 6 pressure-based segregated solver. In this approach the momentum and pressure correction (continuity) equations are solved sequentially. The mass fluxes, pressure, and velocity fields are then updated from the pressure correction and additional scalar quantities such as energy and turbulence are computed. The segregated approach is memory efficient, since the segregated equations need only be stored one at a time, however solution convergence is relatively slow [23].

Table 2.3. Inlet Conditions for Various Cases

Inlet condition	Case #1	Case #2	Case #3
Inlet profile	Turb BL	Uniform	Peaked
Slot leakage rate	$0.5\% \dot{m}_{ex}$	$0.75\% \dot{m}_{ex}$	$1.0\% \dot{m}_{ex}$
Film-coolant rate	$0.5\% \dot{m}_{ex}$	$0.5\% \dot{m}_{ex}$	$0.5\% \dot{m}_{ex}$

The RNG $k - \epsilon$ turbulence model was utilized with enhanced wall functions. The RNG $k - \epsilon$ turbulence model exhibits improved performance in comparison to the standard $k - \epsilon$ model for complex shear flows and flows with high strain rates, swirl, and separation. Hermanson and Thole [22] showed good prediction of secondary flows with the RNG $k - \epsilon$ turbulence model. The enhanced wall function option in Fluent employs a two-layer zonal model in the near-wall region where the laminar sublayer is resolved directly if grid resolution is fine enough ($y^+ \approx 1$) and a blending function is applied in the buffer layer [23].

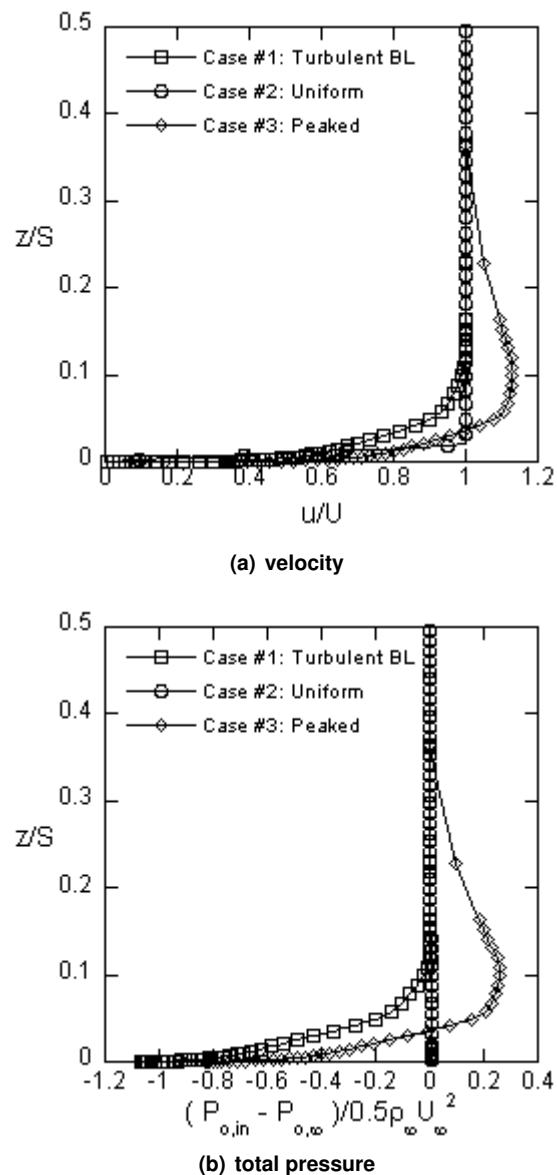
The solution domain was initialized in three zones (front half of the passage, rear half of the passage, and plenums) and the laminar RANS equations were computed with first order discretization for 150 iterations to promote stability early in the solution procedure. The energy and turbulence equations were then included for an additional 150 iterations. Finally all equations were upgraded to second order discretization and computed for 1100 iterations. Solution residuals, area-averaged endwall temperature, mass-averaged total pressure at the inlet and outlet, lift, and drag coefficients were monitored at each iteration to evaluate solution convergence. Typical solution times ranged from 24-30 hours on ten 2.0GHz 64bit processors.

2.5 INLET CONDITIONS

The baseline and three-dimensional slot geometries were evaluated for three different cases. The inlet conditions for the cases were distinguished by the inlet velocity and total pressure profiles as well as by the slot leakage flow rate. The film-coolant flow rate was fixed at 0.5% of the total exit mass flow rate to avoid confounding with variations in the leakage flow. The inlet temperature for all cases was uniform to insure changes in cooling levels were resultant only from variations in slot flow rate and distribution. The inlet conditions for these three cases are listed in Table 2.3. The cases were intended to encompass a wide range of inlet profiles and leakage flow rates.

The normalized inlet velocity and total pressure profiles for each case are shown in Figures 2.7(a) and 2.7(b). Hermanson and Thole [22] showed that secondary flow development was highly sensitive to the total pressure profile exiting the combustor. The turbulent inlet boundary layer they computed was selected for case #1 as the total pressure deficit in the boundary layer was identified as the primary factor in development of the horseshoe vortex. Additionally, the slot leakage rate was set at the lowest value under investigation, 0.5% of the total exit mass flow rate.

A uniform inlet velocity profile for case #2 corresponded to

**Figure 2.7. Normalized inlet profiles**

the inlet profile originally studied by Knost and Thole [18, 19]. When combined with a uniform inlet temperature this yielded a blunt total pressure profile at the domain inlet. Slot leakage was fixed at a moderate rate of 0.75% of the total exit mass flow rate.

Hermanson and Thole [22] argued that the turbulent boundary layer and uniform inlet temperature were not necessarily representative of combustor exit profiles during operation because of film-cooling and dilution blowing in the combustor. They proposed a total pressure profile which was peaked near the endwall as a result of much cooler fluid in the near-wall region. This led to a flow split part way up the span and a counter rotation of the flow above this station. Because it was undesirable in this study to introduce variations in coolant blowing anywhere but at the slot leakage geometry, a peaked near-wall velocity profile

was computed to match the peaked total pressure profile of Hermannson and Thole. This peaked profile was selected as the inlet condition for case #3 and combined with 1.0% \dot{m}_{ex} slot leakage, the highest value investigated.

Mass-averaged coolant momentum flux ratio for the slot coolant was determined by the leakage flow rate for each case and the average slot width. Average momentum flux ratios were maintained while varying local values by manipulating scallop geometry. Mass-averaged momentum flux ratio could be matched between configurations while coolant flow rate varied by altering both average slot width and leakage rate. Varying only average width illuminated effects of altering momentum flux ratio for a fixed leakage rate.

2.6 DISCUSSION OF RESULTS

This paper supports a statistical study of the thermal and aerodynamic effects of the four slot parameters illustrated in Figure 2.2 [24,25]. Selected cases are presented to illustrate primary effects of these parameters. Among these effects are:

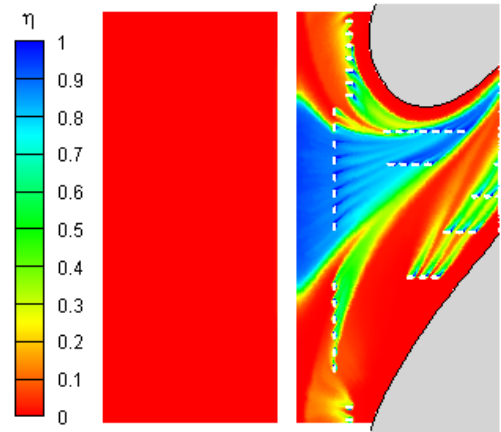
- slot upstream distance affects leakage injection uniformity and cooling levels within the passage
- increasing waveform amplitude concentrates coolant injection location while shifting waveform phase shifts injection location
- contracting average slot width improves coolant coverage uniformity

2.6.1 Primary Effects of 3-D Slot Parameters

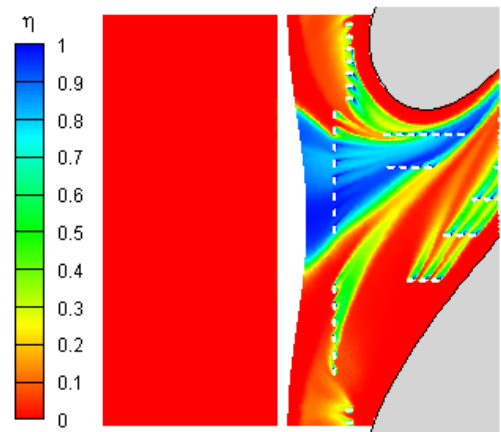
The baseline slot was a conventional, two-dimensional geometry injecting flow axially downstream at 45 degrees with respect to the endwall surface. Contours of adiabatic effectiveness for the baseline slot with the inlet conditions specified by case #1, consisting of 0.5% \dot{m}_{ex} slot leakage flow and a turbulent boundary layer at the inlet, are shown in Figure 2.8. Adiabatic effectiveness is defined such that a value of unity indicates perfect cooling while a value of zero indicates no coolant present.

Coolant emerges from the slot in the center of the passage with no leakage flow present upstream of the vanes for the baseline geometry, as shown in Figure 2.8(a). On the suction side, the leading edge film-cooling jets are swept around the vane leaving an uncooled ring at the vane-endwall junction extending around the shoulder. Coolant from the pressure side leading edge holes exhibits low effectiveness and appears drawn upstream by the leading edge horseshoe vortex. Additionally, the jet farthest upstream in the first row along the vane pressure side appears drawn toward the center of the passage.

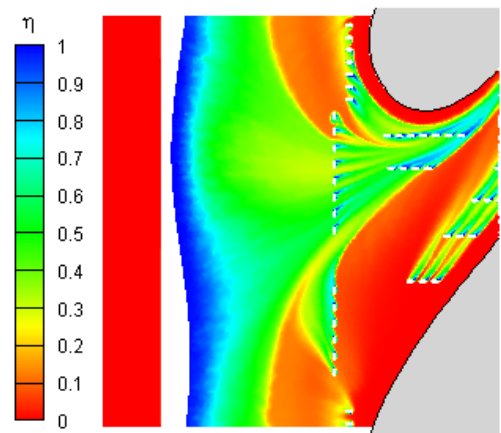
Effects of scalloping the slot and moving its average centerline location axially upstream are illustrated in Figures 2.8(b) and 2.8(c). Both slot configurations have the same total flow area, leakage flow rate, and inlet profile as the baseline configuration of Figure 2.8(a). The average leakage momentum flux ratio for all three slot configurations is $I=0.03$. The average centerline location of the slot in Figure 2.8(b) is at $-0.42C_{ax}$, identical to the



(a) $x/C_{ax} = -0.42$



(b) $x/C_{ax} = -0.42$



(c) $x/C_{ax} = -1.0$

Figure 2.8. Moving the slot upstream yields more uniform injection but reduces effectiveness levels within the passage. All configurations are shown at momentum flux ratio $I=0.03$ for the case #1 inlet conditions.

baseline configuration, while the average centerline location of the slot in Figure 2.8(c) is positioned one axial chord upstream of the vane stagnation.

For a waveform amplitude equal to half of the average slot width ($A=0.5W$), cooling levels and coverage area appear very similar to the baseline two-dimensional configuration for the same average momentum flux ratio and slot location. Coolant coverage appears narrower at the upstream film row yielding a slightly wider uncooled streak between the slot coverage region and the pressure side jets of the upstream row. Cooling levels remain marginally higher along the pressure side edge of the slot coverage area as local mass flow rate is slightly higher than from the two-dimensional geometry in this wider section of the slot. The film-cooling jets throughout the passage appear unaffected in comparison to Fig 2.8(a).

When the slot is moved upstream, coolant is seen to emerge across the entire width of the slot as the vane effect on endwall pressure distribution is reduced. Coolant injection exhibits a sinusoidal pattern indicating the coolant emerges primarily in the region of largest open area although the non-uniformity is not as pronounced as for the downstream location where coolant injects only in the center of the passage. Leakage flow from the upstream slot appears bounded by the legs of the horseshoe vortex and is funneled toward the center of the passage. The horseshoe vortex saddle point for this configuration is upstream of the slot location in Fig 2.8(b) indicating earlier formation. The pressure side leg of the horseshoe vortex draws the pressure side jets in the leading row upstream eliminating the uncooled streak between these jets and the slot coolant. Slot coverage immediately upstream of the leading film-cooling row and within the passage appears nearly identical to Figure 2.8(b), but cooling levels are significantly reduced as the coolant has far longer to mix with the hot core flow gases.

Contours of adiabatic effectiveness for a large amplitude slot geometry waveform are shown in Figures 2.9(a) and 2.9(b). The waveform amplitude is 90% of the average slot width while the phases are zero degrees (directly upstream of stagnation) and 120 degrees (shifted toward the suction side of the passage) respectively. The configuration in Figure 2.9(a) is shown for the inlet conditions specified by case #2 (Table 2.3, Figure 2.7). Both the average slot width and leakage flow rate in Figure 2.9(a) are increased by 50% over the values of Figure 2.8. The configuration in Figure 2.9(b) is shown for the inlet conditions specified by case #1 where the average slot width and leakage flow rate are identical to those of Figure 2.8. This yields nominally the same momentum flux ratio, $I=0.03$. The slot is positioned one axial chord upstream of the vane stagnation in both configurations.

It is seen for both configurations that coolant injection is concentrated primarily in the region of largest open area while very little coolant emerges from the narrowest section of the slot. For zero phase, this induces a coolant coverage area with two peaks wrapping around the pressure and suction sides of the vane and an uncooled region upstream of the center of the passage. Some coolant is shown to penetrate beyond the endwall separation line, outlining cooling levels near unity, upstream of

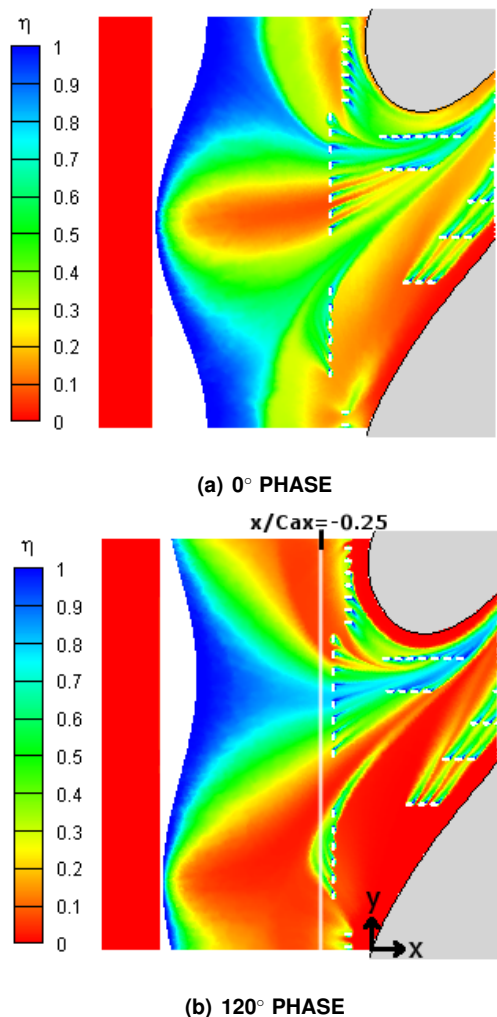


Figure 2.9. Waveform amplitude concentrates coolant injection while phase shifts coverage area laterally ($I=0.03$, $A=0.9W$, $x/C_{ax} = -1.0$).

the leading edge. Leakage flow from the pressure side of the slot fills the space between the suction and pressure side jets of the upstream row broadening coverage area within the passage. Film-coolant from the suction side, leading edge holes advances very near to the vane leading edge-endwall junction while coolant from the pressure side holes of the upstream film-cooling row is drawn upstream and merges with the slot leakage flow.

When the phase is shifted in Figure 2.9(b) such that the open area is concentrated in the middle of the passage, very little coolant emerges toward the pressure side of the leading edge. Higher effectiveness levels are maintained within the passage in the slot coverage area near the vane shoulder in comparison to the zero phase configuration. The leading edge film-cooling jets are less effective leaving a thin uncooled ring at the leading edge-endwall junction while the pressure side jets of the upstream row appear largely unaffected by the shifted slot coolant flow. As before, they are drawn upstream by the pressure side leg of the

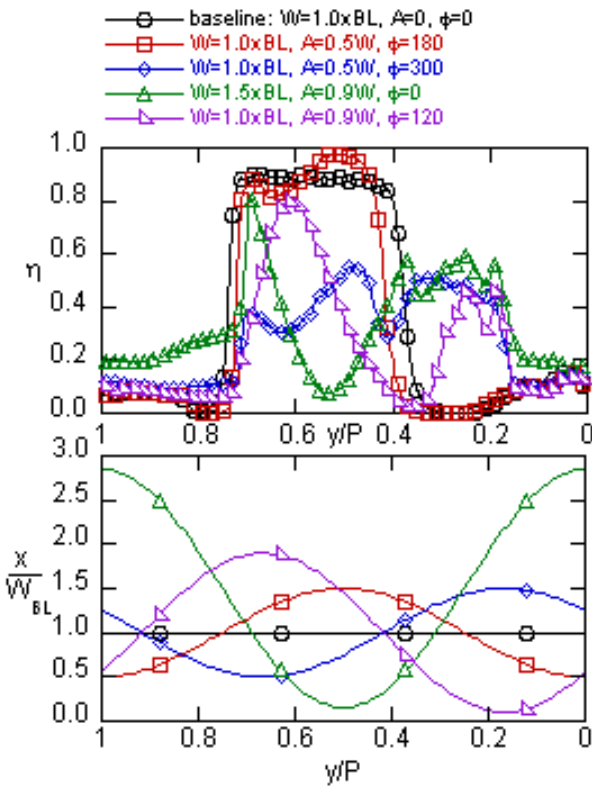


Figure 2.10. Pitchwise adiabatic effectiveness levels at $x/C_{ax} = -0.25$ (top) and slot geometry profiles (bottom) for $l=0.03$ cases.

horseshoe vortex.

Pitchwise adiabatic effectiveness levels at $x/C_{ax} = -0.25$ for the five cases presented in Figures 2.8 and 2.9 are shown in Figure 2.10. This station is slightly upstream of the leading film-cooling row as indicated by the white line in Figure 2.9(b). The configurations are listed in the legend in the order they were presented. The slot geometry profiles are shown in the lower portion of the figure for reference.

Cooling levels for the two configurations associated with Figures 2.8(a) and 2.8(b) appear very similar despite a slot geometry amplitude peak equal to half of the slot average width for the latter. The 180 degree waveform phase aligned the maximum slot open area in the center of the passage, a location where coolant naturally injects because of the low pressure. As noted previously the coolant coverage area is slightly narrower for the scalloped slot, but adiabatic effectiveness levels are a bit higher along the pressure side of the slot coverage range ($y/P=0.5$) where the slot open area is greatest. For both configurations the thermal gradient is quite steep between the edge of the slot coverage and the adjacent portion of the endwall.

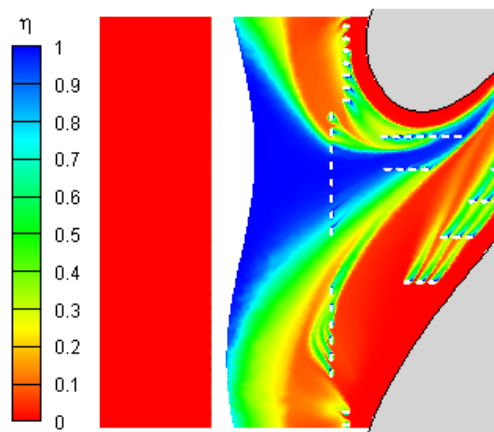
The width and shape of the lobe indicating slot coverage area associated with the configuration of Figure 2.8(c) appears similar to that for Fig 2.8(b). Both range from approximately

$0.4 \leq y/P \leq 0.75$. The slot scallop amplitudes and widths were identical between these configurations, but the phase was shifted from 180 to 300 degrees. Cooling levels for the former configuration are significantly lower, though, as a result of the increased mixing length of the upstream slot location ($x/C_{ax} = -1.0$ vs. -0.42). There is a slight dip in cooling level near $y/P = 0.6$ associated with the narrow slot width at this station and then a rise because of coolant from the peaked region of the slot that is swept between the legs of the horseshoe vortex. On the pressure side of the endwall from $0.2 \leq y/P \leq 0.4$, cooling levels are significantly higher than for the first two configurations. This improvement results from the pressure side jets of the upstream row being drawn upstream as the horseshoe vortex forms further upstream. Cooling levels upstream of the leading edge are similarly low compared to the first two configurations.

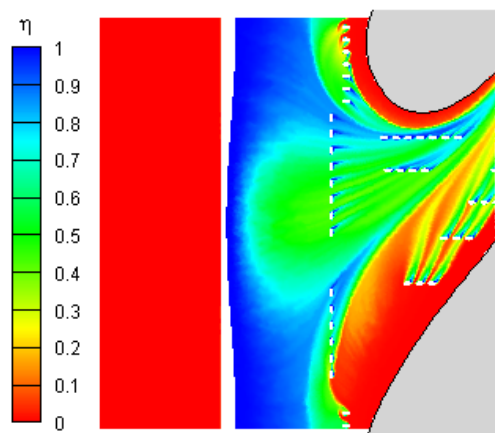
Cooling levels upstream of the leading edge are nearly doubled for the configuration shown in Figure 2.9(a). This slot geometry was highly peaked with an amplitude equal to 90% of the average width and centered directly upstream of the leading edge. The average width was also 50% greater than for the other configurations. To match the coolant momentum flux ratio of the other configurations, the coolant flow rate was also increased by 50%. A spike in cooling level is seen at $y/P = 0.7$ from coolant at the leading edge that is swept around the suction side of the vane. Cooling levels fall rapidly towards the center of the passage, corresponding to the narrowest section of the slot, and then rise toward $y/P = 0.37$ because of leakage flow from the peak upstream of the adjacent leading edge. The primary slot coverage area between the two peaks indicate that the width between the legs of the horseshoe vortex does not vary significantly and that improved effectiveness levels at the leading edge result from leakage penetration beyond the horseshoe vortex. As with the other upstream slot locations, the pressure side jets of the leading row are drawn upstream improving cooling levels in the region between $0.2 \leq y/P \leq 0.4$.

Cooling levels for the configuration shown in Figure 2.9(b) indicate that leakage flow is contained between the legs of the horseshoe vortex from $0.4 \leq y/P \leq 0.75$, but the lobe is much narrower and the peak is shifted slightly toward the suction side of the passage because of the highly peaked slot geometry centered just to the suction side of the center of the passage. As with the configuration of Figure 2.9(a), maximum cooling levels approach those of the configurations where the slot was positioned much closer to the vane in contrast to the lower and more uniform cooling levels of the Figure 2.8(c) configuration.

Finally, cooling effectiveness contours illustrating the effect of expanding and contracting the average slot width for a fixed leakage rate are shown in Figures 2.11(a) and 2.11(b). Each configuration featured a slot waveform amplitude that was 50% of the average slot width, while the average slot width was expanded and contracted by 50% relative to the width of the baseline two-dimensional configuration. Both configurations are shown for the inlet conditions specified by case #3 with the high $1.0\% \dot{m}_{ex}$ flow rate and a peaked inlet total pressure profile. Contracting the slot increased the coolant momentum flux ratio by an



(a) WIDTH = 1.5xBaseline, $I = 0.05$



(b) WIDTH = 0.5xBaseline, $I = 0.47$

Figure 2.11. Contracting the slot improves coverage area at the leading edge and within the passage for a fixed leakage flow rate ($A=0.5W$, $x/C_{ax} = -0.71$, $\dot{m}_c=1.0\%\dot{m}_{ex}$).

order of magnitude.

Slot coolant is seen to penetrate much closer to the vane leading edge for the contracted slot significantly reducing the uncooled area upstream of the vane. The saddle point of the horseshoe vortex also appears closer to the leading edge. Coverage area of the leading edge film-cooling jets appears unaltered. Slot leakage coolant is bounded by the endwall separation lines and is funneled into the center of the passage for both configurations. The coverage area in the upstream portion of the passage is broader for the contracted configuration illustrated by a much narrower uncooled streak through the center of passage. The extended coolant coverage is attributed to the higher momentum flux of the injected leakage flow for the contracted slot. The upstream most jets along the pressure side film-cooling rows also appear drawn further across the passage for the contracted configuration indicating stronger endwall crossflow.

2.7 CONCLUSIONS

In modern gas turbines it is essential to provide cooling to component surfaces because of the extreme operating environment. One surface which is especially difficult to cool because of the complex flow field is the inlet nozzle guide vane endwall. Bypass leakage flow through the combustor-turbine endwall junction has been previously demonstrated to be useful in providing a protective coolant layer insulating portions of the endwall surface from the hot core flow.

A three-dimensional slot was investigated computationally to evaluate effects on endwall cooling. Grid error was assessed to quantify error magnitude and distribution and ensure that no large scale physics were unresolved. Effects of varying the slot waveform amplitude, phase, and upstream location were discussed for a fixed momentum flux ratio. Effects of varying the momentum ratio for a fixed coolant rate were also presented.

Primary effects of varying the slot parameters were as follows. Moving the slot centerline upstream facilitated more uniform coolant injection as the pressure variation across the endwall was reduced but also degraded cooling levels within the passage as the leakage flow had longer to mix with the hot core flow. Slot coolant coverage area was not significantly impacted. Increasing waveform amplitude was shown to concentrate coolant injection in regions with more open area while coolant flow from narrow portions of the slot was restricted. Adjusting waveform phase across the vane pitch shifted coolant injection location and altered coverage area both upstream and within the passage. Finally, expanding and contracting the average slot width altered coolant coverage area. The higher momentum leakage flow emerging from the narrower slot penetrated closer to the vane leading edge and exhibited broader coverage area in the upstream portion of the passage.

NOMENCLATURE

- A waveform amplitude
- C_{ax} vane axial chord
- C_p pressure coefficient, $(p - p_{in}) / 0.5\rho U_{in}^2$
- d hole diameter
- D flow path diameter
- k turbulent kinetic energy
- I momentum flux ratio, $\rho_c V_c^2 / \rho_{in} V_{in}^2$
- L flow path length
- \dot{m} mass flow rate
- p pressure, hole pitch
- P vane pitch
- P_o total pressure
- S vane span
- T temperature
- u,v,w streamwise, stream normal, wall normal local flow velocities
- U inlet flow velocity
- V velocity
- W flow path width
- y^+ non-dimensional relative distance

x,y,z local coordinate system
X,Y,Z global coordinate system

Greek

ε turbulent kinetic energy dissipation rate
 η endwall adiabatic effectiveness, $(T_{in} - T) / (T_{in} - T_c)$
 ϕ waveform phase
 ρ density

Subscripts

BL baseline
c coolant
comp component
ex domain exit
in domain inlet
ref reference

REFERENCES

- [1] Langston, L. S., 1980. "Crossflows In a Turbine Cascade Passage". *Journal of Engineering for Power*, **102**, pp. 866–874.
- [2] Sharma, O. P., and Butler, T. L., 1987. "Predictions of Endwall Losses and Secondary Flows in Axial Turbine Cascades". *J. of Turbomachinery*, **109**, pp. 229–236.
- [3] Goldstein, R. J., and Spores, R. A., 1988. "Turbulent Transport on the Endwall in the Region Between Adjacent Turbine Blades". *J. of Heat Transfer*, **110**, pp. 862–869.
- [4] Blair, M. F., 1974. "An Experimental Study of Heat Transfer and Film Cooling on Large-Scale Turbine Endwalls". *J. of Heat Transfer*, pp. 524–529.
- [5] Granser, D., and Schulenberg, T., 1990. "Prediction and Measurement of Film Cooling Effectiveness for a First-Stage Turbine Vane Shroud". 90-GT-95.
- [6] Burd, S. W., and Simon, T. W., 2000. "Effects of Slot Bleed Injection Over a Contoured Endwall on Nozzle Guide Vane Cooling Performance: Part I: Flow Field Measurements". 2000-GT-199.
- [7] Burd, S. W., Satterness, C. J., and Simon, T. W., 2000. "Effects of Slot Bleed Injection Over a Contoured Endwall on Nozzle Guide Vane Cooling Performance: Part II: Thermal Measurements". 2000-GT-200.
- [8] Oke, R., Simon, T. W., Burd, S. W., and Vahlberg, R., 2000. "Measurements in a Turbine Cascade Over a Contoured Endwall: Discrete Hole Injection of Bleed Flow". 2000-GT-214.
- [9] Oke, R., Simon, T., Shih, T., Zhu, B., Lin, Y. L., and Chyu, M., 2001. "Measurements Over a Film-Cooled, Contoured Endwall with Various Coolant Injection Rates". 2001-GT-140.
- [10] Oke, R., and Simon, T., 2002. "Film-Cooling Experiments with Flow Introduced Upstream of a First Stage Nozzle Guide Vane Through Slots of Various Geometries". GT2002-30169.
- [11] Roy, R. P., Squires, K. D., Gerendas, M., Song, S., Howe, W. J., and Ansari, A., 2000. "Flow and Heat Transfer at the Hub Endwall of Inlet Vane Passages - Experiments and Simulations". 2000-GT-198.
- [12] Lynch, S. P., and Thole, K. A., 2007. "The Effect of Combustor-Turbine Interface Gap Leakage on the Endwall Heat Transfer for a Nozzle Guide Vane". GT2007-27867.
- [13] Colban, W. F., Thole, K. A., and Zess, G., 2002. "Combustor-Turbine Interface Studies: Part 1: Endwall Measurements". *J. of Turbomachinery*, **125**, pp. 193–202.
- [14] Colban, W. F., Lethander, A. T., Thole, K. A., and Zess, G., 2002. "Combustor-Turbine Interface Studies: Part 1: Flow and Thermal Field Measurements". *J. of Turbomachinery*, **125**, pp. 203–209.
- [15] Kost, F., and Nicklas, M., 2001. "Film-Cooled Turbine Endwall in a Transonic Flow Field: Part I - Aerodynamic Measurements". 2001-GT-0145.
- [16] Nicklas, M., 2001. "Film-Cooled Turbine Endwall in a Transonic Flow Field: Part II - Heat Transfer and Film-Cooling Effectiveness Measurements". 2001-GT-0146.
- [17] Kost, F., and Mullaert, A., 2006. "Migration of Film-Coolant from Slot and Hole Ejection at a Turbine Vane Endwall". GT2006-90355.
- [18] Knost, D. G., and Thole, K. A., 2005. "Computational predictions of endwall film-cooling for a first stage vane". *International J. of Turbo and Jet Engines*, **22**, pp. 41–58.
- [19] Knost, D. G., and Thole, K. A., 2005. "Adiabatic Effectiveness Measurements of Endwall Film-Cooling for a First Stage Vane". *J. of Turbomachinery*, **127**, pp. 297–305.
- [20] Cardwell, N., Sundaram, N., and Thole, K. A., 2006. "The Effects of Varying the Combustor-Turbine Gap". GT2006-90089.
- [21] Radomsky, R. W., and Thole, K. A., 2000. "Flowfield Measurements for a Highly Turbulent Flow in a Stator Vane Passage". *J. of Turbomachinery*, **122**, pp. 255–262.
- [22] Hermanson, K., and Thole, K. A., 2000. "Effect of Inlet Profiles on Endwall Secondary Flows". *J. of Propulsion and Power*, **16**, pp. 286–296.
- [23] Fluent Inc., 2006. *Fluent 6.3 User's Guide*. (Fluent Inc: New Hampshire).
- [24] Knost, D. G., Thole, K. A., and Duggleby, A., 2010. Parametric Investigation of the Combustor-Turbine Interface Leakage Geometry: Part I - Thermal Optimization. Submitted to GT2010.
- [25] Knost, D. G., Thole, K. A., and Duggleby, A., 2010. Parametric Investigation of the Combustor-Turbine Interface Leakage Geometry: Part II - Secondary Flows. Submitted to GT2010.

**3 Parametric Investigation of the Combustor-Turbine Interface
Leakage Geometry: Part I - Thermal Optimization - *Journal of
Turbomachinery*, in submission**

GT2010-XXXX1

PARAMETRIC INVESTIGATION OF THE COMBUSTOR-TURBINE INTERFACE LEAKAGE GEOMETRY: PART I - THERMAL OPTIMIZATION

D.G. Knost*

Mechanical Engineering
Virginia Tech
Blacksburg, Virginia 24061

K.A. Thole

Mechanical and Nuclear Engineering
The Pennsylvania State University
State College, Pennsylvania 16802

A. Duggleby

Mechanical Engineering
Texas A&M University
College Station, Texas 77843

ABSTRACT

Bypass leakage flow through the combustor-turbine endwall junction has been demonstrated to provide thermal benefit to portions of the nozzle guide vane endwall. For conventional, two-dimensional slots between the combustor and turbine, coolant emerges between the airfoils and is transported toward the suction side of the passage. Areas at the leading edge and along the pressure side typically see very little cooling benefit from this leakage flow.

A parametric investigation of a three-dimensional slot is presented using statistical analysis to quantify the impact of geometric features on endwall adiabatic effectiveness. Upstream distance to the slot center line was found to dominate overall effectiveness levels regardless of inlet conditions, while average slot width was also significant at higher blowing rates. A robust configuration was identified that improved cooling effectiveness for all inlet conditions, when compared to a baseline two-dimensional slot, by extending coolant coverage area and improving coolant uniformity.

3.1 INTRODUCTION

As turbine inlet temperatures have trended upward it has become essential to cool hardware. One component surface, which has proven difficult to manage because of the complex flowfield in its vicinity, is the nozzle guide vane endwall. Bypass leakage flow through the slot between the combustor and turbine endwalls has been demonstrated to provide some thermal benefit to the endwall surface. In manufacturing, the edges forming this leakage path have traditionally been two-dimensional. By scalloping the edges to form a three-dimensional flow path, it may be possible to more effectively harness bypass leakage flow. This

could concentrate coolant in areas that are typically difficult to manage and may reduce strong thermal gradients across the end-wall alleviating thermal stresses.

In this study, a three-dimensional geometry is explored using parameter mean-effects estimation and analysis of variance to quantify the influence of various geometric parameters. An optimized configuration is identified that promotes both thermal enhancement and robustness. Part II of the study examines secondary flow development and evaluates aerodynamic losses and coolant transport through the passage.

3.2 LITERATURE SUMMARY

Several studies have measured endwall heat transfer as a result of injection from a two-dimensional, flush slot just upstream of the vane. Originally, Blair [1] measured adiabatic effectiveness levels and heat transfer coefficients for a range of blowing ratios through a flush slot positioned just upstream of the leading edges of a single passage channel. He found that the end-wall cooling distribution showed extreme variations across the vane pitch. Much of the coolant was swept across the endwall toward the suction side corner resulting in reduced coolant near the pressure side. As the blowing ratio was increased, he found that the extent of the coolant coverage also increased. Measured heat transfer coefficients were similar between no slot and slot injection cases. In a later study by Granser and Schulenberg [2], similar adiabatic effectiveness results were reported with higher values occurring near the suction side of the vane.

Roy et al. [3] compared their experimental measurements and computational predictions for a flush cooling slot that extended over only a portion of the pitch directly in front of the vane stagnation. Contrary to the previously discussed studies, their adiabatic effectiveness measurements indicated that the coolant

*Address all correspondence to this author. email: dknost@vt.edu

migrated toward the pressure side of the vane. Their measurements also showed reduced values of local heat transfer coefficients at the leading edge when slot cooling was present relative to no slot cooling.

Nicklas [4] presented heat transfer and film-cooling effectiveness measurements from a transonic cascade with an upstream slot and film-cooling holes along the passage endwall. Adiabatic effectiveness measurements indicated higher values near the suction side of the vane due to the slot coolant migration. Kost and Mullaert [5] studied the same airfoil geometry but moved the flush slot upstream to $0.3C_{ax}$ upstream of the vane. They found that for this configuration, slot flow stayed closer to the endwall and provided better cooling than flow from the slot located at $0.2C_{ax}$ upstream of the vane.

Oke and Simon [6] presented results from two upstream film-cooling rows with sections blocked to promote discharge in certain areas. An upstream hole configuration featuring a linear taper on the pressure and suction sides toward the center of the passage provided coolant to the leading edge at all blowing conditions. Injection from a single row of holes with a linear taper on the suction side improved coolant supply to the pressure side at all blowing conditions. Pressure side coverage was higher than for the suction side at high mass flow ratios.

While the thermal effects of varying operating conditions from many fixed geometries have been studied, few have investigated varying the slot leakage geometry to manipulate coolant coverage and effectiveness. This work seeks to quantify the impact of varying geometric features of the slot geometry and optimize the slot to enhance endwall cooling effectiveness.

3.3 COMBUSTOR-TURBINE JUNCTION PARAMETERS

Traditionally the combustor-turbine junction in published studies has been two-dimensional with the downstream edge of the combustor endwall and the upstream edge of the vane endwall flush and parallel. A three-dimensional slot geometry was investigated for this study utilizing a scalloped downstream edge intended to provide variable leakage flow metering across the vane pitch. As illustrated in Figure 3.1(a) and defined in Eq. 3.1, the downstream edge of the slot featured a cosine wave with four parameters: amplitude, phase, average slot width, and upstream distance to the slot centerline.

$$x = A \cos(2\pi y/P + \phi) + D + W/2 \quad (3.1)$$

A cosine was selected because of its smooth and continuous properties. The slot was flush and injected downstream at an inclination angle of 45 degrees with respect to the endwall as shown in Figure 3.1(b). The endwall film-cooling pattern featured axially aligned rows of holes and was originally described by Knost and Thole [7,8].

As mentioned in the literature review, previous studies have shown slot coolant to inject primarily near the center of the passage with little coolant emerging upstream of the vane leading

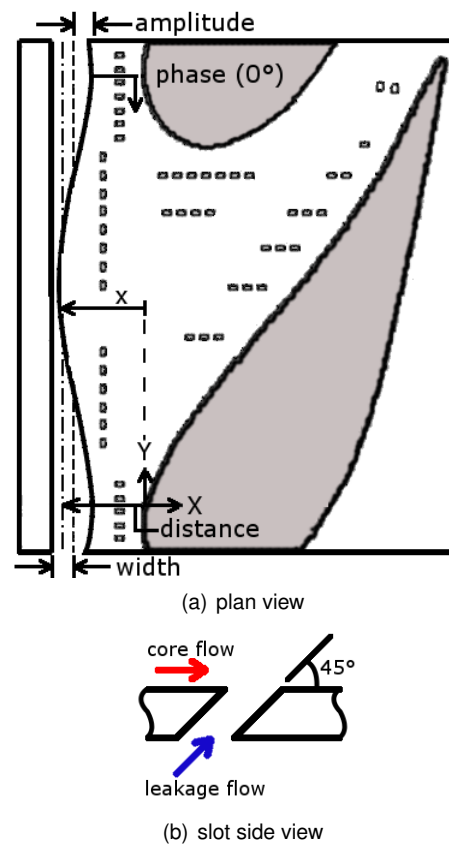


Figure 3.1. The three-dimensional slot was flush and defined by four parameters: amplitude, phase, width, and upstream distance.

edge. This results in over-cooling in the center and under-cooling at the leading edge and on the pressure side of the endwall. The slot waveform amplitude was intended to restrict coolant mass flow in areas of low pressure, via reduced leakage path area, reducing over-cooling. It was also thought that concentrating the slot open area in typical regions of low cooling may increase leakage flow over portions of the upstream endwall that are more difficult to cool. Additionally the slot waveform amplitude was expected to have some effect on secondary flow development as less slot injection in low pressure areas may reduce the sink effect influence of the slot flow seen in previous studies [8] while higher coolant injection could energize the boundary layer in areas where the flow stagnates. Amplitude was measured from the centerline of the vane endwall upstream edge, indicated by a dash-dash line in Figure 3.1(a), and specified as a fraction of the average slot width.

Phase of the slot waveform was also investigated. Varying the phase was expected to alter the leakage flow distribution shifting the slot coolant laterally across the endwall. Shifting phase was also expected to have some effect on secondary flow development as blowing non-uniformity was adjusted across the vane pitch. Phase was measured from a zero degree reference directly upstream of the vane stagnation. Neither the amplitude

or phase parameters affected total flow area.

The average slot width was varied as a global means of altering slot coolant momentum flux ratio. The average slot width was computed as the distance between the upstream edge of the leakage gap and the centerline of the downstream edge formed by the waveform. Cardwell et al. [9] showed that varying slot width for a fixed coolant mass flow rate affected slot coolant coverage area as higher momentum leakage flow penetrated beyond the endwall separation line of the horseshoe vortex yielding more uniform coolant coverage. A narrower average slot width in combination with the open area concentrated near the leading edge was expected to improve coolant coverage in difficult areas at the leading edge and along the pressure side.

The final parameter under investigation was upstream distance to the nominal slot centerline. Upstream distance was measured from the axial location of the stagnation point to the centerline between the upstream edge and the average downstream edge of the slot. The average slot centerline is marked by a dash-dot line in Figure 3.1(a). Previous studies, discussed in the literature review, indicated that slot coolant exits in a non-uniform manner because of the varying static pressure distribution over the endwall due to the presence of the downstream vanes. Lynch and Thole [10] demonstrated that moving the slot further upstream improved slot coolant injection uniformity because the influence of the vanes was reduced, but cooling levels within the passage were diminished as the coolant had longer to mix with the hot core flow. Varying the upstream slot distance was intended to balance these effects to achieve coolant injection uniformity and effectiveness.

3.4 COMPUTATIONAL METHODS

The vane used in this study was a commercial nozzle guide vane originally described by Radomsky and Thole [11]. It was two-dimensional with the midspan cross section modeled along the entire span. The vane and all other geometries in this study were scaled up by a factor of nine to allow direct comparison of results with any data acquired in the large-scale wind tunnel test section previously described by Knost and Thole [8]. The exit Reynolds number based on chord was matched to the engine value of 1.2×10^6 .

The vane was divided at the dynamic stagnation location and trailing edge with a single passage modeled between. A velocity inlet boundary was specified one chord upstream of the passage and an outflow $0.25C$ beyond the vane in the axial direction. These locations were determined by Hermanson and Thole [12] to be free of pressure effects from the vane. Periodic boundary conditions were imposed in the stagnation plane and beyond the trailing edge. The passage was modeled to midspan with an imposed symmetry condition to allow greater cell resolution within the domain. The slot and film-cooling holes were supplied from separate plenums with coolant mass flow rate and temperature prescribed at mass flow inlets. All walls were modeled as adiabatic with no slip except for the vertical plenum walls, which were shear free. This was done to avoid viscous effects in the

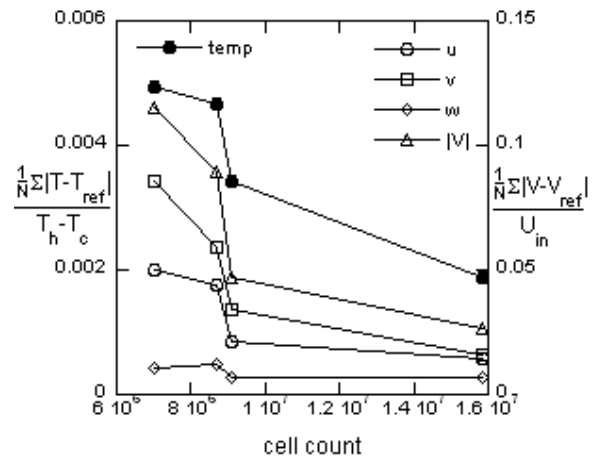


Figure 3.2. Grid error was reduced as cell resolution increased.

corners of the plenums.

A grid study, described in detail by Knost and Thole [13], was conducted to evaluate grid error. As shown in Figure 3.2, error was found to decrease with increased grid resolution. For results reported in this paper, production grids typically ranged from 14.5 to 16 million cells and processed on computing clusters with 32 GB of RAM.

The incompressible Reynolds-Averaged Navier-Stokes (RANS), energy, and turbulence equations were computed using the Fluent 6 pressure-based segregated solver. In this approach the momentum and pressure correction (continuity) equations are solved sequentially. The mass fluxes, pressure, and velocity fields are then updated from the pressure correction and additional scalar quantities such as energy and turbulence are computed. The segregated approach is memory efficient, since the segregated equations need only be stored one at a time, however solution convergence is relatively slow [14].

The RNG $k - \epsilon$ turbulence model was utilized with enhanced wall functions. The RNG $k - \epsilon$ turbulence model exhibits improved performance in comparison to the standard $k - \epsilon$ model for complex shear flows and flows with high strain rates, swirl, and separation. Hermanson and Thole [12] showed good prediction of secondary flows with the RNG $k - \epsilon$ turbulence model. The enhanced wall function option in Fluent employs a two-layer zonal model in the near-wall region where the laminar sublayer is resolved directly if grid resolution is fine enough ($y^+ \approx 1$) and a blending function is applied in the buffer layer [14].

All equations were computed with second order discretization for 1400 iterations. Solution residuals, area-averaged end-wall temperature, mass-averaged total pressure at the inlet and outlet, lift, and drag coefficients were monitored at each iteration to evaluate solution convergence. Typical solution times ranged from 24-30 hours on ten 2.0GHz 64-bit processors.

3.5 DESIGN OF EXPERIMENTS

The trial layout for this investigation, listed in Table 3.1, was a fractional factorial design incorporating an orthogonal array. This is the method advocated by Taguchi [15]. Orthogonal arrays are balanced such that each factor is evenly distributed (all factor combinations appear an equal number of times) and thus has equal opportunity to influence the output. This allows efficient evaluation of many parameters at multiple levels. For this study, a full factorial design would have required 162 trial configurations. Parameter interactions were not explicitly accounted for but were distributed uniformly across all trials.

Three levels of the slot amplitude, average width, and upstream distance parameters were investigated to qualify non-linearity while six phase values were explored to evaluate periodicity. In all, eighteen trial configurations were simulated along with a two-dimensional baseline geometry used for reference and comparison of results. Note that amplitude is expressed as a fraction of the average slot width (W) in Table 3.1, while average slot width is related to the nominal flow path width of the baseline two-dimensional slot configuration. The three widths investigated included an average width yielding the same flow path area as the baseline, two-dimensional slot studied by Knost and Thole [7, 8], a contracted width equivalent to 50% of the baseline slot flow area, and an expanded width equivalent to 150% of the baseline slot flow area. The nominal slot length-to-width ratio was 1.8 with an average flow path width of 1.48cm at a 9x scale.

3.6 INLET CONDITIONS

Each trial configuration was evaluated at three sets of inlet conditions. These cases, listed in Table 3.2, were distinguished by the inlet velocity and total pressure profiles as well as slot leakage flow rate. The three cases were intended to represent a wide range of inlet total pressure profiles and slot coolant blowing rates. The film-coolant flow rate was fixed at 0.5% of the total exit massflow and the inlet temperature profile was uniform for all cases to avoid confounding with variations in the leakage flow.

The normalized inlet velocity profile for each case is shown in Figure 3.3. Hermanson and Thole [12] showed that secondary flow development was highly sensitive to the total pressure profile exiting the combustor. The turbulent inlet boundary layer they computed was selected for case #1 as the total pressure deficit in the boundary layer was identified as the primary factor in development of the horseshoe vortex. The slot leakage rate for case #1 was equal to the film-cooling rate at 0.5% of the total exit mass flow.

A uniform inlet velocity profile was selected for case #2 corresponding to the original inlet condition studied by Knost and Thole [7, 8]. When combined with the uniform inlet temperature, this yielded a blunt total pressure profile at the domain inlet. The slot leakage rate was increased by 50% over case #1 to $0.75\dot{m}_{ex}$.

Finally, Hermanson and Thole argued that the turbulent boundary layer and uniform inlet temperature were not necessarily representative of combustor exit profiles during operation

Table 3.1. Trial Parameter Configurations

Trial	Phase	Amp	Width(W)	Distance
1	0	0.1W	1.0Nom	-0.42C _{ax}
2	0	0.5W	0.5Nom	-0.71C _{ax}
3	0	0.9W	1.5Nom	-1.00C _{ax}
4	60	0.1W	1.0Nom	-0.71C _{ax}
5	60	0.5W	0.5Nom	-1.00C _{ax}
6	60	0.9W	1.5Nom	-0.42C _{ax}
7	120	0.1W	0.5Nom	-0.42C _{ax}
8	120	0.5W	1.5Nom	-0.71C _{ax}
9	120	0.9W	1.0Nom	-1.00C _{ax}
10	180	0.1W	1.5Nom	-1.00C _{ax}
11	180	0.5W	1.0Nom	-0.42C _{ax}
12	180	0.9W	0.5Nom	-0.71C _{ax}
13	240	0.1W	0.5Nom	-1.00C _{ax}
14	240	0.5W	1.5Nom	-0.42C _{ax}
15	240	0.9W	1.0Nom	-0.71C _{ax}
16	300	0.1W	1.5Nom	-0.71C _{ax}
17	300	0.5W	1.0Nom	-1.00C _{ax}
18	300	0.9W	0.5Nom	-0.42C _{ax}
base	0	0.0W	1.0Nom	-0.42C _{ax}

Table 3.2. Inlet Conditions for Various Cases

Inlet condition	Case #1	Case #2	Case #3
Inlet profile	Turb BL	Uniform	Peaked
Slot leakage rate	$0.5\dot{m}_{ex}$	$0.75\dot{m}_{ex}$	$1.0\dot{m}_{ex}$
Film-coolant rate	$0.5\dot{m}_{ex}$	$0.5\dot{m}_{ex}$	$0.5\dot{m}_{ex}$

because of film-cooling and dilution blowing in the combustor. They proposed a total pressure profile that was peaked near the endwall as a result of much cooler fluid in the near-wall region. This led to a flow split part way up the vane span and a counter rotation of the flow above this station. Because it was undesirable in this study to introduce variations in coolant blowing anywhere but at the slot geometry, a peaked near-wall velocity profile was computed to match the peaked total pressure profile of Hermanson and Thole. This peaked profile was imposed as the inlet condition for case #3. The slot leakage rate for case #3 was double that of case #1 at one percent of the total exit flow rate.

The three leakage rates in combination with the three av-

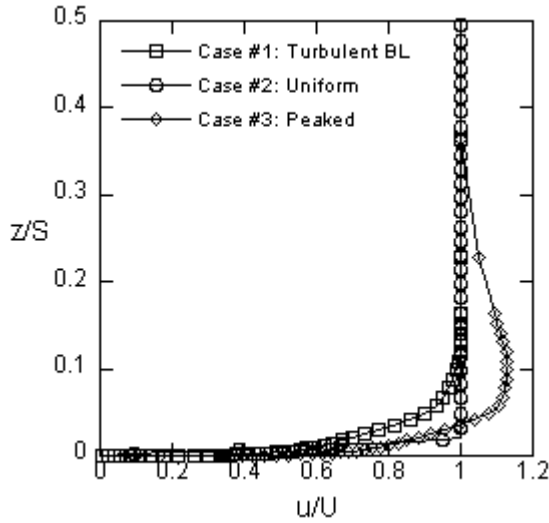


Figure 3.3. Three inlet velocity profiles were simulated including a turbulent boundary layer, uniform profile, and a near-wall peaked profile.

Table 3.3. Momentum Flux Ratios (I) for Case-Geometry Combinations

Width(W)	Case #1	Case #2	Case #3
0.5Nom	0.14	0.27	0.47
1.0Nom	0.03	0.07	0.12
1.5Nom	0.02	0.03	0.05

erage slot widths yielded nine average momentum flux ratios, listed in Table 3.3. Three momentum flux ratios were investigated per case ranging approximately an order of magnitude from the widest slot to the narrowest.

3.7 PERFORMANCE EVALUATION METRIC

Area-averaged adiabatic endwall temperature, \bar{T}_{ew} , normalized as endwall adiabatic effectiveness $\bar{\eta}$, was selected as the characteristic to evaluate overall thermal performance. These characteristics are defined in Eqs. 3.2 and 3.3. An adiabatic effectiveness of zero indicates no cooling while a value of unity indicates perfect cooling.

$$\bar{T}_{ew} = \left[\frac{1}{A} \int_{ew} T_{aw}^2 dA \right]^{1/2} \quad (3.2)$$

$$\bar{\eta} = \frac{T_{in} - \bar{T}_{ew}}{T_{in} - T_c} \quad (3.3)$$

The root-mean-squared adiabatic endwall temperature was computed to emphasize hotspots. Area averages were computed from

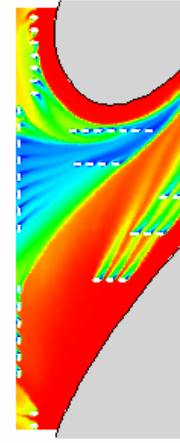


Figure 3.4. Area averages were computed from immediately upstream of the leading row of film-cooling holes to 50% axial chord within the passage.

immediately upstream of the leading row of film-cooling holes to 50% axial chord within the passage as illustrated in Figure 3.4. This was necessary to evaluate the performance effects over the same region for each configuration as the vane endwall area and distribution varied dependent upon the upstream distance of the leakage geometry and the amplitude and phase of the slot waveform.

3.8 DISCUSSION OF RESULTS

Results of the trials were analyzed using mean-effects plots, analysis of variance, and signal-to-noise ratio. Factor level contributions were computed to estimate the average effect of each parameter individually. The response characteristics for all trials involving a parameter at a single level were averaged and subtracted from the mean response computed across all trials to determine the factor level contribution. From the factor level contributions, the expected response for any parameter level combination can be calculated as:

$$E(\bar{T}_{ew,ijkm}) = \bar{T}_{ew,\dots} + A_i + \phi_j + W_k + D_m \quad (3.4)$$

where $\bar{T}_{ew,\dots}$ is the rms adiabatic wall temperature averaged over all trials, A_i is the contribution of the waveform amplitude parameter at level i , ϕ_j is the contribution of the waveform phase parameter at level j , W_k is the contribution of the slot average width parameter at level k , and D_m is the contribution of the upstream distance parameter at level m .

The four slot parameters were evaluated at the levels listed in Table 3.4 for the three inlet condition cases (Table 3.2). All parameter levels are listed in order of increasing magnitude. Three levels of the amplitude, width, and distance parameters were selected to evaluate non-linearity of each, while six levels of phase

Table 3.4. Parameter Levels for Factor Effects Plots

Parameter				
Level	Phase	Amp	Width(W)	Distance
1	0°	0.1W	0.5Nom	-0.42C _{ax}
2	60°	0.5W	1.0Nom	-0.71C _{ax}
3	120°	0.9W	1.5Nom	-1.00C _{ax}
4	180°			
5	240°			
6	300°			
7	360°			

were investigated to identify periodic effects. The seventh level of phase (360°) is repeated data from level 1 (0°) and was not simulated explicitly.

3.8.1 Case #1 Inlet Conditions

The average thermal effect of the parameters at each level evaluated for the case #1 inlet conditions (turbulent boundary layer and 0.5% \dot{m}_{ex} slot flow) can be viewed in Figure 3.5. The factor level contributions are presented as mean area-averaged adiabatic effectiveness levels, $\bar{\eta}$, computed across all trials including the parameter at the level of interest.

For the case #1 inlet conditions with a total pressure deficit in the boundary layer and the low 0.5% \dot{m}_{ex} slot leakage flow rate, Figure 3.5 shows that the largest effect, evaluated as deviation from the trial average, results from varying the slot upstream distance. The average endwall adiabatic effectiveness is also most sensitive to variations in the slot upstream distance as evidenced by the steep slope between levels. Some non-linearity is observed as performance becomes less sensitive the further the leakage gap moves upstream from the vane, falling from $\Delta\bar{\eta}/\Delta(x/C_{ax}) = 0.149$ between $x/C_{ax} = -0.42$ and -0.71 to $\Delta\bar{\eta}/\Delta(x/C_{ax}) = 0.054$ between $x/C_{ax} = -0.71$ and -1.0 . This is likely because of reduced fluctuations in the endwall pressure distribution as a result of the downstream vanes and the low momentum of the coolant at this low blowing condition.

The effects of varying the average slot width and waveform amplitude are much smaller for these inlet conditions, as seen in Figure 3.5. The average cooling effectiveness varies linearly with slot width, decreasing as the slot is expanded. The momentum flux ratio (Table 3.3) ranges from 0.14 to 0.02 for these conditions and effectiveness gain ($\Delta\bar{\eta}/\Delta I$) decreases with increasing momentum. The mean amplitude effect is extremely non-linear with the poorest average response from a moderately scalloped slot with an amplitude that is half of the average width (level 2).

The mean phase effect exhibits two cycles as the phase of the geometry waveform is adjusted across the vane pitch. A small benefit is seen if the widest part of the leakage gap is directly upstream of the vane dynamic stagnation (0°, 360° phase), but

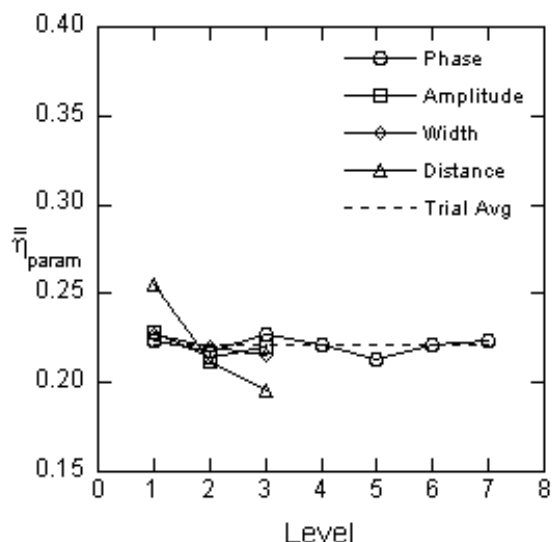


Figure 3.5. Mean parameter thermal effects for case #1.

performance level falls off as the waveform is adjusted to either side of the stagnation location. A cycle of longer length is seen as the phase passes across the center of the passage with maximum benefit achieved at 120°. This is in the region of lowest pressure along the endwall and acts as a natural sink for coolant between the legs of the horseshoe vortex. While phase has little effect on area-averaged adiabatic effectiveness, it was shown by Knost and Thole [?] to influence local cooling levels by shifting coolant laterally across the endwall altering coverage distribution.

The optimal configuration is determined by selecting each parameter at the identified level of maximum benefit. The optimal configuration for the case #1 inlet conditions is listed in Table 3.5. The expected endwall adiabatic effectiveness level of this configuration for the prescribed inlet conditions is $\bar{\eta} = 0.275$, computed by summing the expected contribution of each parameter with the trial average. This configuration is expected to offer a slight improvement over the baseline, two-dimensional configuration value of $\bar{\eta}_{baseline} = 0.273$

While mean-effects analysis is useful for evaluating parameter trending, non-linearity, and identifying an optimal configuration, it offers only limited insight into variability. For this, analysis of variance (ANOVA) is useful. ANOVA is a method for decomposing variability into parts attributable to each parameter under investigation as well as variability that is not directly associated with a study parameter or that exists within samples of the same parameter level. This second type of variability, termed error variability, may arise because of influential factors that were not included as a parameter under study, uncontrollable factors during experimentation (also referred to as noise), or any other errors during the experimental setup and data collection.

The ANOVA table for the trial configurations simulated at the case #1 inlet conditions is listed in Table 3.6. The values in the table were computed using the thermal performance characteristic \bar{T}_{ew} . The total variability, computed as TSS =

Table 3.5. Estimated Thermal Contribution of Parameters at Optimal Configuration for Case #1 Inlet Conditions

Parameter	Level	$\bar{\eta}$ contrib
Phase	120°	+0.006
Amplitude	0.1W	+0.007
Width(W)	0.5Nom	+0.006
Distance	-0.42C _{ax}	+0.034
$\bar{\eta}_{trial\ avg}$		0.221
$\Sigma\ contrib$		+0.054
$\bar{\eta}_{opt}$		0.275

Table 3.6. Thermal ANOVA - Case #1

Factor	DOF	TSS	MSS	F-Ratio	α
Phase	5	0.654	0.131	1.226	0.400
Amplitude	2	1.106	0.553	5.180	0.049
Width(W)	2	0.888	0.444	4.159	0.074
Distance	2	22.59	11.29	105.8	0.000
Error	6	0.640	0.107		
Total	17	25.88			

$\sum(\bar{T}_i - \bar{T}_{avg})^2$, is divided amongst the four parameters under study and the error term. The total degrees of freedom (DOF) for the study is computed as $n - 1$ where n is the total number of samples. The DOF for a parameter is one less than the number of levels of that parameter. The mean sum of squares (MSS), or variance, for any factor is the associated TSS divided by the DOF of the factor.

Analysis of variance is useful in determining which parameters are statistically significant in their contribution to variability. This is done with an F-test, which is a test of the probability that at least one of the parameter level contributions (Eq. 3.4) is not zero for each parameter under consideration. The F-ratio is computed as the ratio of parameter variance to error variance, MSS_{par}/MSS_{err} .

In statistical hypothesis testing there are two types of error: α and β . The first type, α , is the probability that a hypothesis is falsely accepted (in this case that a parameter is accepted as significant when it is not). The second type, β error, is the probability that a hypothesis is falsely rejected. This type of error is not considered in ANOVA.

For a given confidence level a parameter is accepted as significant if its F-ratio is greater than the computed F-distribution value $F(dof_1, dof_2, \alpha)$ where dof_1 is the degrees of freedom of the parameter and dof_2 is the error degrees of freedom. For a 95% confidence interval α equals 0.05. Another method of determining the rejection criteria is computing the value α for the

Table 3.7. Expected Value of Optimal Configuration RMS Adiabatic Effectiveness for All Inlet Conditions

Inlet Cond	$\bar{\eta}_{opt}$	$\bar{\eta}_{opt}/\bar{\eta}_{baseline}$
Case #1	0.255 ± 0.009	0.902 – 0.968
Case #2	0.399 ± 0.021	0.950 – 1.053
Case #3	0.394 ± 0.023	1.127 – 1.266
S/N	0.351 ± 0.018	1.007 – 1.100

F-ratio of the parameter under consideration. This allows researchers with alternative confidence criteria to make their own decision of what should be considered “significant enough”. If the desired value of α is greater than the computed value then the parameter is accepted as significant. For the parameters of this study with the case #1 inlet conditions using a 95% confidence interval ($\alpha \leq 0.05$), only the upstream distance of the slot is identified as significant in contributing to variability of area-averaged endwall adiabatic effectiveness (amplitude was rejected after pooling). This implies that while coolant distribution may be manipulated by varying slot geometry, overall cooling levels may only be significantly affected by moving the slot closer to the vanes.

The parameters that are rejected as significant are pooled (combined) with the error term to improve the optimum performance estimate and decrease uncertainty. Pooled parameters are typically not included in revised performance estimates for the optimal configuration. Once the significant parameters are identified, the relative influence of each can be computed. The pure sum of squares is computed as $PSS = TSS_{par} - (dof_{par} \times MSS_{err})$ and the percent influence is taken as the ratio PSS/TSS . For case #1 the upstream slot distance was computed to contribute 85.6% of total variability while the remaining 14.4% was attributed to factors unaccounted for. In a simulation environment where there is no variability of operating conditions between runs, this effect is likely resultant from weak parameter coupling effects or non-linearities.

Improved estimates of average endwall cooling effectiveness for the optimal configuration (listed in Table 3.5) using analysis of variance data and a 95% confidence interval are listed in Table 3.7. It is seen that for the case #1 inlet conditions, the average thermal performance is expected to be slightly degraded in comparison to the baseline, two-dimensional configuration with a 3.2-9.8% reduction in rms adiabatic effectiveness.

3.8.2 Case #2 Inlet Conditions

The mean thermal parameter level contributions for the inlet conditions specified by case #2 (uniform velocity/total pressure profile and 0.75% \dot{m}_{ex} leakage flow) are shown in Figure 3.6. The levels are defined in Table 3.4. As for the case #1 inlet conditions, slot upstream distance is seen to have the largest effect. As the slot is moved closer to the vane, from level three (-1.0C_{ax}) to one (-0.42C_{ax}), the area-averaged adiabatic effectiveness in-

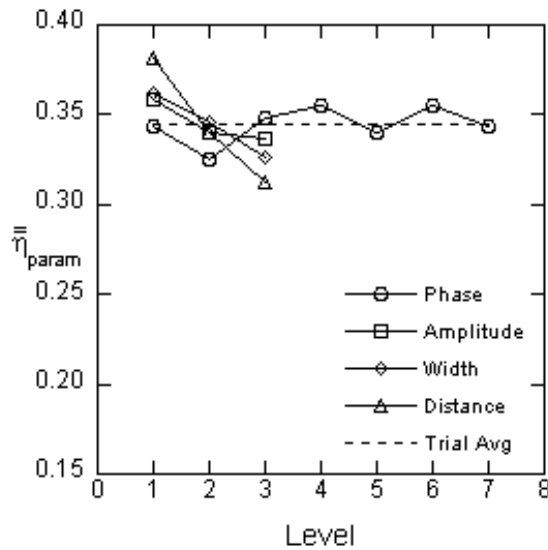


Figure 3.6. Mean parameter thermal effects for case #2.

creases in a nearly linear fashion. The leading edge horseshoe vortex is minimized by this inlet profile because there is no near-wall total pressure gradient. This likely improves linearity as the slot centerline distance from the vane is varied.

The average slot geometry width is also seen to have a nearly linear effect improving as the slot is contracted by increasing the momentum of the injected coolant. Momentum flux ratios (Table 3.3) are doubled from case #1. However, effectiveness gain, while higher, still decreases with increased momentum ratio from $\Delta\bar{\eta}/\Delta I = 0.499$ between levels three ($W=1.5\text{Nom}$) and two ($W=1.0\text{Nom}$) to 0.080 between levels two and one ($W=0.5\text{Nom}$).

Waveform phase, as in case #1, shows two cycles of enhancement. One peak exists at 300° where the maximum slot open area is shifted just to the pressure side of the dynamic stagnation location. Endwall-averaged adiabatic effectiveness falls sharply as phase is adjusted to either side but rises toward the center of the passage exhibiting a slightly higher performance peak of $\bar{\eta} = 0.355$ at 180° .

The waveform amplitude parameter exhibits significant non-linearity with performance worsening as the waveform amplitude is increased. This results in regions with little coolant coverage as leakage flow is concentrated downstream of the region of largest open area. [?].

The optimal configuration for the case #2 inlet conditions is listed in Table 3.8. An expected thermal benefit of $\Delta\bar{\eta} = 0.025$ over the baseline configuration adiabatic effectiveness, $\bar{\eta}_{\text{baseline}} = 0.398$, is predicted.

The analysis of variance table for all trials simulated with the case #2 inlet conditions is listed in Table 3.9. It seen for a 95% cutoff ($\alpha \leq 0.05$) that slot average width and centerline upstream distance are significant in contributing to variability of area-averaged endwall adiabatic effectiveness while the waveform phase and amplitude parameters are not (amplitude is re-

Table 3.8. Estimated Thermal Contribution of Parameters at Optimal Configuration for Case #2 Inlet Conditions

Parameter	Level	$\bar{\eta}$ contrib
Phase	180°	+0.010
Amplitude	0.1W	+0.013
Width(W)	0.5Nom	+0.017
Distance	$-0.42C_{ax}$	+0.037
$\bar{\eta}_{\text{trial avg}}$		0.345
Σ contrib		+0.078
$\bar{\eta}_{\text{opt}}$		0.423

Table 3.9. Thermal ANOVA - Case #2

Factor	DOF	TSS	MSS	F-Ratio	α
Phase	5	3.642	0.728	2.680	0.131
Amplitude	2	3.375	1.687	6.209	0.035
Width(W)	2	7.575	3.788	13.94	0.006
Distance	2	29.89	14.94	54.99	0.000
Error	6	1.631	0.272		
Total	17	46.11			

jected during error pooling).

After error pooling, upstream distance is computed as the dominant factor contributing nearly 62% of all variability. This is not surprising since upstream distance was identified as the most sensitive parameter when examining the parameter level contributions. Average slot width is also significant contributing approximately 13.5% percent influence on total variability. Finally, factors unaccounted for contribute the remaining 24.5% of variability. This is likely due to coupling of the upstream distance and average width effects. Varying the average width of the leakage path directly controls the average momentum flux ratio of the injected coolant while moving the slot axially varies the local momentum flux ratios as the pressure field across the slot exit varies with distance from the downstream vanes. Revised estimates of optimal configuration performance after pooling are given in Table 3.7. Using the pooled estimates, average thermal enhancement is predicted to range between $\pm 5\%$ with respect to the baseline, two-dimensional configuration.

3.8.3 Case #3 Inlet Conditions

Average parameter level contributions at the inlet conditions prescribed by case #3, with a near-wall peaked velocity/total pressure profile (Figure 3.3) and $1.0\% \dot{m}_{ex}$ slot flow, are illustrated in Figure 3.7. Average effectiveness levels are generally higher than for case #1 but lower than case #2 despite increased coolant flow. This is because the horseshoe vortex is more well-

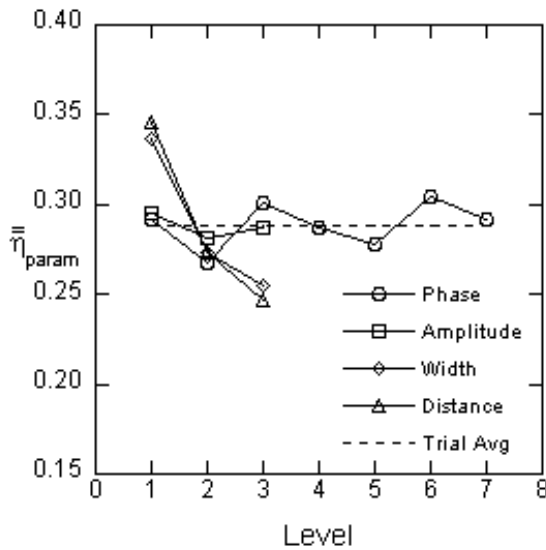


Figure 3.7. Mean parameter thermal effects for case #3.

developed as a result of the near-wall total pressure gradient of the peaked velocity profile. As for the case #1 and case #2 inlet conditions, the largest and most sensitive contributing factor is the slot upstream distance, which exhibits moderate non-linearity, increasing in sensitivity, as the leakage geometry is moved downstream towards the vanes.

At the narrowest level ($W = 0.5\text{Nom}$), the slot width parameter contributes nearly as much performance benefit as the downstream most slot location. High sensitivity to variation of the slot width is also seen with some non-linearity as the gap is widened. The increase in performance gain and sensitivity of the slot width parameter between operating conditions likely results from the larger gains in coolant momentum flux ratio (0.05 to 0.47) as the leakage path is expanded and contracted at the higher flow rate. The effectiveness gain with momentum from the expanded slot to the nominal slot is slightly lower than for cases 1 and 2 at $\Delta\bar{\eta}/\Delta I = 0.280$ from level three to level two, but is more than double the other cases when contracting the slot from level two to one where $\Delta\bar{\eta}/\Delta I = 0.178$. Cardwell et al. [9] showed that wide ranges of coolant momentum flux ratio had a significant impact on coverage area leading to more uniform coolant distribution.

Two periods of cyclic effects are again observed for the phase shift, but the periods are of equal length rather than a shorter period on the pressure side exhibited for the other inlet conditions. The largest performance gain, where $\bar{\eta} = 0.305$, is seen when the phase is shifted to 300° , just to the pressure side of the leading edge. A slightly lower peak of $\bar{\eta} = 0.301$ is observed for a 120° phase shift near the center of the passage.

As with the other cases, the amplitude parameter effect is highly non-linear with a trough at an amplitude equal to half of the average slot width. Average performance improves if the slot geometry is flattened out yielding more uniform injection or if the waveform is amplified promoting injection only in the open

Table 3.10. Estimated Thermal Contribution of Parameters at Optimal Configuration for Case #3 Inlet Conditions

Parameter	Level	$\bar{\eta}$ contrib
Phase	300°	+0.017
Amplitude	0.1W	+0.007
Width(W)	0.5Nom	+0.048
Distance	$-0.42C_{ax}$	+0.057
$\bar{\eta}_{trial\ avg}$		0.288
$\Sigma\ contrib$		+0.129
$\bar{\eta}_{opt}$		0.417

Table 3.11. Thermal ANOVA - Case #3

Factor	DOF	TSS	MSS	F-Ratio	α
Phase	5	6.153	1.231	2.275	0.173
Amplitude	2	1.157	0.578	1.069	0.401
Width(W)	2	44.52	22.26	41.15	0.000
Distance	2	63.80	31.90	58.98	0.000
Error	6	3.245	0.541		
Total	17	118.9			

areas. For these inlet conditions the highest area-averaged effectiveness, $\bar{\eta} = 0.296$, is achieved with minimal scalloping.

The optimal configuration for the case #3 inlet conditions is listed in Table 3.10. The endwall-averaged adiabatic effectiveness level is expected to be $\bar{\eta}_{opt} = 0.417$, an improvement over the baseline configuration performance, $\bar{\eta}_{baseline} = 0.329$.

The ANOVA table for the rms adiabatic wall temperature characteristic is listed in Table 3.11. It is seen that the average slot width and upstream distance parameters are well below the 95% cutoff values of $\alpha \leq 0.05$. The phase and amplitude parameters on the other hand should be pooled with the error term. Total variability, TSS, is more than twice that of the other cases indicative of the increased sensitivities exhibited in the parameter level effects plot.

After parameter pooling the percentage influence of the upstream slot location is estimated at nearly 52.5% while 36% of total variation is attributed to the average slot width. As the slot is contracted and the momentum flux ratios of the leakage coolant vary more widely, the effects begin to balance level of influence with the upstream distance where leakage flow has longer to interact with hot mainstream gases. Approximately 11.5% of variability at the case #3 inlet conditions arises because of factors that were unaccounted for in the experimental design. In this case it is likely that the coupling between the upstream distance and slot momentum flux ratio is increasing as higher momen-

tum flux ratios are seen. There may also be some interaction effects between these two parameters and the slot waveform phase which has some effect over coolant coverage distribution. Pooled estimates of the optimal configuration thermal performance characteristic are listed in Table 3.7. A significant thermal benefit is expected with respect to the baseline configuration ranging from an increase of 12.7% to 26.6%.

3.8.4 Signal-to-Noise Ratio Analysis

Frequently the exact operating conditions for a design in service may not be known completely. In this case design robustness must be evaluated during the development process. This generally involves testing with perturbed inlet conditions and was the motivation for the three cases of the current study. In this instance the three cases were selected as two extremes: one with low blowing and a near-wall total pressure deficit at the inlet and the other with high blowing and a peaked total pressure profile. The third case specified moderate blowing with a blunt inlet total pressure profile.

Examining the results listed in Tables 3.5, 3.8, and 3.10, it is observed that the optimal configuration is slightly different for each case. Some method is required to select an overall “best” configuration. One method of evaluating design robustness would be to average the performance characteristic across all tested conditions and select the best performing trial configuration or parameter combination. While this method may identify the condition with the most desirable mean response, it gives no information concerning the population distribution. In an extreme example consider the case where two configurations have identical means. Which one is best? The configuration with less variability would be more desirable as it is less sensitive to off-nominal operating conditions and thus more predictable.

The mean-squared deviation (MSD) is a characteristic, which incorporates both the population mean and variance. For the current study the goal was to reduce adiabatic endwall temperature to extend component life. Therefore, a smaller-is-better characteristic is appropriate. MSD is computed as:

$$MSD = \left(\bar{\bar{T}}_{ew,avg} \right)^2 + \sigma^2 = \frac{1}{n} \sum_{i=1}^n \left(\bar{T}_{ew,i} \right)^2 \quad (3.5)$$

where $\bar{\bar{T}}_{ew,avg}$ is the root-mean-squared endwall temperature averaged across all inlet condition cases and σ^2 is the variance. It is seen that MSD can be lowered by reducing the variance or lowering the average endwall temperature.

Frequently mean-squared deviation is expressed as a signal-to-noise ratio, S/N, as defined in Eq. 3.6 [15].

$$S/N = -10 \log_{10} MSD \quad (3.6)$$

The logarithmic expression allows evaluation of a wider range of data and tends to linearize results while the $(-)$ insures that S/N

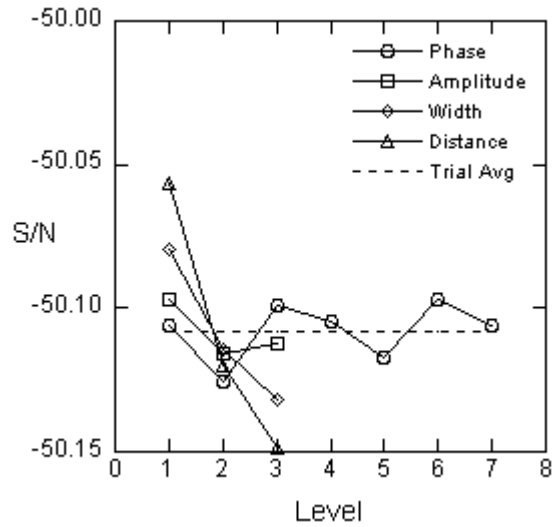


Figure 3.8. Parameter effects on signal-to-noise ratio.

grows as MSD gets smaller. The improved linearity allows for interpolation and extrapolation and is fundamental to successfully predicting performance improvement in the optimum configuration. Conceptually S/N is the ratio of the mean to variability about the mean. Therefore a larger S/N is always desirable.

A factor effects plot for signal-to-noise ratio computed from the rms adiabatic wall temperatures for each trial configuration over all three cases is shown in Figure 3.8. As with the analysis for the separate cases, slot upstream distance is seen as the dominant and most sensitive factor. Strong linearity is exhibited with S/N increasing as the injection location is moved downstream toward the passage. Average slot width is also seen to have a strong influence with performance improving as the leakage gap is narrowed accelerating the coolant toward higher momentum ratios. The amplitude parameter exhibits a highly non-linear effect with the worst performance resulting from moderate scaloping. Finally the phase parameter indicates two periods of enhancement as the slot area distribution is shifted across the passage. The most robust level is 300° (level six), which is shifted slightly to the pressure side of the vane’s dynamic stagnation location. The optimal parameter configuration is listed in Table 3.12 while S/N of the baseline, two-dimensional configuration was -50.049.

The ANOVA table computed from S/N values is given in Table 3.13. The upstream distance and average width parameters are shown to have strong significance while the phase and amplitude parameters are rejected during error pooling. After pooling the upstream slot location is computed to contribute nearly 67.5% of robustness variability while average slot width is attributed with approximately 20.5% influence. Factors that were not accounted for contribute the remaining 12% as there is likely a coupling effect between the upstream distance and average width affecting the local coolant leakage momentum flux ratios.

After parameter pooling the expected range of the optimal

Table 3.12. Estimated S/N contribution of parameters at optimal configuration

Parameter	Level	S/N contrib
Phase	300°	+ 0.011
Amplitude	0.1W	+ 0.011
Width(W)	0.5Nom	+ 0.029
Distance	-0.42C _{ax}	+ 0.054
S/N _{trial avg}		-50.108
Σ contrib		+ 0.104
S/N _{opt}		-50.004

Table 3.13. Thermal ANOVA - Signal-to-Noise Ratio

Factor	DOF	TSS	MSS	F-Ratio	α
Phase	5	0.002	0.000	3.656	0.073
Amplitude	2	0.001	0.001	5.919	0.038
Width(W)	2	0.009	0.004	42.34	0.000
Distance	2	0.027	0.014	133.4	0.000
Error	6	0.001	0.000		
Total	17	0.039			

configuration signal-to-noise ratio is $S/N_{opt} = -50.027 \pm 0.019$ for a 95% confidence interval. This translates to adiabatic effectiveness characteristics averaged over all three cases of $0.333 \leq \bar{\eta} \leq 0.369$ as indicated in Table 3.7. An average improvement of 0.7% to 10% is predicted over the baseline, two-dimensional slot configuration.

3.8.5 Validation Simulations

The optimal parameter configuration, identified in Table 3.12, was simulated for all three inlet condition cases for validation. Computed endwall-averaged adiabatic effectiveness levels are listed in Table 3.14. For the case #1 inlet conditions, an improvement of 1.9% over the baseline configuration was realized at the cost of a 7.8% increase in total pressure loss coefficient in the span from $0 \leq z/S \leq 0.15$. For the case #2 and 3 inlet conditions, more substantial thermal gains were realized with less effect on total pressure loss. The thermal signal-to-noise ratio was $S/N = -49.999$, slightly better than the predicted bounds, while the average adiabatic effectiveness level across all inlet conditions was $\bar{\eta}_{avg} = 0.374$.

Contours of endwall cooling effectiveness for the baseline configuration and optimal thermal configuration are shown in Figures 3.9 and 3.10. For case #1 coolant injection is spread across the entire width of the slot in the optimized configuration. This yields a slight amount of coolant upstream of the leading edge film-cooling holes, but has a larger effect by sig-

Table 3.14. Performance Characteristics of Optimal Thermal Configuration from Validation Simulations

Inlet Cond	$\bar{\eta}_{opt}$	$\bar{\eta}_{opt}/\bar{\eta}_{baseline}$	C _{Po} /C _{Po,baseline}
Case #1	0.278	1.019	1.078
Case #2	0.422	1.058	1.028
Case #3	0.423	1.285	1.004

nificantly widening slot coolant coverage area at the leading row of holes upstream of the center of the passage. Coolant coverage is broader in the upstream section of the passage while adiabatic effectiveness levels are slightly lower as coolant is more evenly distributed. The horseshoe vortex appears slightly more intense in the optimized configuration drawing the pressure side film-cooling jets of the upstream film-cooling row upstream and slightly widening the the uncooled ring around the vane shoulder on the suction side. The pressure side film-cooling rows within the passage appear largely unaffected at this low coolant leakage rate.

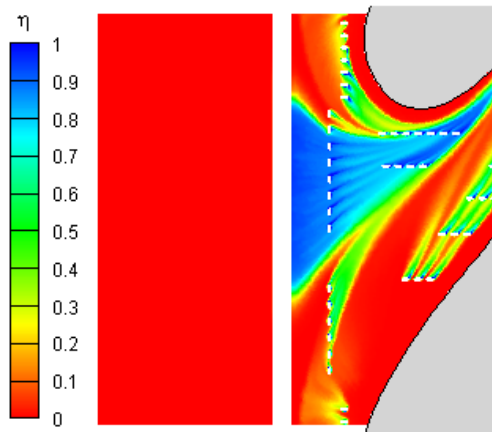
For the case #2 inlet conditions, the coolant injection area is again spread across the entire slot with coverage significantly improved upstream of the leading edge film holes. Cooling levels are lowered in the upstream center of the passage as leakage flow from the center of the slot is slightly restricted by the scalloping. Secondary flows appear slightly stronger for the optimized geometry as the leading edge film-cooling jets at the pressure side are drawn upstream by the horseshoe vortex while the uncooled area at the vane-endwall junction is expanded along the suction side. Within the passage film-coolant from the pressure side jets is drawn further into the center of the passage eliminating the thin hotstreak seen for the baseline configuration.

Finally, slot coverage and cooling levels are significantly improved upstream of the leading edge as a result of the higher leakage momentum and slight coolant concentration in this area for case #3. Slot flow coverage is broader in the upstream portion of the passage while cooling levels are slightly lowered just upstream of the film-cooling holes near the shoulder as coolant is more evenly distributed. The legs of the horseshoe vortex appear closer to the vane as the uncooled areas at the shoulder and upstream portion of the endwall along the pressure side-endwall junction appear narrower.

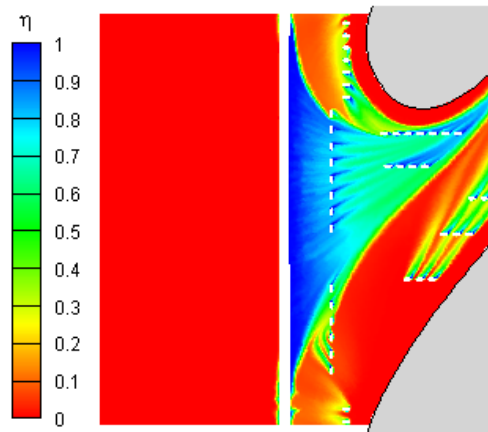
3.9 CONCLUSIONS

A computational, parametric investigation of a three-dimensional combustor-turbine interface slot was conducted using orthogonal array experimental design, parameter mean-effects estimation, and analysis of variance. RMS adiabatic end-wall temperature, selected to emphasize hotspots, was used to evaluate overall cooling effectiveness.

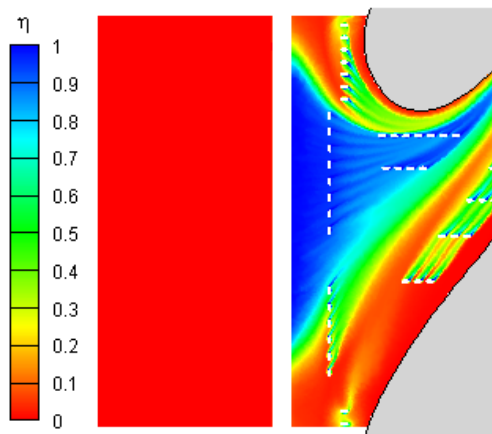
Slot distance upstream of the passage was found to be the dominant factor for all inlet conditions. At the lowest leakage flow rate, mild non-linearity was seen with decreased sensitivity



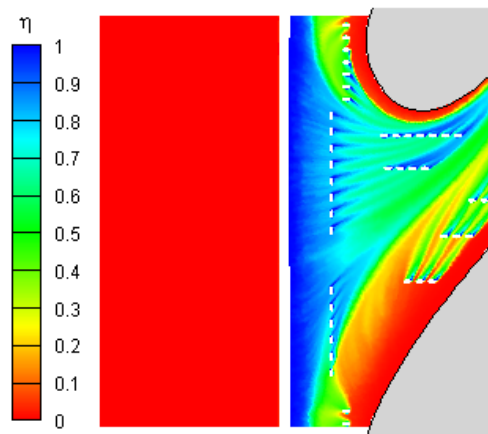
(a) CASE #1



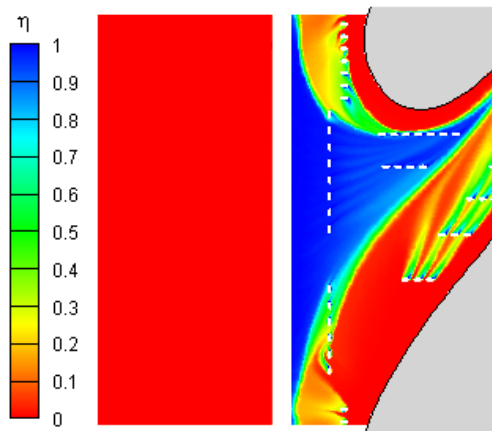
(a) CASE #1



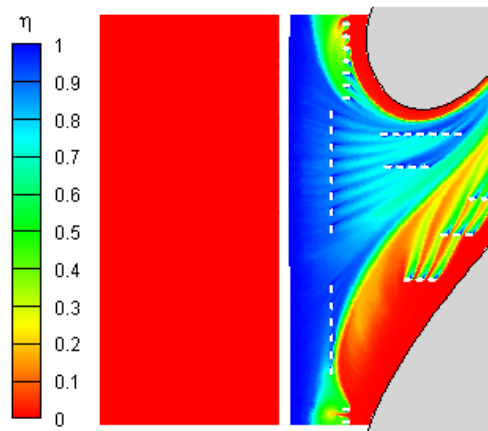
(b) CASE #2



(b) CASE #2



(c) CASE #3



(c) CASE #3

Figure 3.9. Contours of adiabatic effectiveness for the baseline, two-dimensional configuration at all cases.

Figure 3.10. Contours of adiabatic effectiveness for the optimal thermal configuration at all cases.

as the slot centerline was moved further upstream. Linearity improved at higher blowing rates with the most linear response for case #2 where horseshoe vortex development was minimized because of the blunt inlet total pressure profile. Average slot width gained influence as leakage flow rate increased with nearly the same impact as upstream distance at the highest blowing rate. The average slot width effect was non-linear, though, decreasing in sensitivity as the slot was narrowed despite increased momentum flux. Slot waveform amplitude and phase were found to have no significant effect on overall endwall cooling levels for any inlet condition combination, however, both have been shown previously to alter endwall coolant distribution and local cooling.

Slot configuration robustness was evaluated by the signal-to-noise ratio method prescribed by Taguchi. As for each individual case, slot upstream distance and average width were determined to be the most significant factors. The optimal configuration consisted of a slightly scalloped geometry with a phase offset to the pressure side of the stagnation point. The slot was contracted to 50% of the baseline slot width and stationed at the nearest upstream location to the vanes. Area-averaged endwall adiabatic effectiveness levels were increased for all cases as coolant coverage area was expanded and local cooling levels were more evenly distributed.

NOMENCLATURE

A waveform amplitude, area
 C_{ax} vane axial chord
 C_{Po} total pressure loss coefficient, $(P_{o,out} - P_{o,in})/0.5\rho U_{in}^2$
D upstream distance to slot centerline
 \dot{m} mass flow rate
MSD mean-squared deviation, $(1/n)\sum_{i=1}^n T_i^2$
n number of samples
P vane pitch
S/N signal-to-noise ratio, $-10\log_{10} MSD$
T temperature
U inlet flow velocity
W average slot width
x,y,z local coordinate system
X,Y,Z global coordinate system

Greek

α 1-confidence interval
 η endwall adiabatic effectiveness, $(T_{in} - T)/(T_{in} - T_c)$
 ϕ waveform phase
 ρ density
 σ standard deviation

Subscripts

c coolant
ew endwall
in domain inlet
opt optimal
out domain outlet

REFERENCES

- [1] Blair, M. F., 1974. "An Experimental Study of Heat Transfer and Film Cooling on Large-Scale Turbine Endwalls". *J. of Heat Transfer*, pp. 524–529.
- [2] Granser, D., and Schulenberg, T., 1990. "Prediction and Measurement of Film Cooling Effectiveness for a First-Stage Turbine Vane Shroud". 90-GT-95.
- [3] Roy, R. P., Squires, K. D., Gerendas, M., Song, S., Howe, W. J., and Ansari, A., 2000. "Flow and Heat Transfer at the Hub Endwall of Inlet Vane Passages - Experiments and Simulations". 2000-GT-198.
- [4] Nicklas, M., 2001. "Film-Cooled Turbine Endwall in a Transonic Flow Field: Part II - Heat Transfer and Film-Cooling Effectiveness Measurements". 2001-GT-0146.
- [5] Kost, F., and Mullaert, A., 2006. "Migration of Film-Coolant from Slot and Hole Ejection at a Turbine Vane Endwall". GT2006-90355.
- [6] Oke, R., and Simon, T., 2002. "Film-Cooling Experiments with Flow Introduced Upstream of a First Stage Nozzle Guide Vane Through Slots of Various Geometries". GT2002-30169.
- [7] Knost, D. G., and Thole, K. A., 2005. "Computational predictions of endwall film-cooling for a first stage vane". *International J. of Turbo and Jet Engines*, **22**, pp. 41–58.
- [8] Knost, D. G., and Thole, K. A., 2005. "Adiabatic Effectiveness Measurements of Endwall Film-Cooling for a First Stage Vane". *J. of Turbomachinery*, **127**, pp. 297–305.
- [9] Cardwell, N., Sundaram, N., and Thole, K. A., 2006. "The Effects of Varying the Combustor-Turbine Gap". GT2006-90089.
- [10] Lynch, S. P., and Thole, K. A., 2007. "The Effect of Combustor-Turbine Interface Gap Leakage on the Endwall Heat Transfer for a Nozzle Guide Vane". GT2007-27867.
- [11] Radomsky, R. W., and Thole, K. A., 2000. "Flowfield Measurements for a Highly Turbulent Flow in a Stator Vane Passage". *J. of Turbomachinery*, **122**, pp. 255–262.
- [12] Hermanson, K., and Thole, K. A., 2000. "Effect of Inlet Profiles on Endwall Secondary Flows". *J. of Propulsion and Power*, **16**, pp. 286–296.
- [13] Knost, D. G., Thole, K. A., and Duggleby, A., 2009. "Evaluating a Three-Dimensional Slot Design for the Combustor-Turbine Interface". GT2009-60168.
- [14] Fluent Inc., 2006. *Fluent 6.3 User's Guide*. (Fluent Inc: New Hampshire).
- [15] Taguchi, G., Chowdhury, S., and Wu, Y., 2005. *Taguchi's Quality Engineering Handbook*. John Wiley & Sons, Hoboken, NJ.

4 Parametric Investigation of the Combustor-Turbine Interface
Leakage Geometry: Part II - Secondary Flows - *Journal of
Turbomachinery*, in submission

GT2010-XXXX2

PARAMETRIC INVESTIGATION OF THE COMBUSTOR-TURBINE INTERFACE LEAKAGE GEOMETRY: PART II - SECONDARY FLOWS

D.G. Knost*

Mechanical Engineering
Virginia Tech
Blacksburg, Virginia 24061

K.A. Thole

Mechanical and Nuclear Engineering
The Pennsylvania State University
State College, Pennsylvania 16802

A. Duggleby

Mechanical Engineering
Texas A&M University
College Station, Texas 77843

ABSTRACT

Secondary flows have been attributed with increased heat transfer to the nozzle guide vane endwall and aerodynamic losses through the passage. For a conventional two-dimensional slot between the combustor and turbine endwalls, leakage flow typically emerges near the center of the passage. By manipulating the slot geometry, it may be possible to strategically concentrate leakage injection altering secondary flow development.

This paper presents a computational investigation of a scalloped slot configuration. Part I of this study investigated the effects of four parameters on endwall cooling levels, while part II evaluated the same parameters to determine the influence of each on total pressure loss in the near-wall region. Amplitude of a waveform defining the downstream edge of the slot was found to be the most significant factor, lowering total pressure loss with increased peaking. Strong coupling effects between parameters were also found. Inducing early development of the horseshoe vortex and intensifying endwall crossflow was found to lower pressure loss in the passage by combining regions of vorticity associated with the passage vortex and film-coolant injection near the vane shoulder.

4.1 INTRODUCTION

Gas turbines are manufactured as many components and assembled to form a turbine disc. This procedure inherently leaves many small gaps between parts which are sealed and pressurized to avoid hot gas ingestion. Some bypass leakage flow injects through the gaps into the main flow path. One such gap is the slot formed by the combustor-turbine endwall junction. Slot leakage flow has been shown to provide some thermal benefit to the inlet nozzle guide vane endwall. Part I [1] of this study

presented a parametric evaluation of a three-dimensional slot geometry with the goal of improving cooling effectiveness from leakage flow. Upstream distance to the slot was found to dominate endwall cooling levels with higher effectiveness the closer the slot moved to the vanes. Average slot width became significant at mass flow rates where leakage momentum flux ratio varied widely as the slot was contracted. High momentum flux from the narrowest slot was shown to contribute nearly as much improvement in cooling level as upstream distance at the highest leakage flow rate.

Part II of this study examined the effects of varying the slot leakage geometry on secondary flow development and total pressure loss through the passage. Secondary flows develop because of pressure gradients in the low momentum near-wall fluid. The results presented quantify the relative influence on total pressure loss of four slot geometry parameters and suggest a configuration to minimize total pressure loss in the near-wall region. Secondary flows and thermal fields are compared for a baseline two-dimensional slot, the thermally optimized geometry presented in part I, and the aerodynamically optimized configuration identified in this paper.

4.2 RELEVANT PAST STUDIES

The endwall flowfield of a first stage turbine vane has several complex features attributed with high heat transfer and aerodynamic losses. These features, commonly referred to as secondary flows, also tend to sweep coolant from component surfaces replacing it with hot core flow gases.

Flowfield studies by Langston et al. [2], Sharma and Butler [3], Goldstein and Spores [4], and others agreed on the dominant structures for a uniform approach flow with a two-dimensional turbulent boundary layer. As the flow stagnates ap-

*Address all correspondence to this author. email: dknost@vt.edu

proaching the vane, the horseshoe vortex develops because of the low momentum boundary layer with legs extending around the pressure and suction sides of the vane. Endwall crossflow within the passage due to vane turning amplifies the pressure side leg of the horseshoe vortex forming the passage vortex.

Hermanson and Thole [5] demonstrated that secondary flow development varied with inlet total pressure profile. For a turbine with combustor film-cooling and dilution flows, they suggested that a near-wall peaked total pressure profile may be more appropriate than an iso-thermal turbulent boundary layer. The total pressure peak, resulting from much cooler near-wall fluid, resulted in upward turning of the flow above a fixed spanwise station and a counter-rotating vortex within the passage. Colban et al. [6] confirmed these predictions with measurements featuring a backward facing slot configuration.

Kost and Nicklas [7] observed that the horseshoe vortex was intensified by blowing from an upstream slot when compared to no blowing. This effect resulted from injection near the separation point. Kost and Mullaert [8] showed lower losses and better cooling for the same geometry when the slot was moved further upstream.

Secondary flow development has been investigated by several researchers, while few have examined the impact of blowing from an upstream slot. This work seeks to evaluate the influence of slot geometry on total pressure losses resulting from secondary flows. A range of inlet conditions are investigated and the secondary flow and thermal fields are analyzed to determine the mechanisms of total pressure loss reduction within the passage.

4.3 THREE DIMENSIONAL SLOT GEOMETRY

A scalloped slot defined by four parameters was evaluated to determine the effect that each had on total pressure loss through the passage. The four parameters, discussed at length by Knost et al. in [9] and part I [1] of this study, were slot waveform amplitude, waveform phase, average width, and upstream distance.

The amplitude was measured as maximum deviation from the average downstream edge, indicated by the dash-dash line in Figure 4.1. Amplitude was expressed as a fraction of the average slot width, W . Large amplitude scalloping was intended to localize leakage flow injection.

Waveform phase was also considered. Phase was measured from a zero degree reference directly upstream of the vane stagnation. Adjusting waveform phase was intended to shift leakage injection laterally across the endwall.

Average slot width was varied as a means of adjusting average leakage momentum flux ratio. Average width was measured from the upstream edge of the slot to the average centerline of the downstream edge indicated by the dash-dash line in Figure 4.1. Slot widths were referenced to the nominal width of a baseline, two-dimensional configuration.

Upstream distance to the slot centerline was adjusted to alter the influence of the vane. Moving the slot further upstream improved leakage discharge uniformity as endwall pressure variations were reduced over the slot area. Upstream distance was

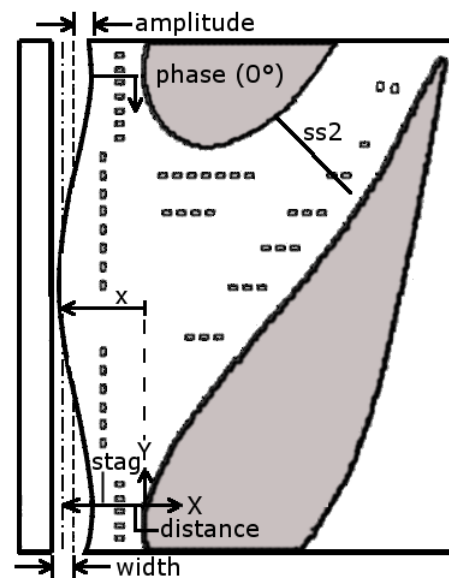


Figure 4.1. Four parameters, amplitude, phase, average width, and upstream distance, were investigated.

Table 4.1. Inlet Conditions for Various Cases

Inlet condition	Case #1	Case #2	Case #3
Inlet profile	Turb BL	Uniform	Peaked
Slot leakage rate	$0.5\% \dot{m}_{ex}$	$0.75\% \dot{m}_{ex}$	$1.0\% \dot{m}_{ex}$
Film-coolant rate	$0.5\% \dot{m}_{ex}$	$0.5\% \dot{m}_{ex}$	$0.5\% \dot{m}_{ex}$

measured from the vane stagnation to the average slot centerline, indicated by a dash-dot line in Figure 4.1, between the slot upstream and downstream edges.

4.4 INLET CONDITIONS

Three inlet condition cases were simulated, listed in Table 4.1. The cases were intended to evaluate a wide range of inlet total pressure profiles and slot blowing rates. The film-cooling flow rate was maintained for all cases and the inlet temperature profile was uniform to insure that all variability was due to variation in the slot leakage flow.

Case #1 was a low blowing condition with a turbulent boundary layer velocity profile at the inlet. The turbulent boundary layer was originally presented by Hermanson and Thole [5]. Case #2 featured a moderate slot blowing rate, halfway between cases one and three, and a uniform inlet velocity. This combined with the uniform inlet temperature yielded a blunt total pressure profile, shown in Figure 4.2. Case #3 had the highest leakage rate, $1.0\% \dot{m}_{ex}$, and a peaked total pressure profile. Hermanson and Thole [5] argued that a peaked total pressure profile may be more realistic in operation due to cooler near-wall temperatures resulting from combustor blowing.

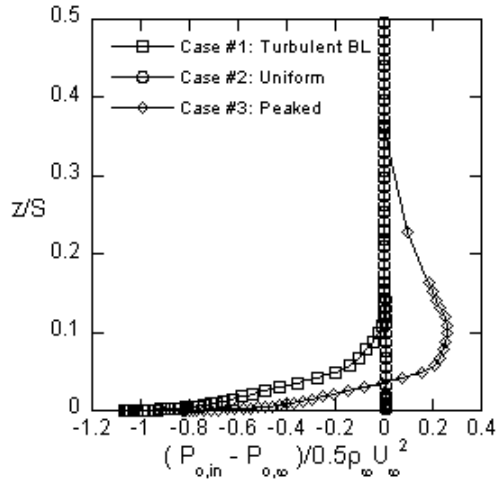


Figure 4.2. Three inlet total pressure profiles were simulated.

4.5 PERFORMANCE EVALUATION METRIC

The characteristic selected to evaluate changes in aerodynamic loss due to secondary flows was mass-averaged total pressure loss, $\Delta \bar{P}_o$, computed between the domain inlet and outlet. The mass averages were computed over the span $0 \leq z/S \leq 0.15$ as the secondary flows resided within this region. The total pressure losses were normalized by the mass averaged inlet dynamic pressure over the same span yielding a total pressure loss coefficient C_{P_o} . These characteristics are defined in Eqs. 4.1 and 4.2.

$$\bar{P}_o = \frac{\int_{CS} P_o \rho u dA}{\int_{CS} \rho u dA} \quad (4.1)$$

$$C_{P_o} = \frac{\bar{P}_{o,in} - \bar{P}_{o,out}}{\frac{1}{2} \rho u_{in}^2} \quad (4.2)$$

A lower value of total pressure loss coefficient indicated a reduction in total pressure loss through the passage. A value of zero would indicate perfect pressure recovery.

4.6 DISCUSSION OF RESULTS

The aerodynamic effects of the four parameters including: slot waveform amplitude, phase, average width, and upstream distance, were investigated using mean-effects estimation, analysis of variance, and signal-to-noise ratio. The amplitude, width, and distance parameters were evaluated at three levels, listed in Table 4.2, to qualify non-linearity. Phase was evaluated at six levels to illustrate any periodic effects. A seventh level, 360 degrees, is listed in Table 4.2 but is repeated data from level 1, zero degrees. The levels for all parameters were arranged in increasing order and evenly spaced. When examining the mean-effects plots, each parameter grows in magnitude with increasing level number.

Table 4.2. Parameter Levels for Factor Effects Plots

Parameter				
Level	Phase	Amp	Width(W)	Distance
1	0°	0.1W	0.5Nom	-0.42C _{ax}
2	60°	0.5W	1.0Nom	-0.71C _{ax}
3	120°	0.9W	1.5Nom	-1.00C _{ax}
4	180°			
5	240°			
6	300°			
7	360°			

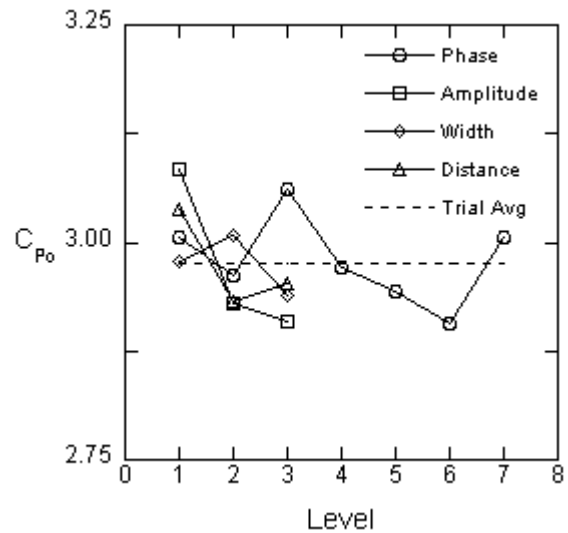


Figure 4.3. Mean parameter aero effects for case #1.

4.6.1 Case #1 Inlet Conditions

The mean-effects of the four parameters at each level listed in Table 4.2 for the inlet conditions prescribed by case #1 (from Table 4.1: 0.5% m_{ex} slot flow, turbulent boundary layer) are illustrated in Figure 4.3. The mean-effects are computed by averaging all trials containing the parameter at the level of interest and subtracting the mean response of all trials. A lower average value of C_{P_o} indicates better performance as total pressure loss through the passage is reduced.

It is seen for case #1 that waveform amplitude and phase have the largest mean effects, measured as deviation from the trial average. Total pressure loss decreases monotonically with increasing amplitude and is minimized at level 3, where amplitude was 90% of the average slot width.

Phase also exhibits large variations in mass-averaged total pressure loss with a minimum at level 6 (300°). Concentrating leakage injection upstream of the leading edge facilitates early development of the horseshoe vortex at low momentum flux ra-

tios as will be shown. Increasing slot coolant flow through the center of the passage strengthens crossflow along the endwall as shown by Knost and Thole [10]. Concentrating slot leakage just to the pressure side of the leading edge at 300° balances these effects drawing the passage vortex across the passage toward the suction side.

As the slot centerline is moved upstream from $-0.42C_{ax}$ (level 1) to $-0.71C_{ax}$, there is a marked drop in total pressure loss. The downstream most injection location is very near the separation point of the horseshoe vortex, tending to exacerbate its development. When the slot injection location is moved further upstream, this effect is alleviated. This phenomenon was also noted by Kost and Nicklas [7]. Moving the slot to the furthest upstream slot location, $-1.0C_{ax}$, yields a slightly higher value of C_{Po} as the boundary layer has more distance to redevelop.

The effect of varying the average slot width is strongly non-linear with the lowest total pressure loss from level 3, a slot that was nominally 50% wider than the baseline, two-dimensional configuration. Narrowing the average slot width accelerates the flow yielding more uniform injection, while widening the slot lowers the average momentum flux improving localization of coolant injection in the region of largest open area.

The optimal slot geometry for the case #1 inlet conditions (Table 4.2) is listed in Table 4.3 along with the optimal thermal geometry from part I [1] of this study. A highly peaked geometry that is shifted to the pressure side of the leading edge is prescribed.

Analysis of variance (ANOVA), as described in part I and many introductory statistics texts, was employed to evaluate the significance and relative influence of each of the four factors as well as factors which were unaccounted for. Using a 95% confidence interval ($\alpha \leq 0.05$) all parameters except waveform amplitude were rejected as significant contributors to variability for all three cases considered. For the case #1 inlet conditions, varying amplitude was attributed with 32.3% of variability in total pressure loss through the passage, while factors that were unaccounted for contributed the remaining 67.7%. For this case it is likely that there is coupling between the amplitude and phase factors as well as the upstream location.

Expected values of total pressure loss coefficient over the span $0 \leq z/S \leq 0.15$ for the optimal configuration listed in Table 4.3 are given in Table 4.4. The total pressure loss coefficient for the case #1 inlet conditions is expected to range between a reduction of 5% to an increase of nearly 1% over the baseline value, $C_{Po, \text{baseline}} = 3.039$.

4.6.2 Case #2 Inlet Conditions

The mean-effects plot for the case #2 inlet conditions is shown in Figure 4.4. Case #2 was characterized by $0.75\% \dot{m}_{ex}$ slot leakage flow and a blunt inlet total pressure profile, shown in Figure 4.2. As for case #1, waveform amplitude exhibits the largest effect with total pressure losses reduced as the scalloping becomes more peaked. However, this effect is much more linear

Table 4.3. Estimated Contribution of Parameters at Optimal Configuration for Case #1 Boundary Conditions

Parameter	Level	C_{Po} contrib	Thermal Opt
Phase	300°	-0.068	120°
Amplitude	0.9W	-0.065	0.1W
Width(W)	1.5Nom	-0.036	0.5Nom
Distance	$-0.71C_{ax}$	-0.042	$-0.42C_{ax}$
$C_{Po, \text{trial avg}}$		2.975	
$\sum \text{contrib}$		-0.212	
$C_{Po, \text{opt}}$		2.763	

Table 4.4. Expected Value of Optimal Configuration Total Pressure Loss Coefficient for All Inlet Conditions

Inlet Cond	$C_{Po, \text{opt}}$	$C_{Po, \text{opt}}/C_{Po, \text{baseline}}$
Case #1	2.972 ± 0.091	0.948 – 1.008
Case #2	3.139 ± 0.047	0.957 – 0.986
Case #3	3.008 ± 0.018	0.899 – 0.966
S/N	3.041 ± 0.067	0.914 – 0.955

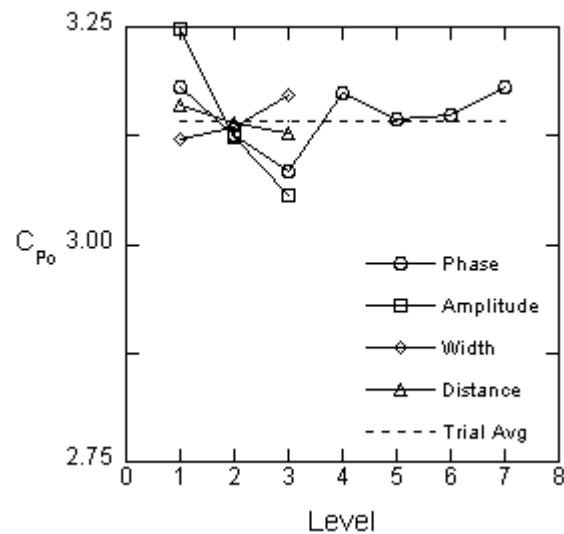


Figure 4.4. Mean parameter aero effects for case #2.

for case #2 than case #1.

The phase parameter exhibits some effect primarily when the open area is concentrated either directly upstream of the leading edge (level 1,7) or to the suction side of the center of the passage (level 3, 120°). Development of the leading edge horseshoe vortex is minimized for this inlet condition because of the blunt total pressure profile. Concentrating leakage injection directly upstream of the leading edge induces vortex development be-

Table 4.5. Estimated Contribution of Parameters at Optimal Configuration for Case #2 Boundary Conditions

Parameter	Level	C_{Po} contrib	Thermal Opt
Phase	120°	-0.059	180°
Amplitude	0.9W	-0.086	0.1W
Width(W)	0.5Nom	-0.021	0.5Nom
Distance	-1.0 C_{ax}	-0.015	-0.42 C_{ax}
$C_{Po,trial\ avg}$		3.143	
Σ contrib		-0.181	
$C_{Po,opt}$		2.962	

cause of the spanwise velocity component of the injected coolant. Shifting leakage injection primarily upstream of the center of the passage increases endwall crossflow pushing the passage vortex nearer to the center of the passage.

Increasing the average slot width increases total pressure loss in a linear fashion for case #2. The contracted slot at level 1 (50% of the baseline, two-dimensional slot width) promotes more uniform slot momentum flux. Increasing the average slot width lowers average slot momentum flux yielding more non-uniform injection. This is desirable when concentrated upstream of the passage center for the case #2 inlet conditions, but has detrimental effects upstream of the leading edge as the passage vortex remains nearer to the pressure side.

Total pressure loss coefficient also decreases linearly as the slot is moved further upstream. As the pressure effects from the vane diminish further upstream, slot momentum flux becomes more uniform. Boundary layer disturbances upstream of the stagnation have longer to dissipate maintaining total pressure uniformity.

As for the case #1 inlet conditions, only waveform amplitude is accepted as a significant contributor to total pressure loss variability for a 95% confidence interval. The amplitude parameter is attributed with 68.2% of variation while error variability, likely from coupling between the amplitude, phase, and upstream distance parameters, contributes 31.8% influence. The total variability for case #2 was only 65% of that seen for case #1, despite increased leakage flow, and approximately one third that of case #3. Despite more relative influence, less total aerodynamic effect is achievable with slot geometry manipulation in the absence of an inlet total pressure gradient.

A highly peaked slot geometry with an open area concentration positioned far upstream of the center of the passage is optimal for the case #2 inlet conditions as listed in Table 4.5. Expected values of C_{Po} incorporating ANOVA results are given in Table 4.4. A decrease in total pressure loss coefficient of 1.4%-4.3% with respect to the baseline configuration value, $C_{Po,baseline} = 3.230$, is predicted.

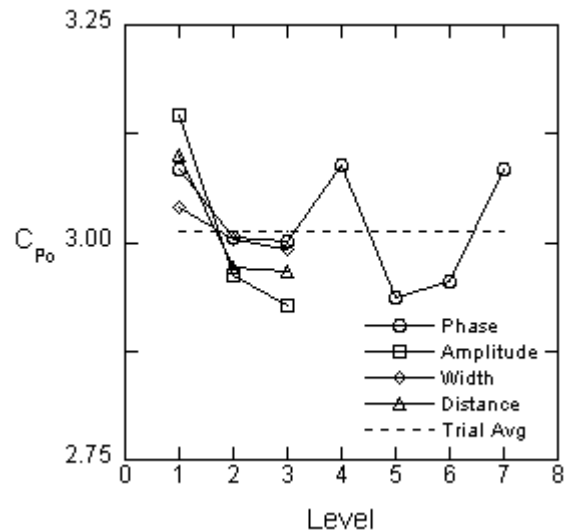


Figure 4.5. Mean parameter aero effects for case #3.

4.6.3 Case #3 Inlet Conditions

The case #3 inlet conditions included 1.0% m_{ex} slot leakage flow and a near-wall peaked total pressure profile shown in Figure 4.2. The mean parameter effects for case #3 are shown in Figure 4.5.

Mass-averaged total pressure loss decreases non-linearly with increasing waveform amplitude and is more sensitive when increased from slight to moderate scalloping (0.1W to 0.5W) than from moderate to highly peaked scalloping (0.9W).

A phase of 240 degrees (level 5), shifted to the pressure side of the center of the passage, is shown to minimize C_{Po} . Concentrating leakage flow at this station promotes horseshoe vortex development further upstream because of slot injection upstream of the leading edge. Endwall cross passage currents are also strengthened by increasing mass flow through the center of the passage. These effects combine to shift the passage vortex toward the suction side of the passage.

Total pressure loss is significantly increased for the injection location nearest the vane (level 1, -0.42 C_{ax}). As noted for case #1, this location is slightly upstream of the horseshoe vortex separation location, which is amplified by the spanwise component of the injecting leakage flow. Moving the slot further upstream significantly reduces the average value of C_{Po} with little distinction between upstream locations of -0.71 C_{ax} and -1.0 C_{ax} .

Increasing the average slot width from 50% of the baseline slot width to 150% of the baseline slot width has only a small effect reducing total pressure loss as the slot grows wider. This lowers the average momentum of the leakage flow increasing coolant flow in the region of maximum open area.

The optimal slot configuration for the case #3 inlet conditions is listed in Table 4.6. Similar to the other cases, an amplitude that is 90% of the average slot width is prescribed, but the wave phase should be shifted to 240 degrees positioning the maximum slot open area to the pressure side of the center of the

Table 4.6. Estimated Contribution of Parameters at Optimal Configuration for Case #3 Boundary Conditions

Parameter	Level	C_{Po} contrib	Thermal Opt
Phase	240°	-0.075	300°
Amplitude	0.9W	-0.084	0.1W
Width(W)	1.5Nom	-0.020	0.5Nom
Distance	-1.0 C_{ax}	-0.046	-0.42 C_{ax}
$C_{Po,trial\ avg}$		3.012	
Σ contrib		-0.225	
$C_{Po,opt}$		2.787	

passage. The slot should be stationed one axial chord upstream and expanded to 150% of the baseline slot width.

Using analysis of variance, only the wave amplitude parameter is accepted as a significant contributor to variations in total pressure loss for a 95% confidence interval. The amplitude parameter has 34.3% relative influence while factors unaccounted for contribute the remaining 65.7% of variability. Estimates of total pressure loss coefficient incorporating ANOVA data are listed in Table 4.4. A reduction of total pressure loss coefficient ranging from 3.4%-10.1% with respect to the baseline configuration value, $C_{Po, baseline} = 3.225$, is predicted.

4.6.4 Signal-to-Noise Ratio

As discussed in part I [1] of this study, the signal-to-noise ratio presented by Taguchi [11] is a useful method for evaluating design robustness. This method uses the mean-squared deviation (MSD) to identify the optimal configuration rather than a direct average of the performance characteristic over all cases. MSD is frequently expressed as a signal-to-noise ratio (S/N) to accommodate a wider range of responses and linearize results. A higher value of S/N indicates a more robust configuration. Mean-squared deviation and signal-to-noise ratio were defined as in part I, but the total pressure loss metric of Eqs 4.1 and 4.2 was substituted for the thermal metrics defined in part I.

The mean-effects plot for total pressure loss signal-to-noise ratio is shown in Figure 4.6. As for all individual cases, amplitude is shown to have the largest effect raising S/N as the wave amplitude is increased. The gain in S/N from level 1 (0.1W) to level 2 (0.5W) is nearly four times that from level 2 to level 3 (0.9W) indicating a significant decrease in sensitivity as the scalloping becomes more peaked.

Signal-to-noise ratio is improved if the phase of the slot waveform is adjusted to either side of the vane stagnation from level 1/7 to level 2 (60°) or level 6 (300°). Larger gains are seen, however, when the maximum open area is positioned to the pressure side of the vane stagnation with very little difference between 240 and 300 degrees. The true optimum likely is between these settings and dependent upon coolant blowing range and in-

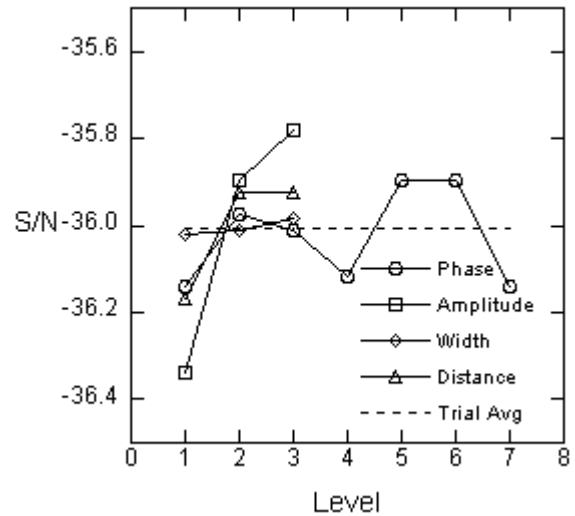


Figure 4.6. Mean parameter signal-to-noise ratios for all inlet condition cases.

let total pressure gradient.

A large improvement is seen when the slot centerline is moved upstream from $-0.42C_{ax}$ to $-0.71C_{ax}$ or $-1.0C_{ax}$. S/N is slightly higher for level 2 ($-0.71C_{ax}$), but the preferred position is dependent on the inlet total pressure profile and slot leakage rate as shown for the various cases. The location farthest upstream is most suitable for higher blowing rates.

Finally, the signal-to-noise ratio is quite insensitive to variations in average slot width. Robustness improves slightly from widening the slot as injection localization is improved by lowering the average momentum flux ratio. This is most desirable for a strong inlet total pressure gradient.

The optimal configuration for robust total pressure loss minimization is listed in Table 4.7. Highly peaked slot scalloping is specified with the maximum open area positioned at 240 degrees, shifted toward the pressure side of the center of the passage. The slot centerline is stationed $-0.71C_{ax}$ upstream of the vane stagnation, and the average slot width is 50% greater than the baseline, two-dimensional configuration.

Using analysis of variance for the S/N values, all parameters except waveform amplitude are rejected as significant contributors to total pressure loss for a 95% confidence interval. Amplitude magnitude is estimated to contribute 53.5% of variability while the remaining 46.5% is attributed to the error term. This is likely from coupling effects between the amplitude, phase, and upstream distance parameters. Including only the amplitude contribution, the signal-to-noise ratio of the optimum configuration, listed in Table 4.7, is predicted as $S/N_{opt} = -35.78 \pm 0.191$. This is converted to the range of C_{Po} values listed in Table 4.4, the expected total pressure loss coefficient when averaged over all three inlet condition cases. A reduction of C_{Po} ranging from 4.5% to 8.6% with respect to the baseline, two-dimensional configuration is predicted.

Table 4.7. Estimated Contribution of Optimal Parameter Levels to S/N

Parameter	Level	C_{Po} contrib	Thermal Opt
Phase	240°	+0.110	300°
Amplitude	0.9W	+0.224	0.1W
Width(W)	1.5Nom	+0.021	0.5Nom
Distance	-0.71 C_{ax}	+0.081	-0.42 C_{ax}
$S/N_{\text{trial avg}}$		-36.01	
Σ contrib		+0.436	
S/N_{opt}		-35.57	

Table 4.8. Performance Characteristics of Optimal Aerodynamic Configuration from Validation Simulations

Inlet Cond	$C_{Po, \text{opt}}$	$C_{Po, \text{opt}}/C_{Po, \text{baseline}}$	$\bar{\eta}_{\text{opt}}/\bar{\eta}_{\text{baseline}}$
Case #1	2.573	0.847	0.758
Case #2	2.832	0.877	0.793
Case #3	2.608	0.809	0.709

4.6.5 Validation Simulations

The optimized slot configuration listed in Table 4.7 was simulated for all three inlet condition cases to validate performance improvement. Performance characteristics are given in Table 4.8. Total pressure loss coefficient, computed from the domain inlet to outlet, was significantly reduced ranging from 12.3%-19.1% improvement with respect to the baseline, two-dimensional configuration. This was markedly better than predicted using analysis of variance to identify significant contributing factors.

Despite decreasing total pressure loss in the near-wall region, the upstream location, increased width, and large amplitude scalloping degraded endwall cooling effectiveness relative to the two-dimensional baseline geometry. Moving the slot farther upstream resulted in a longer distance for the coolant to mix with hot core flow gases while increasing the average slot width lowered leakage flow momentum. This was shown to have an adverse effect in part I [1] as the coolant distribution was neither as broad nor uniform when compared to a contracted slot.

4.7 SECONDARY FLOW AND THERMAL FIELDS

Predicted secondary flow and thermal fields were evaluated for the three slot configurations listed in Table 4.9. These included the baseline two-dimensional slot, the thermally optimized slot presented in part I [1] of this study, and the aerodynamically optimized configuration from the previous section.

The secondary flow and thermal fields are presented in two planes illustrated in Figure 4.1. The stagnation plane is parallel to the axial direction and aligned at the vane dynamic stagnation location. Plane SS2 is normal to the vane suction surface

Table 4.9. Baseline and Optimized Slot Configurations

Parameter	Optimized		
	Baseline	Thermal	Aerodynamic
Phase	0°	300°	240°
Amplitude	0.0W	0.1W	0.9W
Width(W)	1.0Nom	0.5Nom	1.5Nom
Distance	-0.42 C_{ax}	-0.42 C_{ax}	-0.71 C_{ax}

at a distance $s/C = 0.36$ along the vane surface. This plane is near the passage throat. In-plane flow vectors are depicted in the stagnation plane while secondary flow vectors, computed as deviations from the midspan streamlines and normalized by the mass-averaged inlet velocity, are shown in SS2. For the normalized thermal fields, a value of unity translates to coolant temperature and a value of zero specifies hot gas temperature. Contours of in-plane vorticity are included to aid in locating and tracking secondary flows. White lines indicate clockwise rotation about an axis normal to the plane, and black lines indicate counter-clockwise rotation.

Secondary flow and thermal fields in the stagnation plane for the baseline, two dimensional slot configuration are shown in Figure 4.7(a). Predictions for the case #1 inlet conditions, which included 0.5% \dot{m}_{ex} slot leakage flow and a turbulent inlet boundary layer, are presented. A downward turning of the flow is seen as it approaches the vane stagnation ($x/C_{ax} = 0$) rolling into the horseshoe vortex. The horseshoe vortex is centered at $-0.25C_{ax}$, as indicated by the white contours, and induces separation of the film-cooling jet injecting at the leading edge. No slot leakage flow is present upstream of the vane for this configuration, as also noted by Sundaram and Thole [12].

The stagnation plane secondary flow and thermal fields for the thermally optimized slot configuration are shown in Figure 4.7(b). The thermally optimized configuration featured a contracted slot, 50% of the width of the baseline slot, stationed $-0.42C_{ax}$ upstream of the vane stagnation point. The narrower slot increased the average momentum flux ratio of the injecting leakage flow by a factor of approximately four for a fixed flow rate. Slot coolant is shown to inject upstream of the leading edge as a result. The spanwise component of the injecting leakage flow promotes development of the horseshoe vortex leading to formation further upstream at $x/C_{ax} = -0.3$. The core of the horseshoe vortex extends higher than for the baseline configuration, reaching to approximately 3% span. The leading edge film-cooling jet appears slightly more separated injecting nearly normal to the endwall despite being directed at thirty degrees axially downstream. The secondary flow field of the aerodynamically optimized slot, shown in Figure 4.7(c), appears quite similar to that of the thermally optimized slot despite leakage injection further upstream at $-0.71C_{ax}$, but no leakage flow is evident in the stagnation plane.

Further into the passage, the secondary flow and thermal

fields in plane SS2 are depicted for the three slot configurations with the case #1 inlet conditions. For the baseline configuration shown in Figure 4.8(a), the passage vortex is evident from the secondary flow vectors and is centered at $y/P = 0.10$, $z/S = 0.02$ indicated by the white contours illustrating clockwise vorticity. A second region of clockwise vorticity corresponding to the suction side film-cooling jets near the vane shoulder is seen at $y/P = 0.06$, $z/S = 0.03$. The suction side film-cooling jets and slot coolant appear partially merged as the slot coolant is lifted above the endwall reaching nearly 7% span. The remnants of the weaker suction side leg of the horseshoe vortex are identified by the single black iso-contour positioned at $y/P = 0.05$, $z/S = 0.06$.

Figure 4.8(b) illustrates the secondary flow and thermal fields in plane SS2 for the thermally optimized slot with the case #1 inlet conditions. The secondary flow vectors appear more intense near the center of the passage vortex than for the baseline configuration. The core of the passage vortex, identified by the white in-plane vorticity contours, is larger and has moved slightly closer to the center of the passage and up from the endwall. The vorticity region associated with the suction side film-cooling holes appears nearly the same as for the baseline configuration, but the suction side leg of the horseshoe vortex is larger and more intense. The slot and film-coolant appear well merged and are swept nearly normal to the endwall by the strong updraft of the passage vortex. The suction side leg of the horseshoe vortex entrains a small amount of coolant drawing it back toward the suction side.

Secondary flow and thermal fields in plane SS2 for the aerodynamically optimized slot with the case #1 inlet conditions are shown in Figure 4.8(c). The core of the passage vortex is located farther toward the suction side of the passage than for the other two configurations. The vorticity contours associated with the suction side film-cooling holes are in the same location as for the baseline and thermally optimized configurations, but are highly skewed and more well merged with the passage vortex contours. The suction side leg of the horseshoe vortex appears similar in size and shape to that of Figure 4.8(b). The slot coolant is entrained by the passage vortex and lifted above the endwall as high as 8% of the vane span.

The stagnation plane secondary flow and thermal fields for the baseline, thermally optimized, and aerodynamically optimized slot geometries with the case #2 inlet conditions are shown in Figure 4.9. Case #2 featured $0.75\dot{m}_{ex}$ slot leakage flow and a blunt inlet total pressure profile as listed in Table 4.1 and shown in Figure 4.2.

As the flow approaches the vane, very little downward turning is predicted for the baseline slot configuration, shown in Figure 4.9(a). This is because there was no total pressure gradient imposed at the inlet as discussed by Hermanson and Thole [5]. The leading edge film-cooling jet injects downstream approaching the vane surface. No slot leakage flow is seen to emerge at $-0.42C_{ax}$.

A significant amount of coolant is present along the endwall approaching the vane for the thermally optimized slot configura-

tion, shown in Figure 4.9(b). The average slot width for this configuration was 50% narrower than the baseline. This increased the slot momentum flux ratio by a factor of approximately four, from $I = 0.07$ to 0.27. The spanwise component of the injected slot leakage flow upstream of the leading edge induces formation of a small horseshoe vortex, shown by the white contours indicating iso-values of clockwise in-plane vorticity. The small vortex lifts the leading edge film-cooling jet slightly off the endwall.

As seen in Figure 4.9(c), the horseshoe vortex develops in nearly the same location for the aerodynamically optimized slot as for the thermally optimized geometry. The vortex is slightly less intense, though, as upward motion near the endwall is lower upstream and film-cooling detachment is reduced. A small amount of coolant is present along the endwall upstream of the vane due to slot injection at $-0.71C_{ax}$.

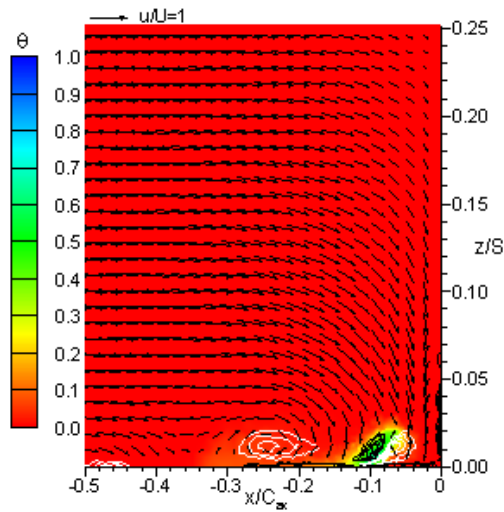
The passage vortex is not very well developed in plane SS2 for the baseline slot configuration with the case #2 inlet conditions as shown in Figure 4.10(a). The passage vortex, centered at $y/P = 0.13$, $z/S = 0.02$, is less intense and flatter than for the case #1 inlet conditions, though, strong endwall cross flows are exhibited for both cases. Vorticity contours indicating the position of the suction side film-cooling jets from near the vane shouldered are located at $y/P = 0.05$, $z/S = 0.025$. The slot leakage flow and film-coolant appear well merged and is lifted normal to endwall by the upward motion of the passage vortex. A small amount of slot coolant extends into the center of the passage vortex.

Figure 4.10(b) illustrates the secondary flow and thermal fields of the thermally optimized slot geometry in plane SS2. The passage vortex is more structured than for the baseline configuration, but is positioned slightly toward the pressure side of the passage, while the suction side film-cooling jets are centered closer to the vane suction surface. The spreading of these two clockwise vorticity regions increases C_{Po} by nearly 3% with respect to the baseline configuration [1]. The slot coolant is partially entrained by the passage vortex and does not appear well merged with the suction side film-cooling jets.

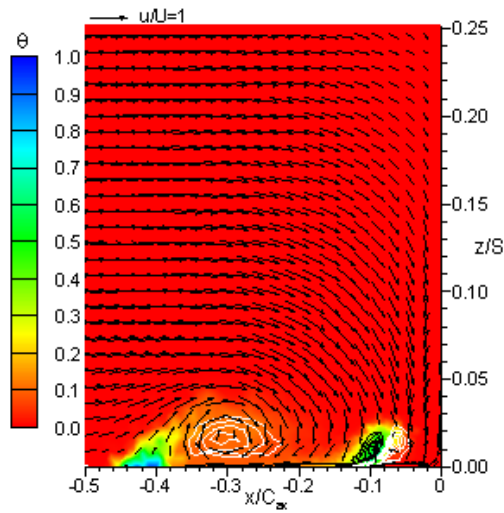
As shown in Figure 4.10(c), the passage vortex is more well developed for the aerodynamically optimized slot configuration than for either of the other slot geometries. The core of the passage vortex, indicated by white clockwise vorticity contours, is larger and more intense. It is shifted slightly toward the suction side of the passage compared to the baseline and thermally optimized configurations and is more well merged with the circulating suction side film-cooling jets. The vorticity contours of the film-cooling jets appear highly skewed. The slot coolant is entrained in the passage vortex and lifted as high as 6% of the vane span.

The flow and thermal fields in the stagnation plane for the case #3 inlet conditions are shown in Figure 4.11 for the three slot configurations. Case #3 consisted of the highest slot leakage rate, $1.0\dot{m}_{ex}$, and a total pressure profile that was peaked in the near-wall region as illustrated in Figure 4.2.

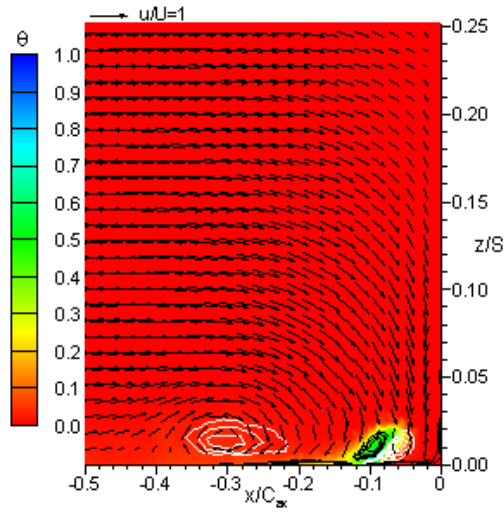
A flow split at fifteen percent span is predicted for the baseline configuration as seen in Figure 4.11(a). The flow above this



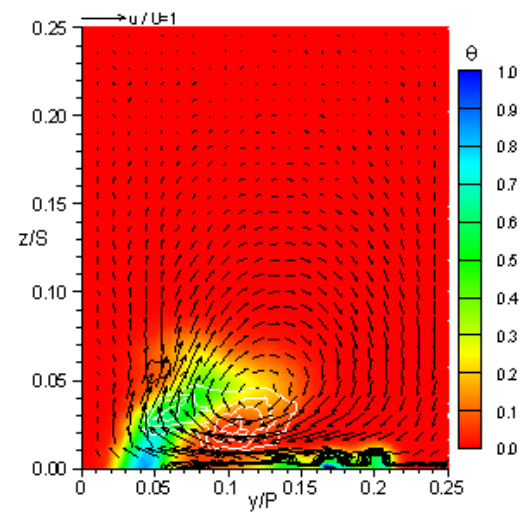
(a) baseline



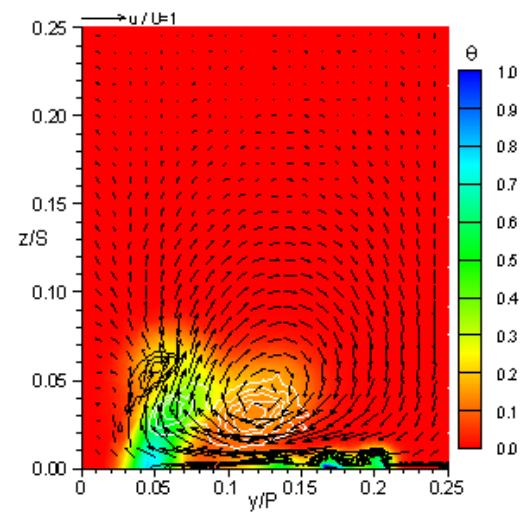
(b) thermal optimum



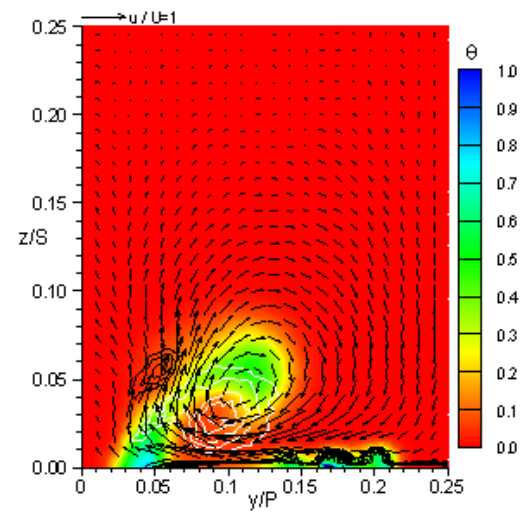
(c) aerodynamic optimum



(a) baseline



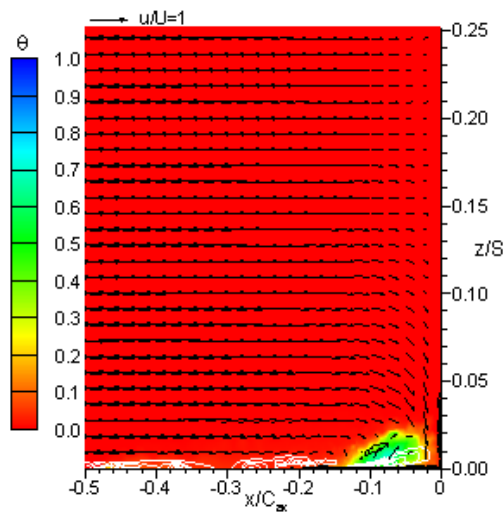
(b) thermal optimum



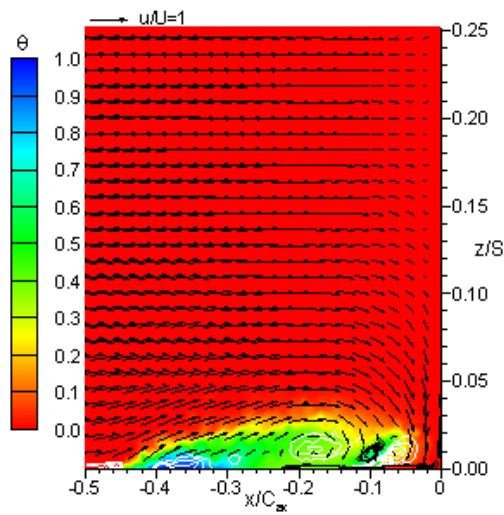
(c) aerodynamic optimum

Figure 4.7. Thermal and secondary flow fields in the stagnation plane for case #1 inlet conditions.

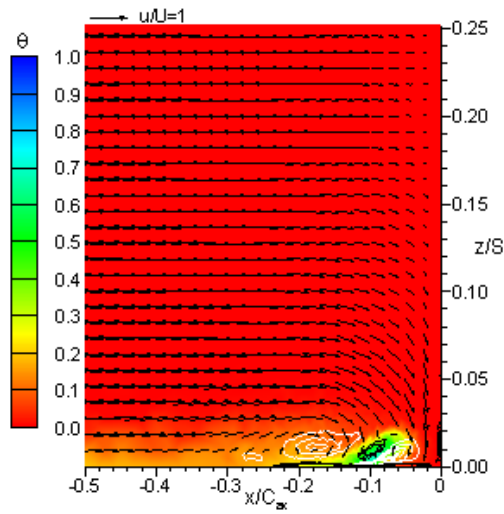
Figure 4.8. Thermal and secondary flow fields in plane SS2 for case #1 inlet conditions.



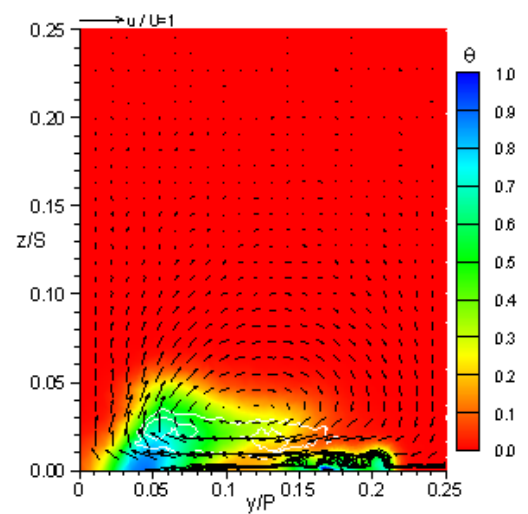
(a) baseline



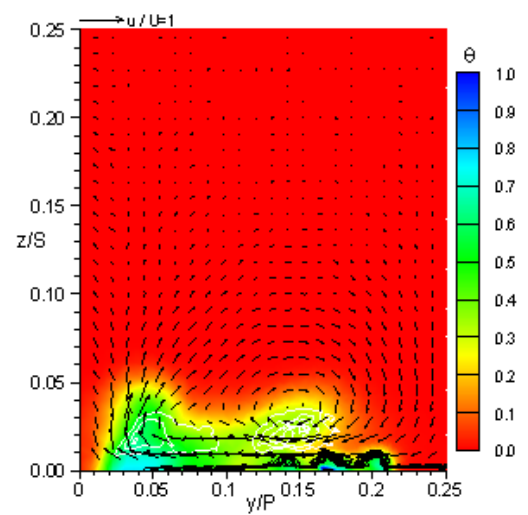
(b) thermal optimum



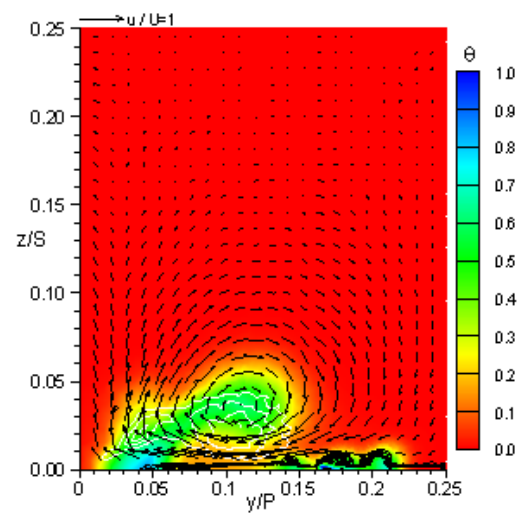
(c) aerodynamic optimum



(a) baseline



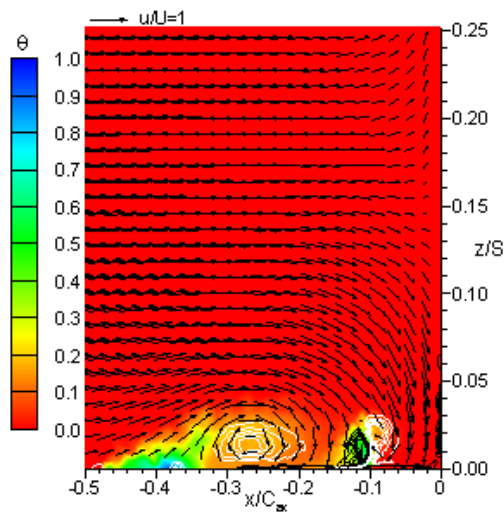
(b) thermal optimum



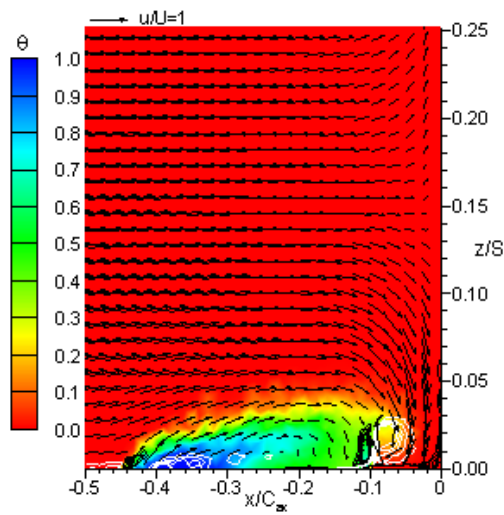
(c) aerodynamic optimum

Figure 4.9. Thermal and secondary flow fields the stagnation plane for case #2 inlet conditions.

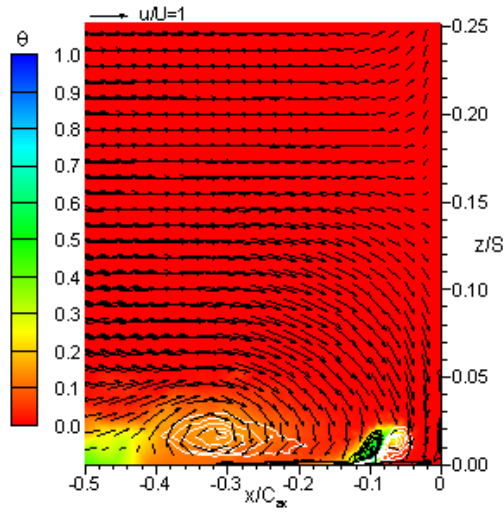
Figure 4.10. Thermal and secondary flow fields in plane SS2 for case #2 inlet conditions.



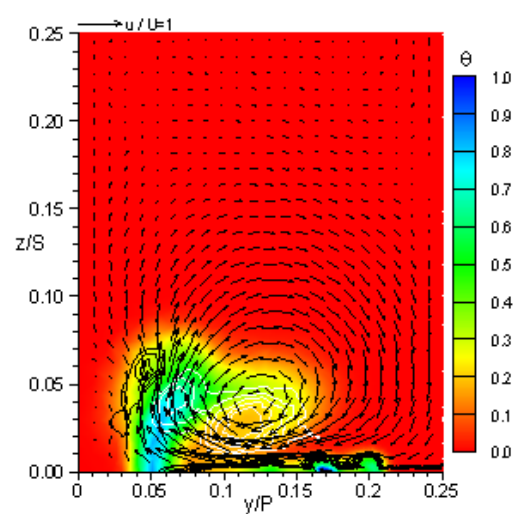
(a) baseline



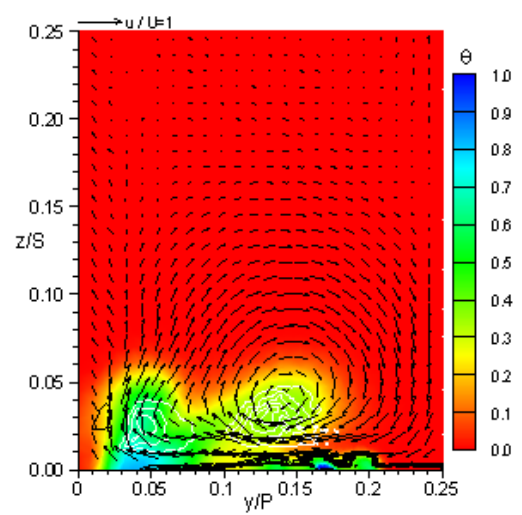
(b) thermal optimum



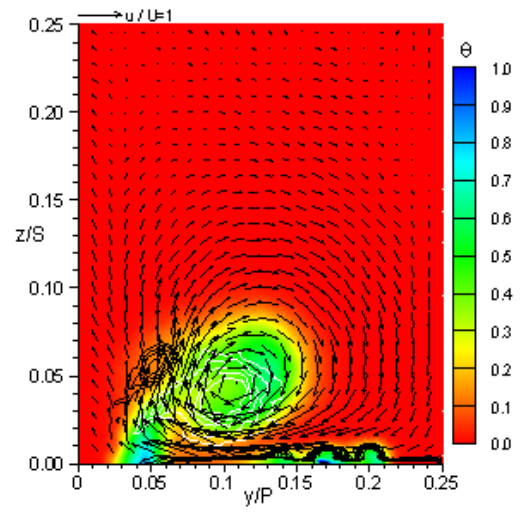
(c) aerodynamic optimum



(a) baseline



(b) thermal optimum



(c) aerodynamic optimum

Figure 4.11. Thermal and secondary flow fields in the stagnation plane for case #3 inlet conditions.

Figure 4.12. Thermal and secondary flow fields in plane SS2 for case #3 inlet conditions.

station turns up the vane surface as a result of the inlet total pressure peak. The downward turning flow below $z/S = 0.15$ rolls into the horseshoe vortex. Some leakage injection is visible at $x/C_{ax} = -0.42$ as the high blowing rate has sufficient momentum to overcome the increased pressure along the endwall upstream of the leading edge. The coolant injects near the separation point amplifying the horseshoe vortex.

The slot leakage flow is injected at a much higher momentum flux ratio from the thermally optimized configuration ($I = 0.47$ vs. 0.12), shown in Figure 4.11(b). Coolant covers the endwall up to the film-cooling jet and the horseshoe vortex development is minimized with only a small, low intensity circulation visible at $x/C_{ax} = -0.18$. Strong downward turning at the vane stagnation causes complete separation of the leading edge film-cooling jet.

For the aerodynamically optimized slot, shown in Figure 4.11(c), leakage injection further upstream at $-0.71C_{ax}$ induces earlier development of the horseshoe vortex than for the baseline and thermally optimized configurations. The horseshoe vortex is similar in size to that of the baseline configuration but slightly broader as indicated by the white vorticity contours.

The secondary flow and thermal fields in plane SS2 for the baseline slot geometry with the case #3 inlet conditions are shown in Figure 4.12(a). The passage vortex is well structured with the core centered at $y/P = 0.12$, $z/S = 0.02$. The vorticity contours corresponding to the suction side film-cooling jets are centered at $y/P = 0.07$, $z/S = 0.04$ and are partially merged with the passage vortex core. The slot and film-coolant is swept normal to the endwall as some coolant becomes entrained in the passage vortex. The suction side leg of the horseshoe vortex, identified by the black contours indicating counter-clockwise vorticity, is positioned at $y/P = 0.05$, $z/S = 0.06$. This vortex entrains a small amount of coolant drawing it back toward the suction surface.

The secondary flow and thermal fields in plane SS2 for the thermally optimized slot are presented in Figure 4.12(b). The passage vortex appears less intense than for the baseline case and is positioned slightly toward the pressure side of the passage as the endwall crossflow is weaker. The suction side film-cooling jets are stationed closer the endwall and vane suction surface than for the baseline slot configuration. The suction side film-cooling jets and passage vortex appear completely separated. Much of the slot coolant is entrained by the passage vortex and lifted off of the endwall. The suction side leg of the horseshoe vortex is much weaker than for the baseline configuration. It is positioned lower to the endwall and nearer to the vane suction surface as indicated by the single black vorticity contour ($\Omega_N C/U_{in} = -40$) at $y/P = 0.02$, $z/S = 0.03$.

The passage vortex for the aerodynamically optimized slot geometry, shown in Figure 4.12(c), is larger and more intense than for either the baseline or thermally optimized geometries. It is centered further toward the suction side of the passage, as the endwall crossflow appears stronger. The passage vortex entrains much of the slot coolant lifting it above the endwall as high as 8% of the vane span. The suction-side film-cooling jet vorticity

is much lower than for the other configurations and more well merged with the passage vortex, while the suction side leg of the horseshoe vortex appears more intense than for the other configurations.

4.8 CONCLUSIONS

Secondary flows develop as a result of pressure gradients in the low momentum fluid near the endwall. They have been attributed with increased heat transfer and total pressure loss through the passage. Secondary flows also tend to sweep up coolant and convect hot core flow gases down onto component surfaces.

A parametric investigation of a scalloped slot was performed to evaluate the possibility of reducing total pressure losses in the near-wall region by manipulating the secondary flows. The amplitude of a waveform defining the downstream edge of the slot was determined to have a significant effect on total pressure loss variation. It was also likely that coupling effects between the waveform amplitude, the pitchwise location of the region with maximum open area, and the upstream location of the slot were significant. An optimal configuration consisting of a highly peaked waveform, shifted to the pressure side of the passage center, and stationed $-0.71C_{ax}$ upstream of the leading edge was identified using signal-to-noise ratio analysis. Total pressure loss coefficient, C_{Po} , was reduced by 12%-19% in the near-wall region relative to a baseline two-dimensional slot depending upon the inlet conditions. Endwall cooling levels were 21%-29% lower than the baseline because of positioning further upstream and a wider average slot width.

Total pressure losses were reduced by two methods. Leakage injection farther upstream from the vane induced early formation of the passage vortex for inlet conditions with a near-wall total pressure deficit. Increased coolant flow through the center of the passage also strengthened endwall crossflow. Both mechanisms shifted the passage vortex laterally across the passage toward the suction surface. This integrated vorticity associated with the passage vortex and from film-cooling jets injecting near the vane shoulder. Combining these circulating flows lowered total pressure losses through the passage.

NOMENCLATURE

A	waveform amplitude, area
C_{ax}	vane axial chord
C_{Po}	total pressure loss coefficient, $(\bar{P}_{o,out} - \bar{P}_{o,in}) / 0.5\rho U_{in}^2$
I	momentum flux ratio, $\rho_c V_c^2 / \rho_{in} V_{in}^2$
\dot{m}	mass flow rate
MSD	mean-squared deviation, $(1/n) \sum_{i=1}^n (\Delta \bar{P}_{o,i})^2$
n	number of samples
P	vane pitch
P_o	total pressure
S/N	signal-to-noise ratio, $-10 \log_{10} MSD$
T	temperature
U	inlet flow velocity

W average slot width
x,y,z local coordinate system
X,Y,Z global coordinate system

Greek

α 1-confidence interval
 ϕ waveform phase
 ρ density
 θ non-dimensional temperature, $(T_{in} - T) / (T_{in} - T_c)$

Subscripts

c coolant
i measurement index
in domain inlet
opt optimal
out domain outlet
 ∞ free stream

REFERENCES

- [1] Knost, D. G., Thole, K. A., and Duggleby, A., 2010. Parametric Investigation of the Combustor-Turbine Interface Leakage Geometry: Part I - Thermal Optimization. Submitted to GT2010.
- [2] Langston, L. S., 1980. "Crossflows In a Turbine Cascade Passage". *Journal of Engineering for Power*, **102**, pp. 866–874.
- [3] Sharma, O. P., and Butler, T. L., 1987. "Predictions of Endwall Losses and Secondary Flows in Axial Turbine Cascades". *J. of Turbomachinery*, **109**, pp. 229–236.
- [4] Goldstein, R. J., and Spores, R. A., 1988. "Turbulent Transport on the Endwall in the Region Between Adjacent Turbine Blades". *J. of Heat Transfer*, **110**, pp. 862–869.
- [5] Hermanson, K., and Thole, K. A., 2000. "Effect of Inlet Profiles on Endwall Secondary Flows". *J. of Propulsion and Power*, **16**, pp. 286–296.
- [6] Colban, W. F., Lethander, A. T., Thole, K. A., and Zess, G., 2002. "Combustor-Turbine Interface Studies: Part 1: Flow and Thermal Field Measurements". *J. of Turbomachinery*, **125**, pp. 203–209.
- [7] Kost, F., and Nicklas, M., 2001. "Film-Cooled Turbine Endwall in a Transonic Flow Field: Part I - Aerodynamic Measurements". 2001-GT-0145.
- [8] Kost, F., and Mullaert, A., 2006. "Migration of Film-Coolant from Slot and Hole Ejection at a Turbine Vane Endwall". GT2006-90355.
- [9] Knost, D. G., Thole, K. A., and Duggleby, A., 2009. "Evaluating a Three-Dimensional Slot Design for the Combustor-Turbine Interface". GT2009-60168.
- [10] Knost, D. G., and Thole, K. A., 2005. "Adiabatic Effectiveness Measurements of Endwall Film-Cooling for a First Stage Vane". *J. of Turbomachinery*, **127**, pp. 297–305.

- [11] Taguchi, G., Chowdhury, S., and Wu, Y., 2005. *Taguchi's Quality Engineering Handbook*. John Wiley & Sons, Hoboken, NJ.
- [12] Sundaram, N., and Thole, K. A., 2008. "Film-Cooling Flowfields with Trenched Holes on an Endwall". GT2008-50149.

5 Conclusions and Recommendations

As turbine technology has evolved, it has become necessary to cool component surfaces because of high turbine inlet temperatures. One surface which requires thermal management is the nozzle guide vane endwall. Secondary flows, which develop as a result of a pressure gradient in the low momentum boundary layer make this a particularly difficult task.

This research focused on utilizing bypass leakage flow emerging from the combustor-turbine interface slot to cool the endwall surface. Reducing total pressure loss through the passage by affecting secondary flow development was also explored. A three-dimensional slot geometry with four parameters intended to influence leakage injection was evaluated computationally. The primary effects of the scalloping waveform amplitude and phase as well as the nominal slot width and upstream distance were presented. Design of experiments techniques, parameter mean effects estimation, and analysis of variance were also employed to optimize the slot geometry both thermally and aerodynamically for three sets of inlet conditions. The influence of all significant parameters was quantified and validation simulations were explored to determine the sources of enhancement.

5.1 Primary Effects of Three-Dimensional Parameters

Moving the slot centerline upstream facilitated more uniform coolant injection for the same momentum ratio as the pressure variation across the endwall was reduced but also degraded cooling levels within the passage as the leakage flow had longer to mix with the hot core flow. Slot coolant coverage area was not significantly impacted. Increasing waveform amplitude was shown to concentrate coolant injection in regions with more open area while coolant flow from narrow portions of the slot was restricted. Adjusting waveform phase

across the vane pitch shifted coolant injection location and altered coverage area both upstream and within the passage. Expanding and contracting the average slot width altered coolant coverage area. The higher momentum leakage flow emerging from the narrower slot penetrated closer to the vane leading edge and exhibited broader coverage area in the upstream portion of the passage.

5.2 Thermal Optimization

Slot distance upstream of the passage was found to be the dominant factor influencing RMS adiabatic endwall temperature for all inlet conditions. At the lowest leakage flow rate, mild non-linearity was seen with decreased sensitivity as the slot centerline was moved further upstream. Linearity improved at higher blowing rates with the most linear response for a blunt inlet total pressure profile where horseshoe vortex development was minimized. Average slot width gained influence as leakage flow rate increased with nearly the same impact as upstream distance at the highest blowing rate. The average slot width effect was non-linear, though, decreasing in sensitivity as the slot was narrowed despite increased momentum flux. Slot waveform amplitude and phase were found to have no significant effect on overall endwall cooling levels for any inlet condition combination, however, both were shown to alter endwall coolant distribution and local cooling.

The configuration optimized for robustness consisted of a slightly scalloped geometry with a phase offset to the pressure side of the stagnation point. The slot was contracted to 50% of the baseline slot width and stationed at the nearest upstream location to the vanes. Area-averaged endwall adiabatic effectiveness levels were increased for all inlet condition cases as coolant coverage area was expanded and local cooling levels were more evenly distributed.

5.3 Secondary Flows

A parametric investigation of a scalloped slot was performed to evaluate the possibility of reducing total pressure losses in the near-wall region by manipulating the secondary flows. The amplitude of a waveform defining the downstream edge of the slot was determined to have a significant effect on total pressure loss variation. It was also likely that coupling effects between the waveform amplitude, the pitchwise location of the region with maximum open area, and the upstream location of the slot were significant. An optimal configuration consisting of a highly peaked waveform, shifted to the pressure side of the passage center, and stationed $-0.71C_{ax}$ upstream of the leading edge was identified using signal-to-noise ratio analysis. Total pressure loss coefficient, C_{Po} , was reduced in the near-wall region relative to a baseline two-dimensional slot for all inlet conditions. Endwall cooling levels were lower than the baseline because of positioning further upstream and a wider average slot width.

Total pressure losses were reduced by two methods. Leakage injection farther upstream from the vane induced early formation of the passage vortex for inlet conditions with a near-wall total pressure deficit. Increased coolant flow through the center of the passage also strengthened endwall crossflow. Both mechanisms shifted the passage vortex laterally across the passage toward the suction surface. This integrated vorticity associated with the passage vortex and from film-cooling jets injecting near the vane shoulder. Combining these circulating flows lowered total pressure losses through the passage.

5.4 Recommendations for Further Investigation

Design of experiments techniques were shown to be very powerful in decoupling effects of the various parameters. A partial factorial design was employed to reduce the number of trial configurations. Upstream distance to the slot and

nominal width were determined to be dominant factors in thermal performance while scalloping amplitude had the largest influence on near-wall total pressure losses.

In all cases, factors which were unaccounted for (error variability) had significant effects even contributing the majority of influence on secondary flow losses for an inlet total pressure gradient. Coupling effects were distributed across all parameters in the current study. New trials could be designed to investigate parameter coupling effects while fixing the primary parameters of influence at their optimized values or eliminating the parameters without direct influence.

The scalloping shape was selected as a cosine wave because of its continuous properties and simplicity in manufacturing. Alternative shaping functions, perhaps polynomials, could be evaluated to provide greater control over injection localization.

Finally, the design of experiments approach is useful to evaluate the design space across a wide range. Gradient based search methods could be used once an initial configuration is determined by design of experiments to optimize parameters which do not have a monotonic effect.

Appendix A Performance Evaluation Metrics and Statistics

Table A.1: Performance Metrics for All Trial Configurations

Trial	Phase	Amp	Width(W)	Distance	Case #1		Case #2		Case #3	
					$\bar{\eta}$	C_{Po}	$\bar{\eta}$	C_{Po}	$\bar{\eta}$	C_{Po}
1	0	0.1W	1.0Nom	$-0.42C_{ax}$	0.273	3.267	0.401	3.300	0.335	3.355
2	0	0.5W	0.5Nom	$-0.71C_{ax}$	0.209	2.932	0.340	3.109	0.324	2.980
3	0	0.9W	1.5Nom	$-1.00C_{ax}$	0.188	2.821	0.290	3.136	0.218	2.919
4	60	0.1W	1.0Nom	$-0.71C_{ax}$	0.211	3.018	0.343	3.205	0.261	3.072
5	60	0.5W	0.5Nom	$-1.00C_{ax}$	0.197	2.890	0.311	3.059	0.261	2.875
6	60	0.9W	1.5Nom	$-0.42C_{ax}$	0.247	2.981	0.324	3.111	0.280	3.069
7	120	0.1W	0.5Nom	$-0.42C_{ax}$	0.273	3.112	0.417	3.209	0.414	3.154
8	120	0.5W	1.5Nom	$-0.71C_{ax}$	0.211	3.020	0.326	3.126	0.248	3.019
9	120	0.9W	1.0Nom	$-1.00C_{ax}$	0.197	3.050	0.302	2.915	0.241	2.830
10	180	0.1W	1.5Nom	$-1.00C_{ax}$	0.197	2.995	0.319	3.272	0.235	3.085
11	180	0.5W	1.0Nom	$-0.42C_{ax}$	0.244	3.079	0.380	3.174	0.315	3.162
12	180	0.9W	0.5Nom	$-0.71C_{ax}$	0.224	2.838	0.366	3.074	0.311	3.020
13	240	0.1W	0.5Nom	$-1.00C_{ax}$	0.202	3.153	0.331	3.243	0.282	3.216
14	240	0.5W	1.5Nom	$-0.42C_{ax}$	0.235	2.850	0.362	3.127	0.302	2.863
15	240	0.9W	1.0Nom	$-0.71C_{ax}$	0.204	2.824	0.329	3.064	0.248	2.733
16	300	0.1W	1.5Nom	$-0.71C_{ax}$	0.212	2.966	0.338	3.262	0.247	2.997
17	300	0.5W	1.0Nom	$-1.00C_{ax}$	0.195	2.810	0.319	3.146	0.241	2.871
18	300	0.9W	0.5Nom	$-0.42C_{ax}$	0.257	2.944	0.407	3.040	0.427	2.995
base	0	0.0W	1.0Nom	$-0.42C_{ax}$	0.273	3.039	0.398	3.230	0.329	3.225

Table A.2: Parameter Level Average Performance Metrics

	Level	Case #1		Case #2		Case #3	
		$\bar{\eta}$	C_{Po}	$\bar{\eta}$	C_{Po}	$\bar{\eta}$	C_{Po}
Phase	0	0.223	3.007	0.344	3.182	0.292	3.085
	60	0.218	2.963	0.326	3.125	0.267	3.006
	120	0.227	3.060	0.348	3.083	0.301	3.001
	180	0.222	2.971	0.355	3.173	0.287	3.089
	240	0.214	2.943	0.341	3.145	0.277	2.937
	300	0.221	2.907	0.355	3.149	0.305	2.955
Amp	0.1W	0.228	3.085	0.358	3.248	0.296	3.147
	0.5W	0.215	2.930	0.340	3.124	0.282	2.962
	0.9W	0.220	2.910	0.336	3.057	0.287	2.928
Width	0.5Nom	0.227	2.978	0.362	3.122	0.337	3.040
	1.0Nom	0.221	3.008	0.346	3.134	0.273	3.004
	1.5Nom	0.215	2.939	0.327	3.172	0.255	2.992
Dist	$-0.42C_{ax}$	0.255	3.039	0.382	3.160	0.345	3.100
	$-0.71C_{ax}$	0.212	2.933	0.340	3.140	0.273	2.970
	$-1.00C_{ax}$	0.196	2.953	0.312	3.128	0.246	2.966

Table A.3: Thermal ANOVA - Case #1

Factor	DOF	TSS	MSS	F-Ratio	α
Phase	5	0.654	0.131	1.226	0.400
Amplitude	2	1.106	0.553	5.180	0.049
Width(W)	2	0.888	0.444	4.159	0.074
Distance	2	22.59	11.29	105.8	0.000
Error	6	0.640	0.107		
Total	17	25.88			

Table A.4: Aerodynamic ANOVA - Case #1

Factor	DOF	TSS	MSS	F-Ratio	α
Phase	5	16.63	3.326	0.740	0.621
Amplitude	2	43.14	21.57	4.802	0.057
Width(W)	2	5.631	2.815	0.627	0.566
Distance	2	14.75	7.374	1.641	0.270
Error	6	26.96	4.493		
Total	17	107.1			

Table A.5: Thermal ANOVA - Case #2

Factor	DOF	TSS	MSS	F-Ratio	α
Phase	5	3.642	0.728	2.680	0.131
Amplitude	2	3.375	1.687	6.209	0.035
Width(W)	2	7.575	3.788	13.94	0.006
Distance	2	29.89	14.94	54.99	0.000
Error	6	1.631	0.272		
Total	17	46.11			

Table A.6: Aerodynamic ANOVA - Case #2

Factor	DOF	TSS	MSS	F-Ratio	α
Phase	5	7.747	1.549	1.622	0.285
Amplitude	2	46.62	23.31	24.40	0.001
Width(W)	2	3.404	1.702	1.781	0.247
Distance	2	1.282	0.641	0.671	0.546
Error	6	5.733	0.955		
Total	17	64.78			

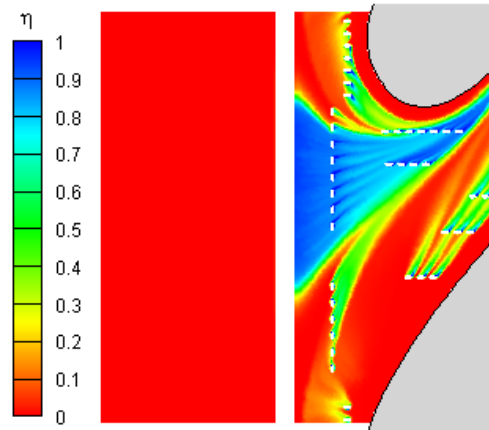
Table A.7: Thermal ANOVA - Case #3

Factor	DOF	TSS	MSS	F-Ratio	α
Phase	5	6.153	1.231	2.275	0.173
Amplitude	2	1.157	0.578	1.069	0.401
Width(W)	2	44.52	22.26	41.15	0.000
Distance	2	63.80	31.90	58.98	0.000
Error	6	3.245	0.541		
Total	17	118.9			

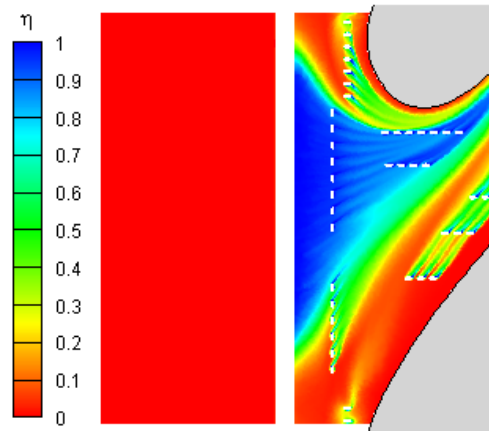
Table A.8: Aerodynamic ANOVA - Case #3

Factor	DOF	TSS	MSS	F-Ratio	α
Phase	5	29.90	5.979	0.793	0.591
Amplitude	2	81.97	40.98	5.436	0.045
Width(W)	2	3.685	1.843	0.244	0.791
Distance	2	34.05	17.02	2.258	0.186
Error	6	45.24	7.540		
Total	17	194.8			

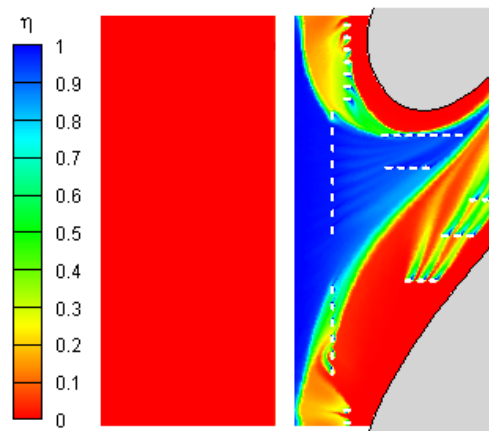
Appendix B Endwall Adiabatic Effectiveness Contours



(a) Case #1

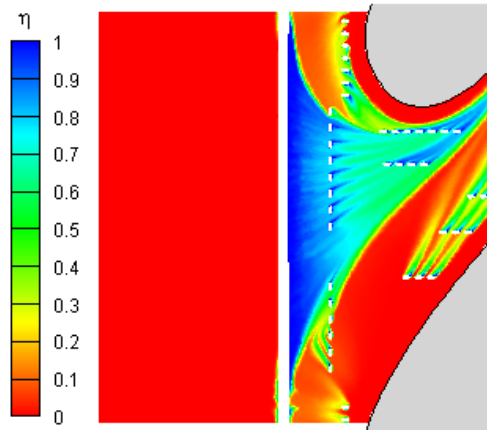


(b) Case #2

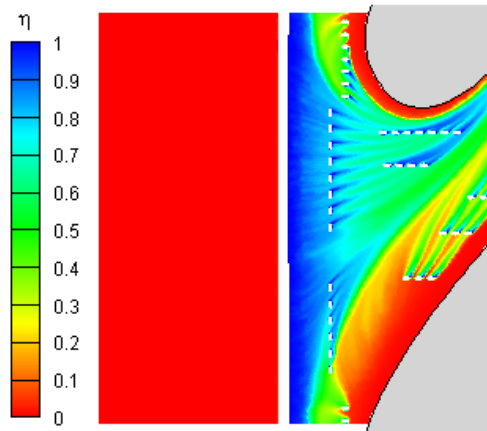


(c) Case #3

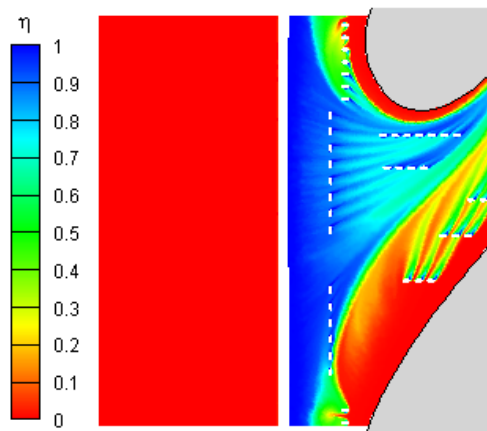
Figure B.1: Contours of endwall adiabatic effectiveness for baseline configuration: Phase = 0° , Amp = 0.0W, Width = 1.0Nom, Dist = $-0.42C_{ax}$



(a) Case #1

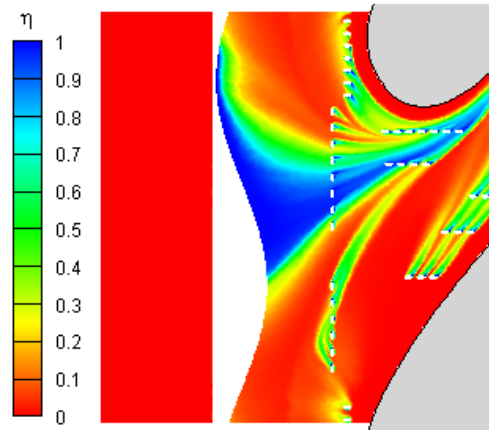


(b) Case #2

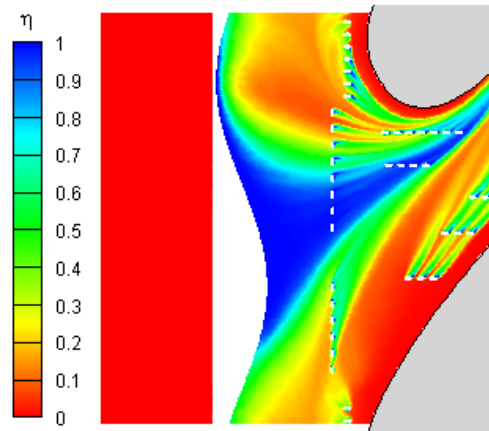


(c) Case #3

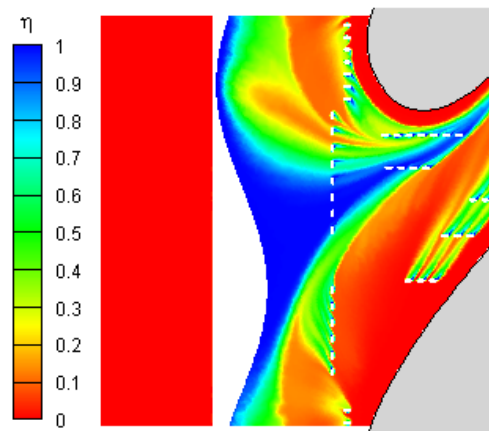
Figure B.2: Contours of endwall adiabatic effectiveness for optimal thermal configuration: Phase = 300° , Amp = $0.1W$, Width = $0.5Nom$, Dist = $-0.42C_{ax}$



(a) Case #1

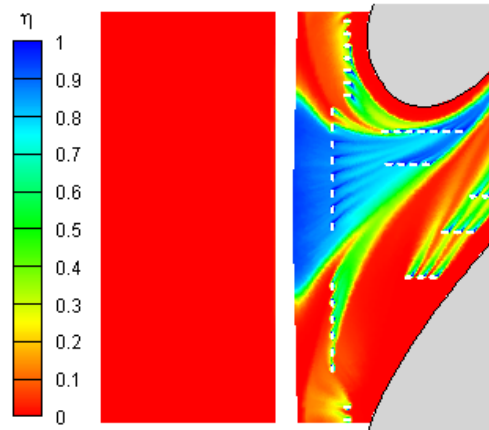


(b) Case #2

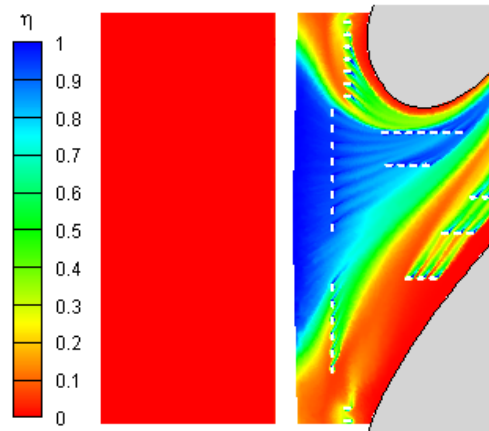


(c) Case #3

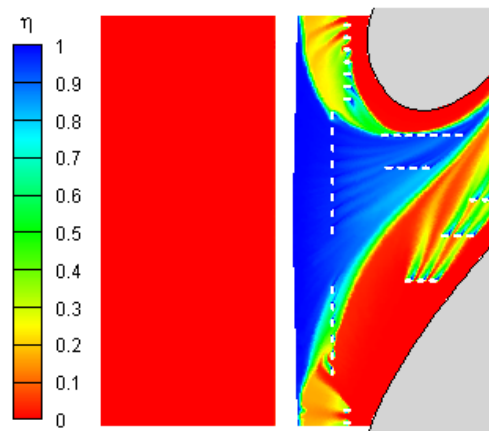
Figure B.3: Contours of endwall adiabatic effectiveness for optimal aerodynamic configuration: Phase = 240° , Amp = $0.9W$, Width = 1.5Nom , Dist = $-0.71C_{ax}$



(a) Case #1

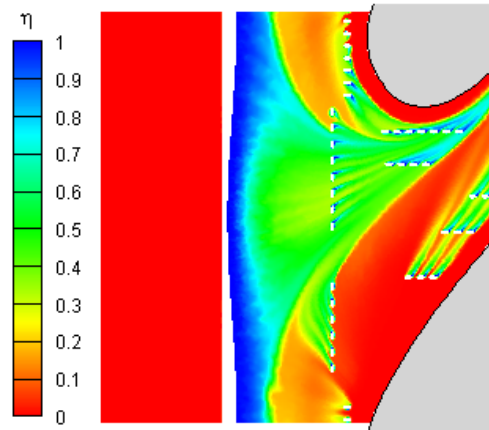


(b) Case #2

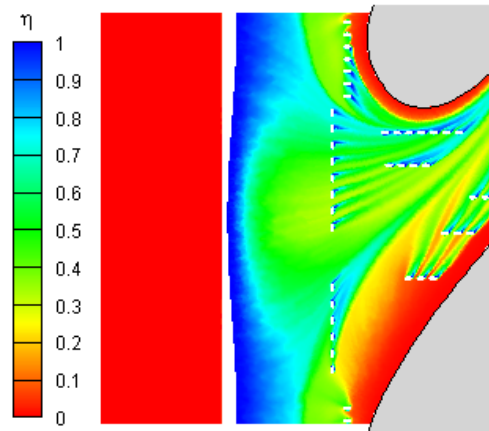


(c) Case #3

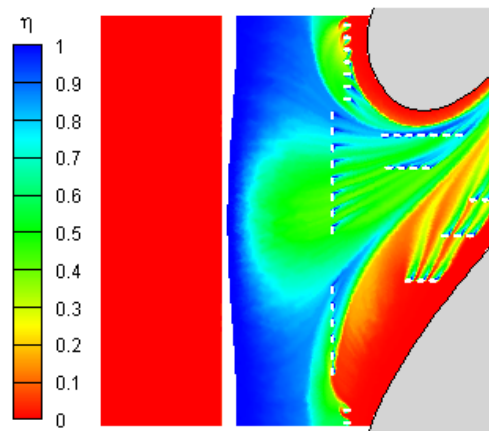
Figure B.4: Contours of endwall adiabatic effectiveness for trial 1 configuration: Phase = 0° , Amp = $0.1W$, Width = $1.0Nom$, Dist = $-0.42C_{ax}$



(a) Case #1

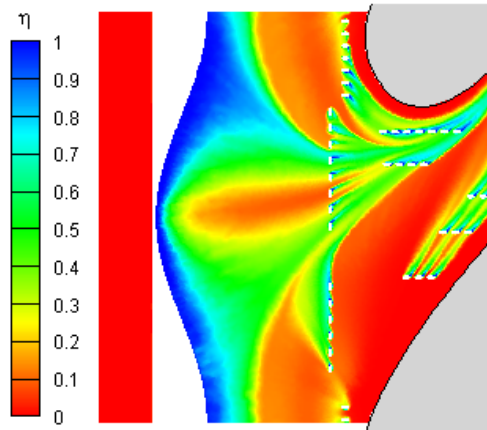


(b) Case #2

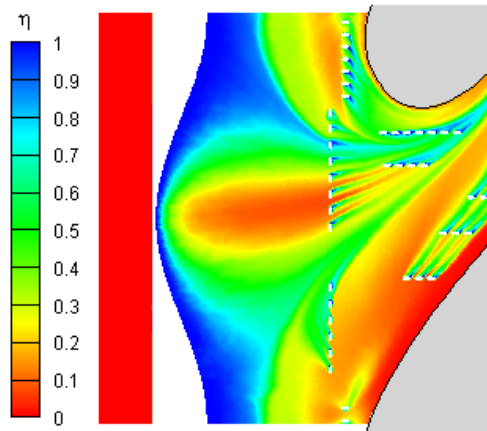


(c) Case #3

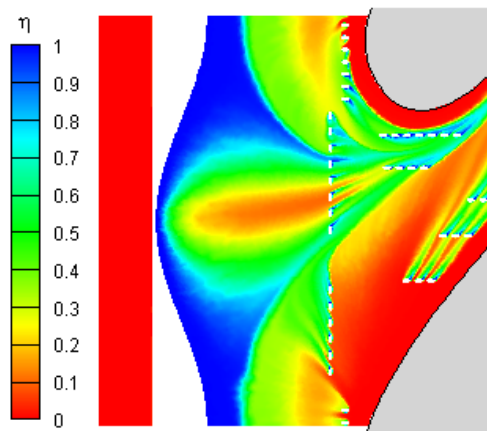
Figure B.5: Contours of endwall adiabatic effectiveness for trial 2 configuration: Phase = 0° , Amp = $0.5W$, Width = $0.5Nom$, Dist = $-0.71C_{ax}$



(a) Case #1

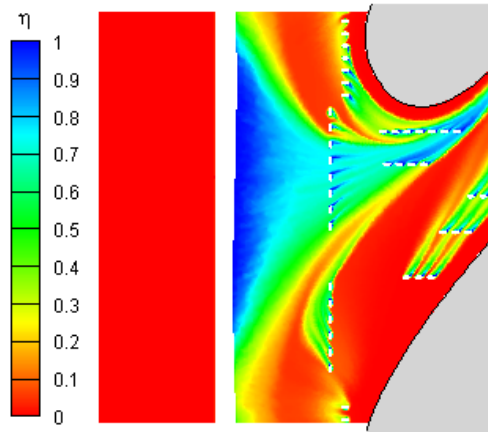


(b) Case #2

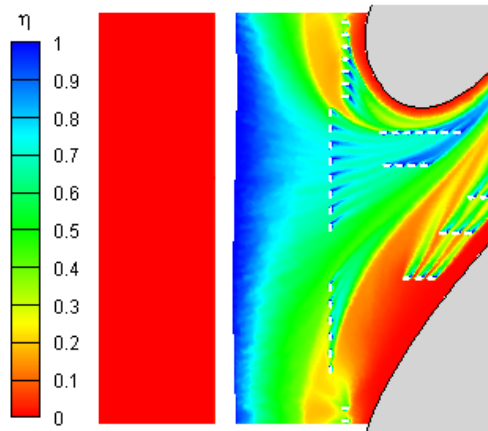


(c) Case #3

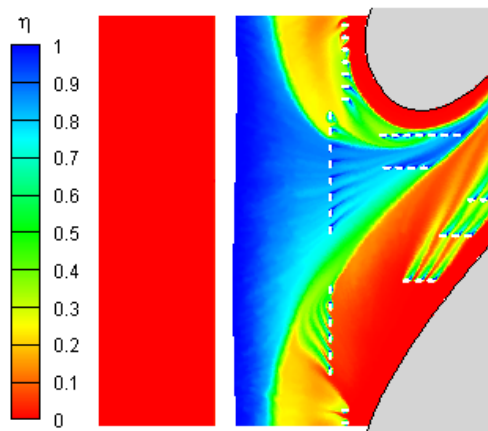
Figure B.6: Contours of endwall adiabatic effectiveness for trial 3 configuration: Phase = 0° , Amp = 0.9W, Width = 1.5Nom, Dist = $-1.0C_{ax}$



(a) Case #1

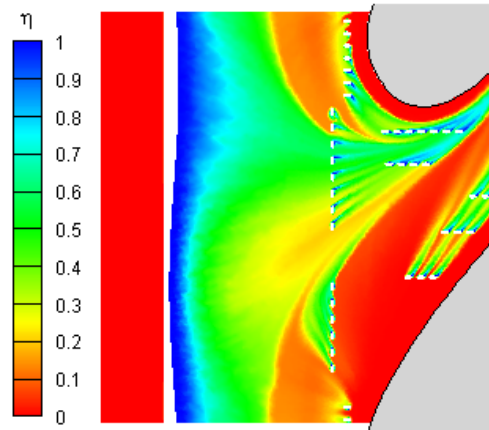


(b) Case #2

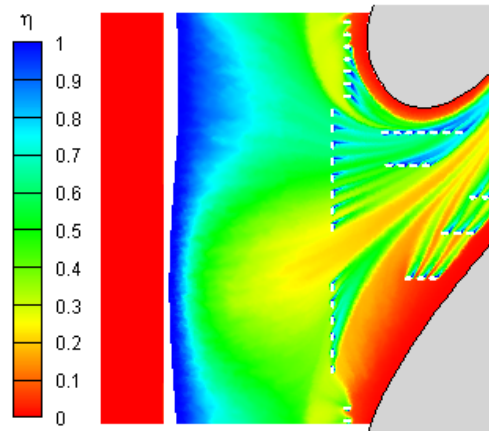


(c) Case #3

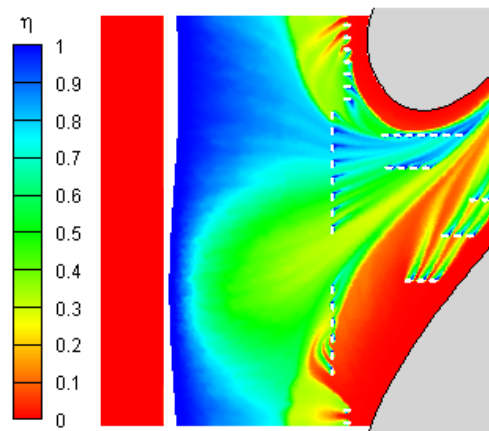
Figure B.7: Contours of endwall adiabatic effectiveness for trial 4 configuration: Phase = 60° , Amp = $0.1W$, Width = $1.0Nom$, Dist = $-0.71C_{ax}$



(a) Case #1

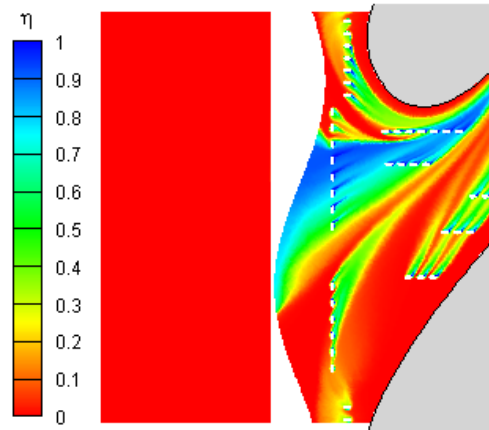


(b) Case #2

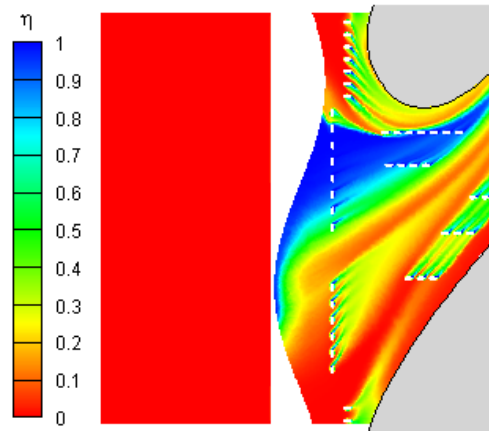


(c) Case #3

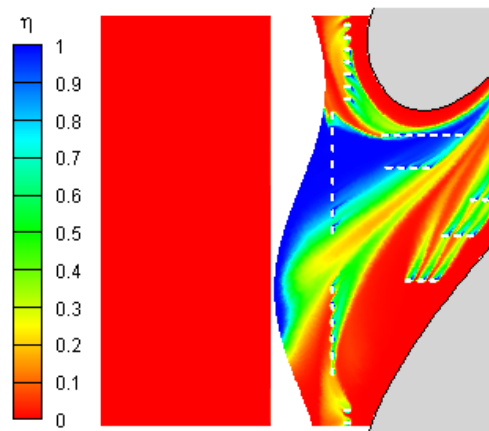
Figure B.8: Contours of endwall adiabatic effectiveness for trial 5 configuration: Phase = 60° , Amp = $0.5W$, Width = $0.5Nom$, Dist = $-1.0C_{ax}$



(a) Case #1

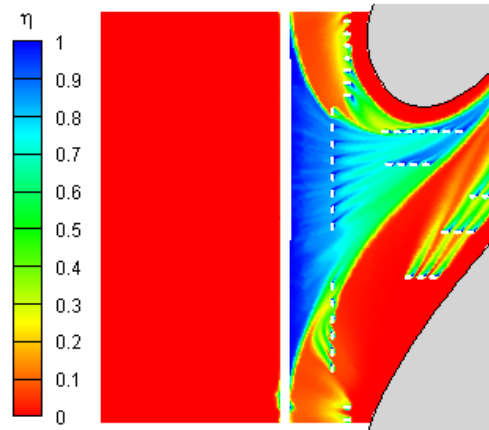


(b) Case #2

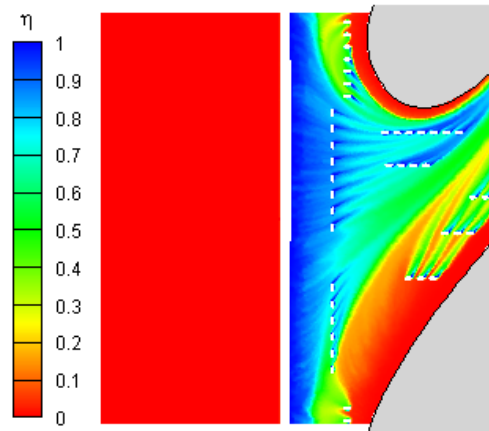


(c) Case #3

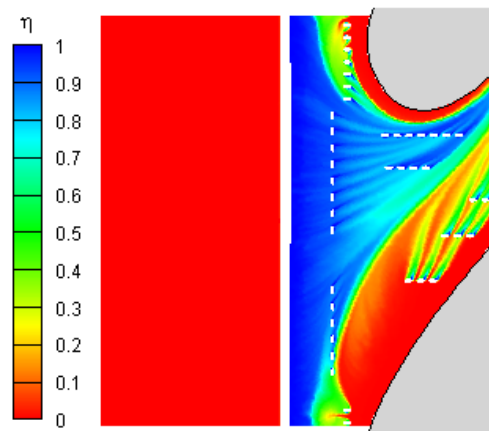
Figure B.9: Contours of endwall adiabatic effectiveness for trial 6 configuration: Phase = 60° , Amp = $0.9W$, Width = $1.5N_{om}$, Dist = $-0.42C_{ax}$



(a) Case #1

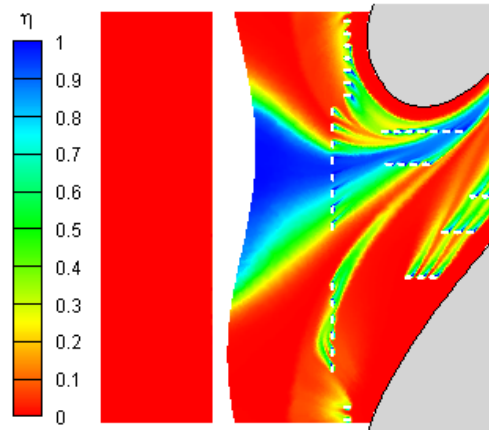


(b) Case #2

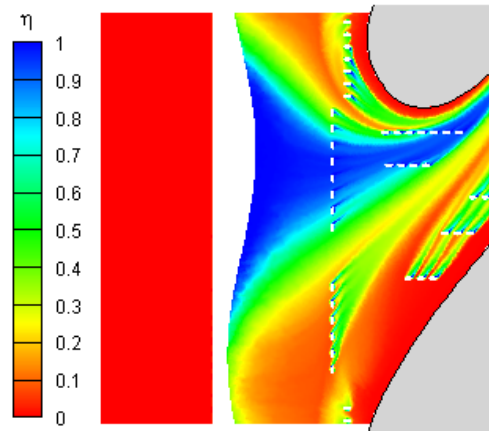


(c) Case #3

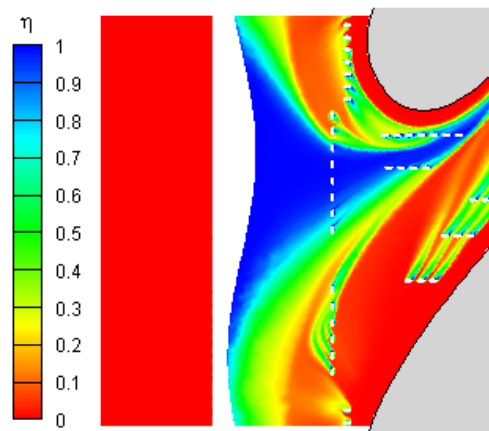
Figure B.10: Contours of endwall adiabatic effectiveness for trial 7 configuration:
Phase = 120° , Amp = $0.1W$, Width = 0.5Nom , Dist = $-0.42C_{ax}$



(a) Case #1

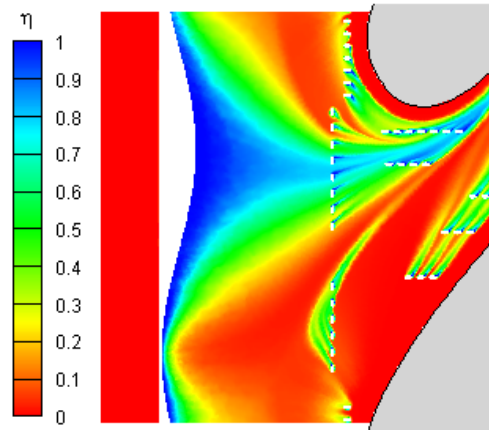


(b) Case #2

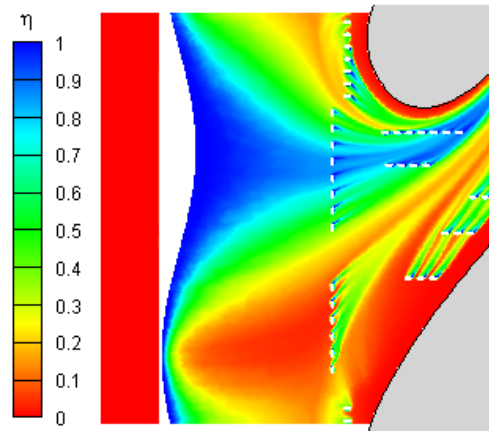


(c) Case #3

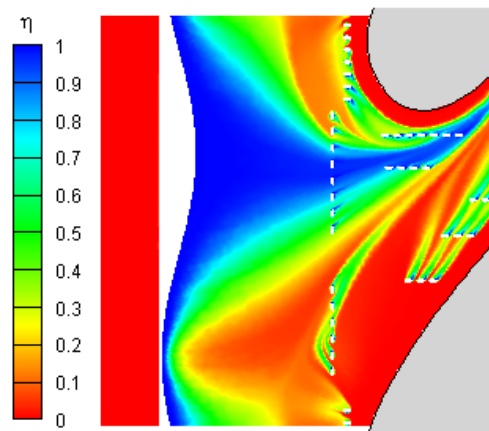
Figure B.11: Contours of endwall adiabatic effectiveness for trial 8 configuration:
Phase = 120° , Amp = $0.5W$, Width = 1.5Nom , Dist = $-0.71C_{ax}$



(a) Case #1

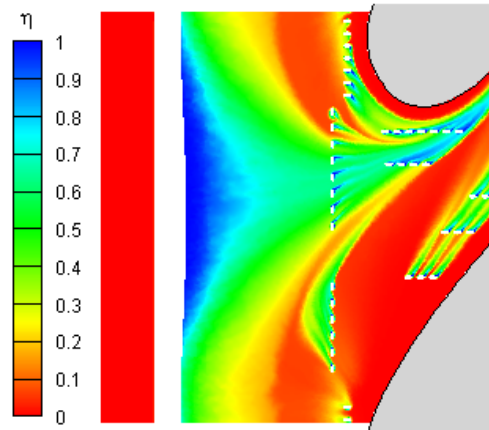


(b) Case #2

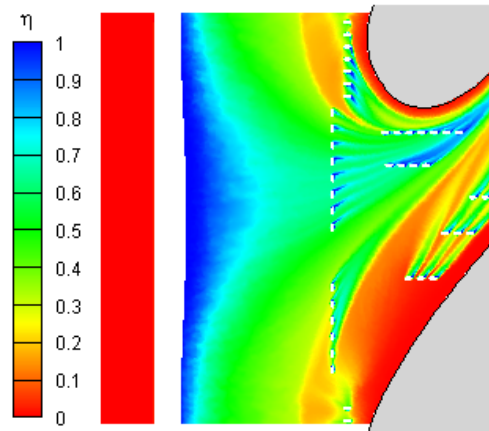


(c) Case #3

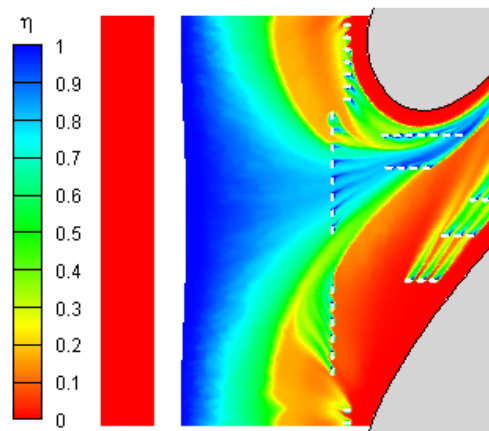
Figure B.12: Contours of endwall adiabatic effectiveness for trial 9 configuration: Phase = 120° , Amp = $0.9W$, Width = 1.0Nom , Dist = $-1.0C_{ax}$



(a) Case #1

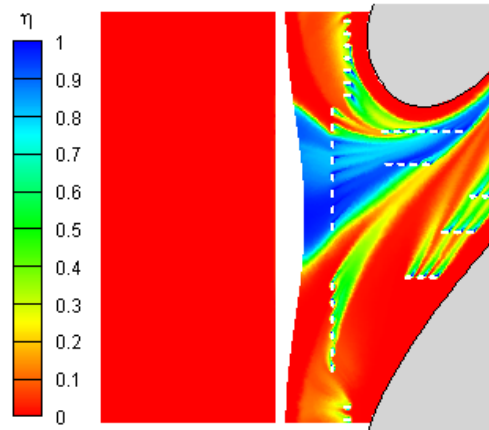


(b) Case #2

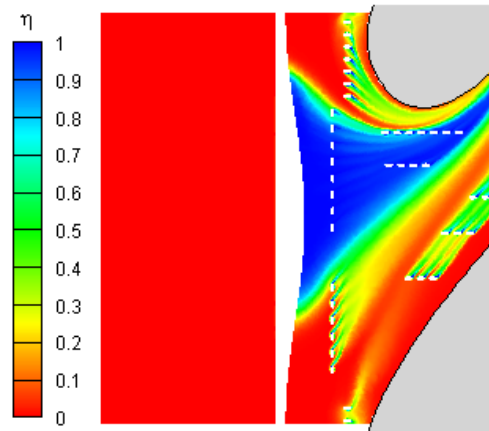


(c) Case #3

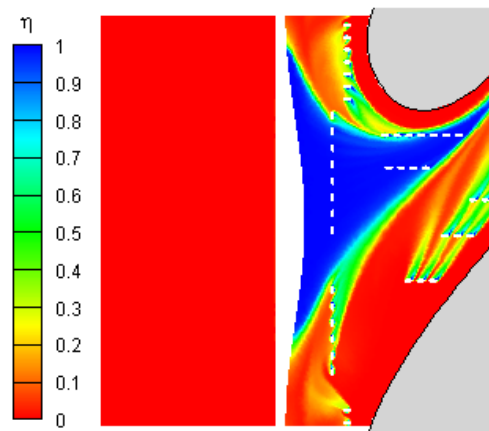
Figure B.13: Contours of endwall adiabatic effectiveness for trial 10 configuration: Phase = 180° , Amp = $0.1W$, Width = 1.5Nom , Dist = $-1.0C_{ax}$



(a) Case #1

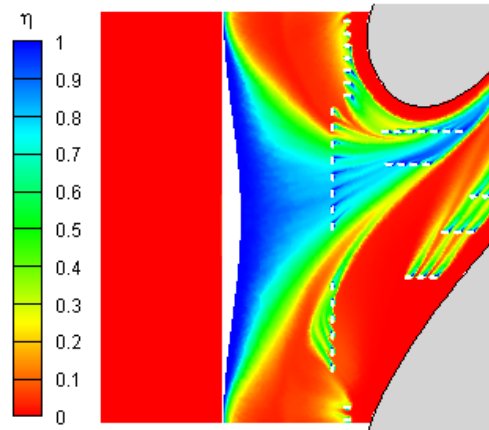


(b) Case #2

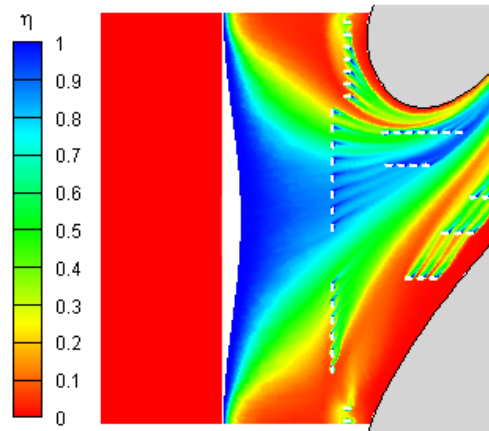


(c) Case #3

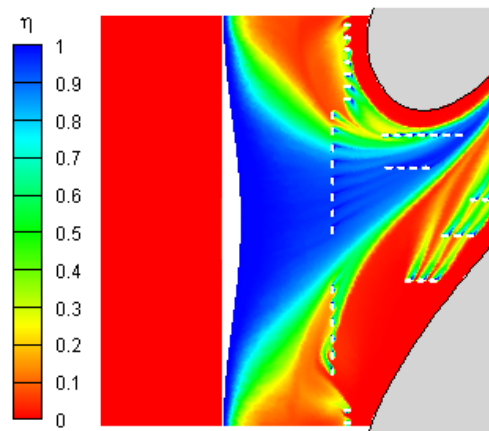
Figure B.14: Contours of endwall adiabatic effectiveness for trial 11 configuration: Phase = 180° , Amp = $0.5W$, Width = $1.0Nom$, Dist = $-0.42C_{ax}$



(a) Case #1

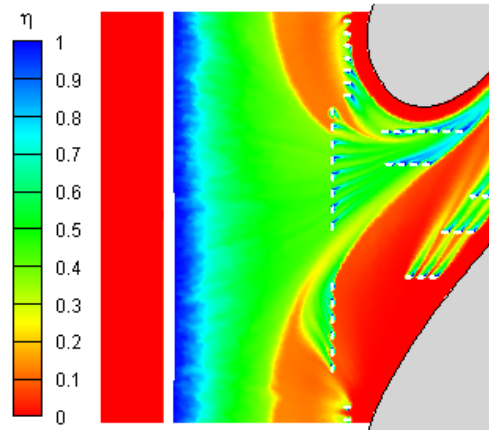


(b) Case #2

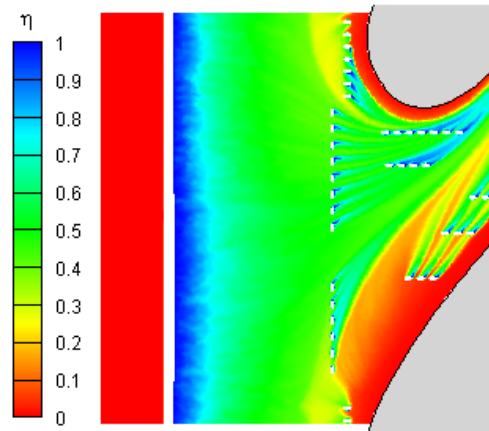


(c) Case #3

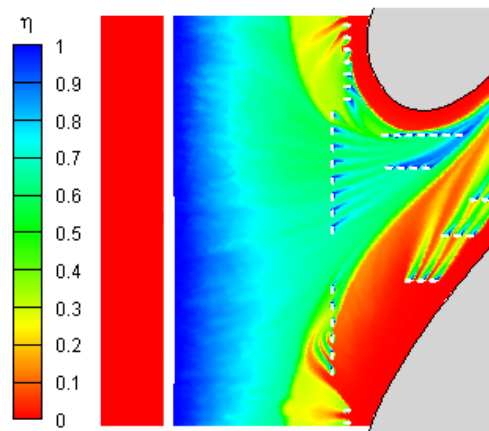
Figure B.15: Contours of endwall adiabatic effectiveness for trial 12 configuration: Phase = 180° , Amp = $0.9W$, Width = $0.5Nom$, Dist = $-0.71C_{ax}$



(a) Case #1

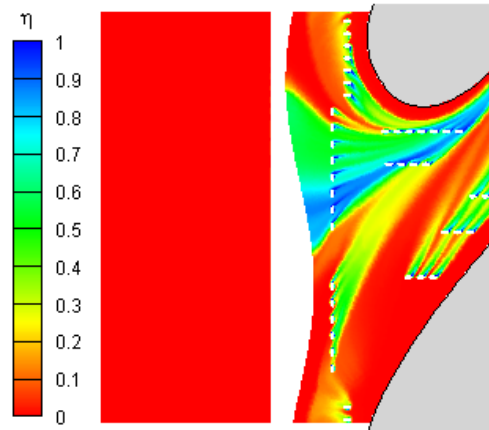


(b) Case #2

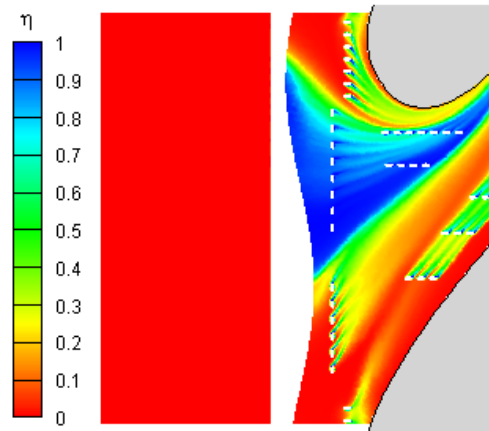


(c) Case #3

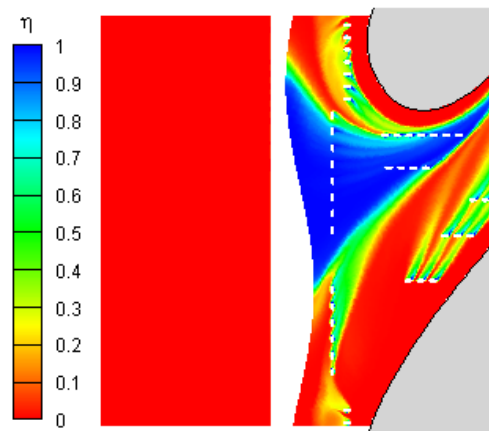
Figure B.16: Contours of endwall adiabatic effectiveness for trial 13 configuration: Phase = 240° , Amp = $0.1W$, Width = $0.5Nom$, Dist = $-1.0C_{ax}$



(a) Case #1

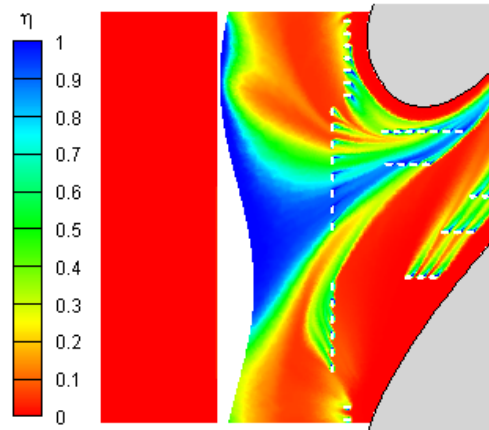


(b) Case #2

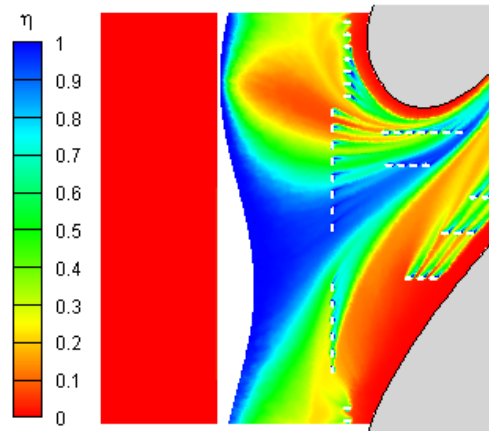


(c) Case #3

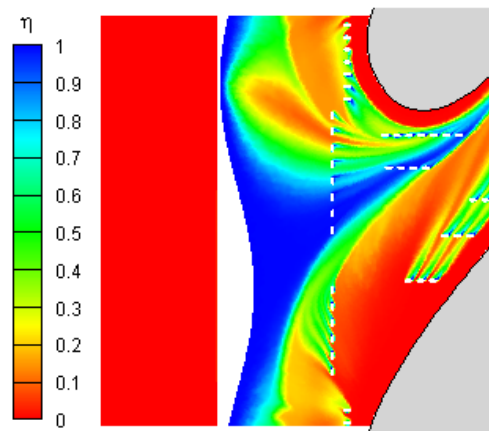
Figure B.17: Contours of endwall adiabatic effectiveness for trial 14 configuration: Phase = 240° , Amp = $0.5W$, Width = 1.5Nom , Dist = $-0.42C_{ax}$



(a) Case #1

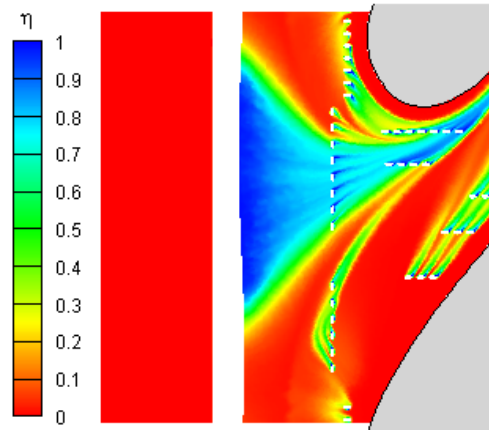


(b) Case #2

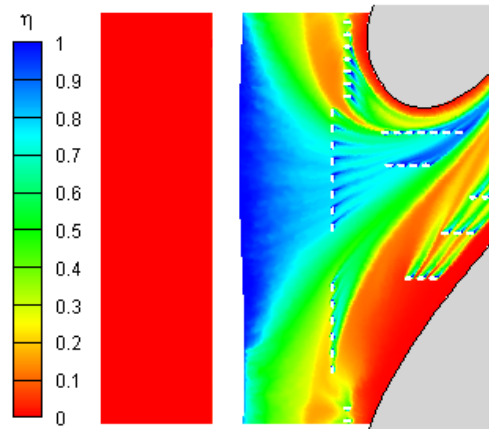


(c) Case #3

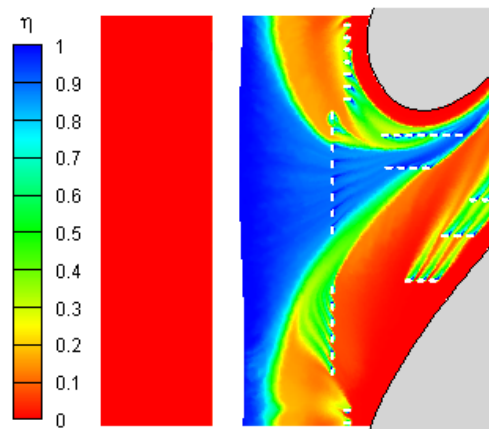
Figure B.18: Contours of endwall adiabatic effectiveness for trial 15 configuration: Phase = 240° , Amp = $0.9W$, Width = $1.0Nom$, Dist = $-0.71C_{ax}$



(a) Case #1

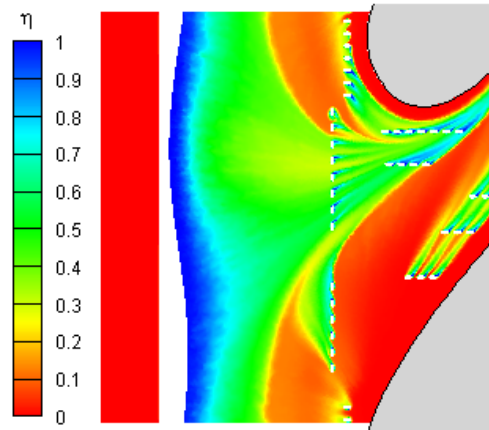


(b) Case #2

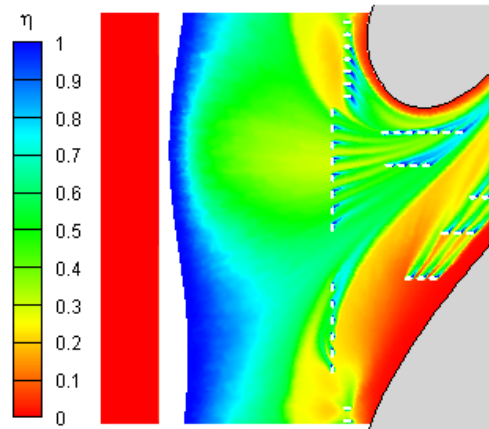


(c) Case #3

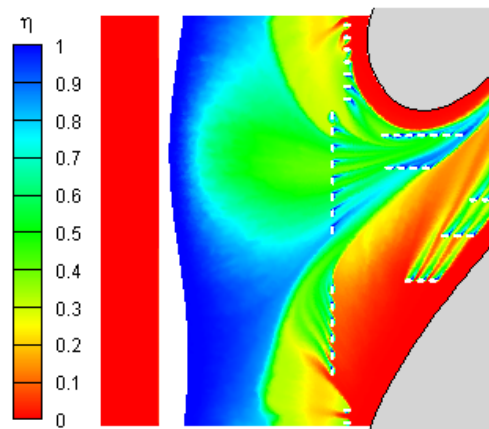
Figure B.19: Contours of endwall adiabatic effectiveness for trial 16 configuration: Phase = 300° , Amp = $0.1W$, Width = 1.5Nom , Dist = $-0.71C_{ax}$



(a) Case #1

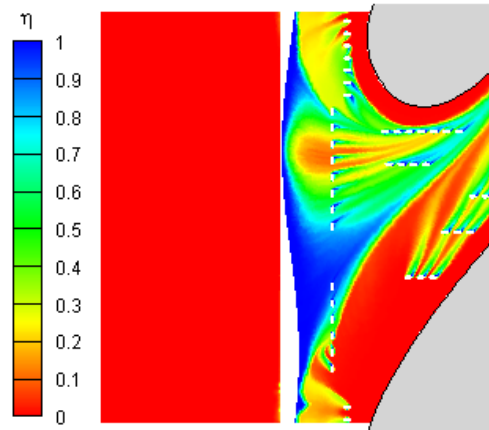


(b) Case #2

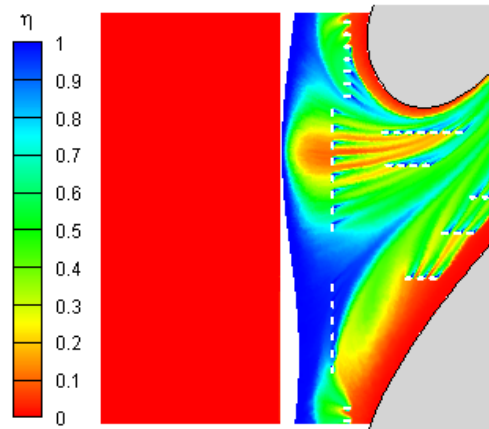


(c) Case #3

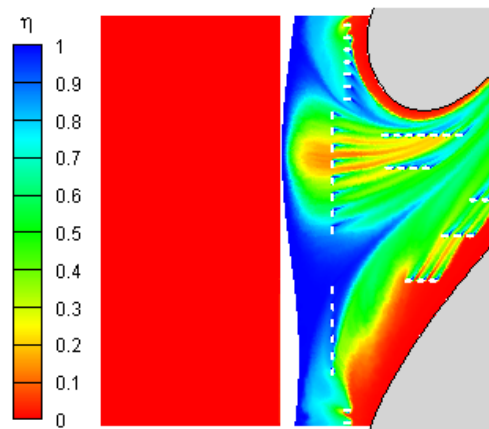
Figure B.20: Contours of endwall adiabatic effectiveness for trial 17 configuration: Phase = 300° , Amp = $0.5W$, Width = $1.0Nom$, Dist = $-1.0C_{ax}$



(a) Case #1



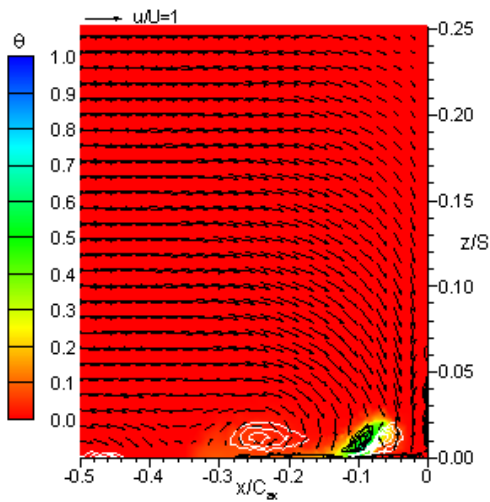
(b) Case #2



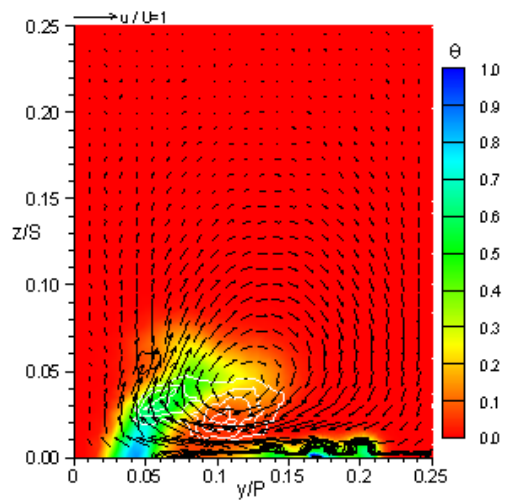
(c) Case #3

Figure B.21: Contours of endwall adiabatic effectiveness for trial 18 configuration: Phase = 300° , Amp = $0.9W$, Width = $0.5Nom$, Dist = $-0.42C_{ax}$

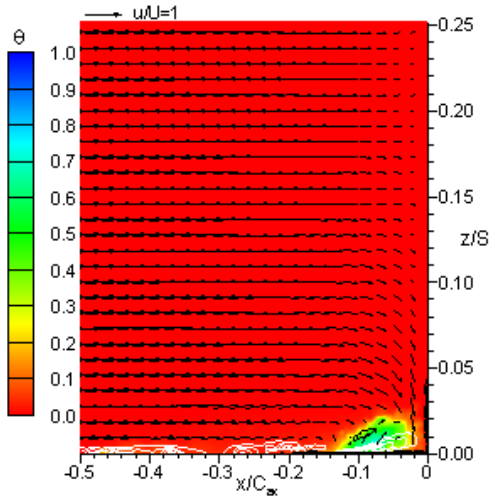
Appendix C Endwall Adiabatic Effectiveness Contours



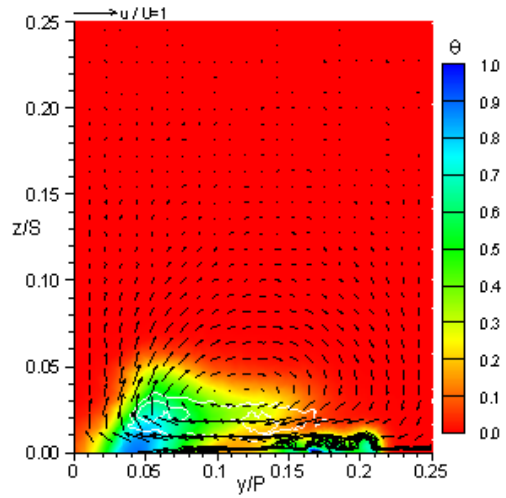
(a) Case #1



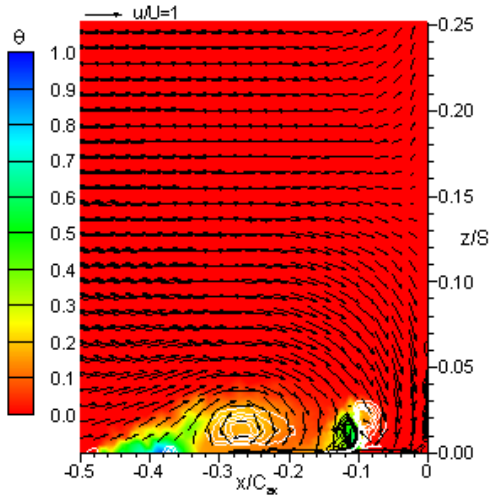
(a) Case #1



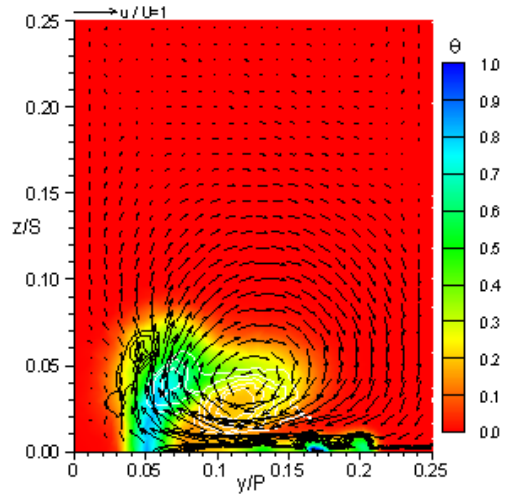
(b) Case #2



(b) Case #2



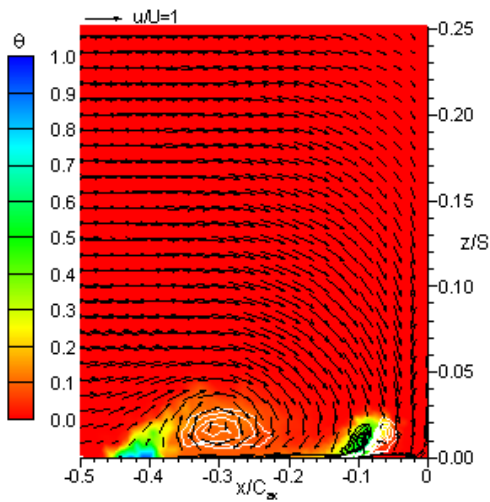
(c) Case #3



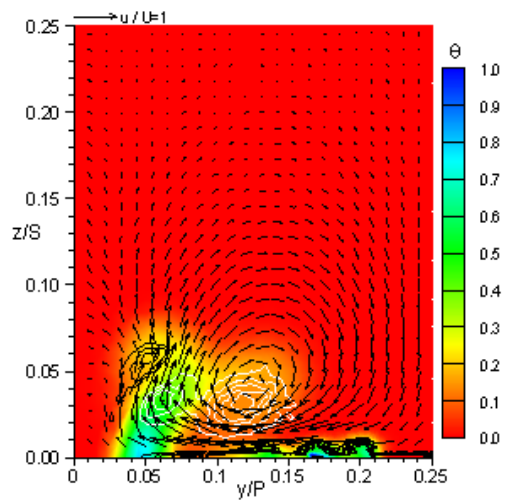
(c) Case #3

Figure C.1: Baseline configuration stagnation plane.

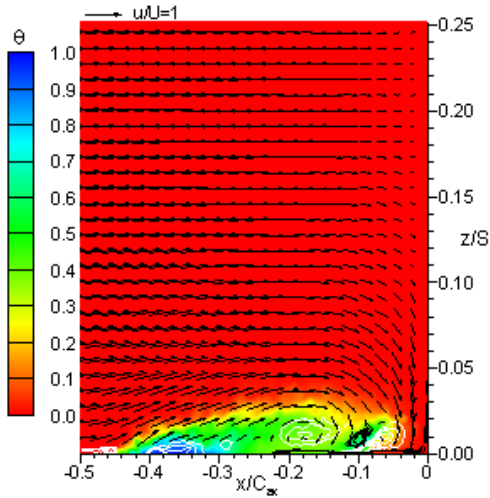
Figure C.2: Baseline configuration SS2 plane.



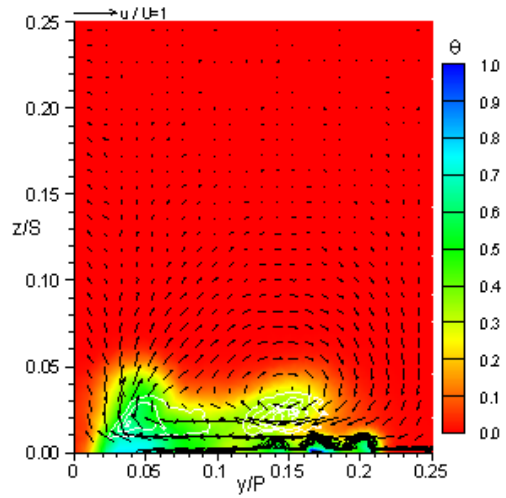
(a) Case #1



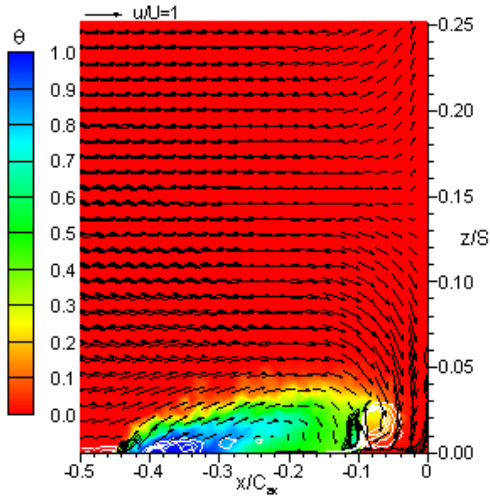
(a) Case #1



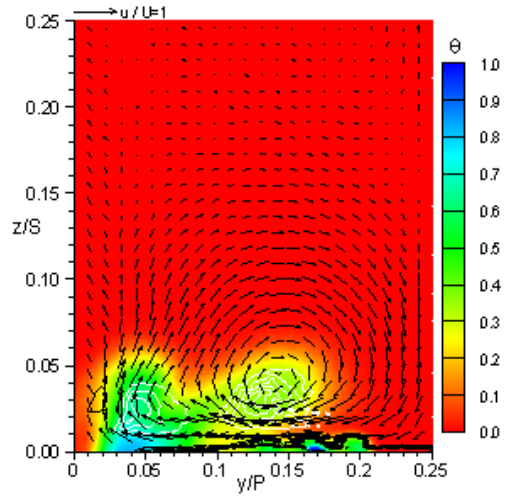
(b) Case #2



(b) Case #2



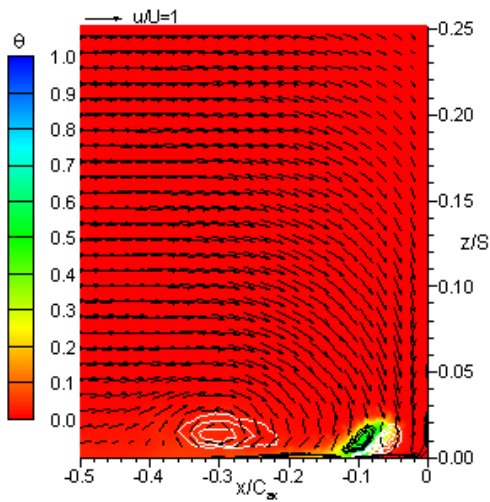
(c) Case #3



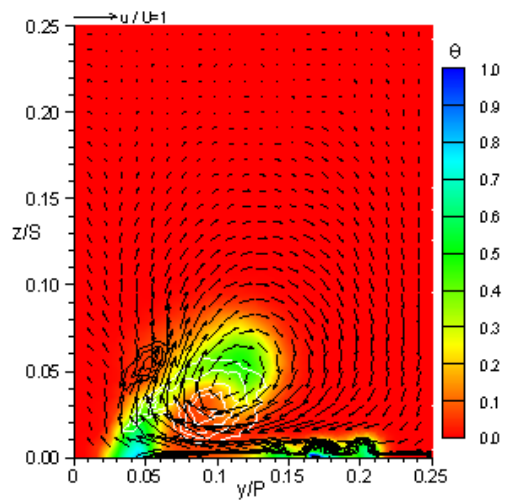
(c) Case #3

Figure C.3: Optimal thermal configuration stagnation plane.

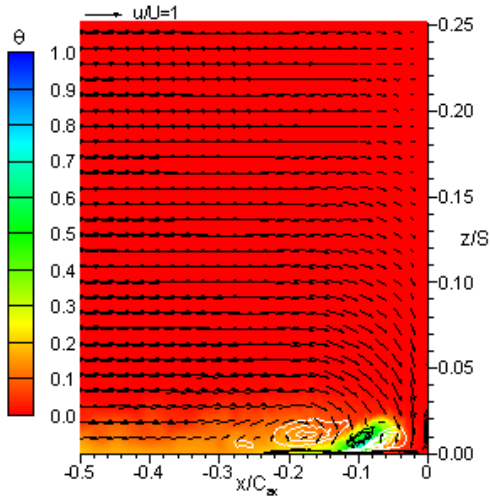
Figure C.4: Optimal thermal configuration SS2 plane.



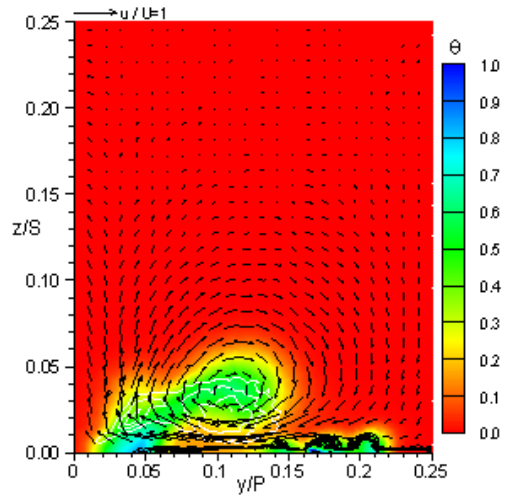
(a) Case #1



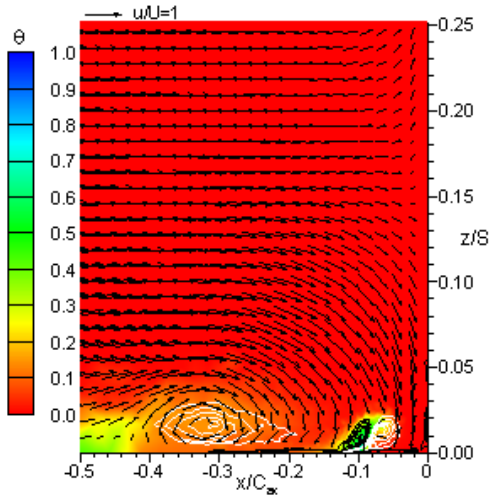
(a) Case #1



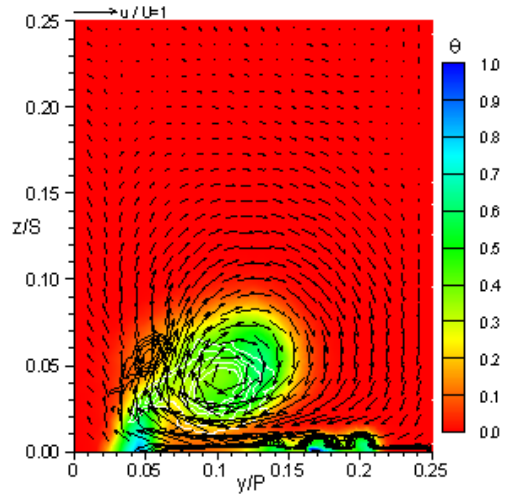
(b) Case #2



(b) Case #2



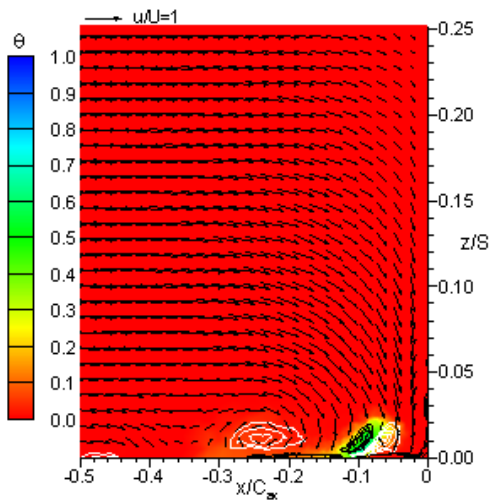
(c) Case #3



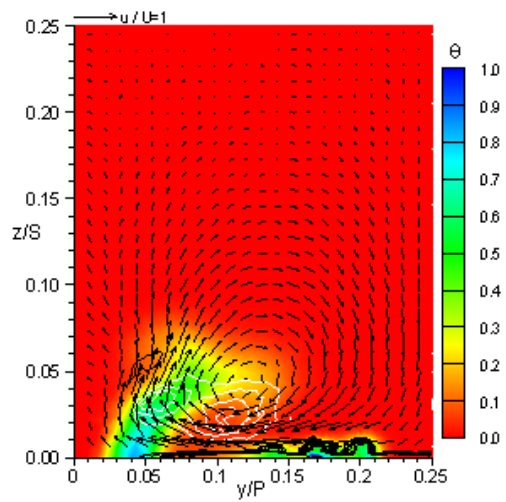
(c) Case #3

Figure C.5: Optimal aerodynamic configuration stagnation plane.

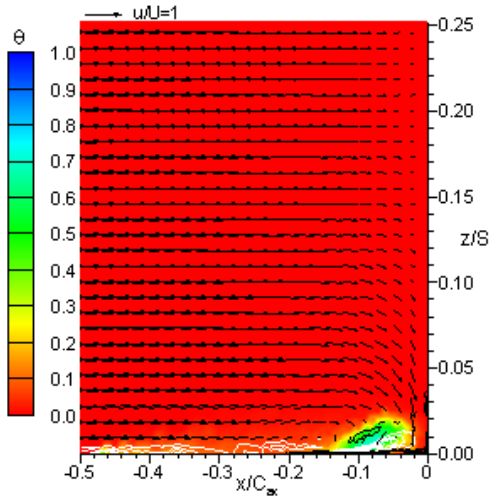
Figure C.6: Optimal aerodynamic configuration SS2 plane.



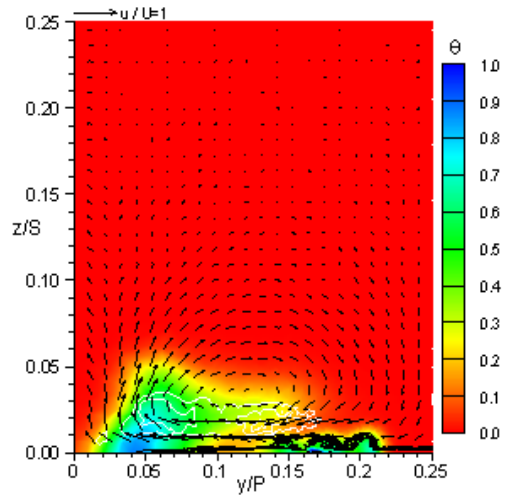
(a) Case #1



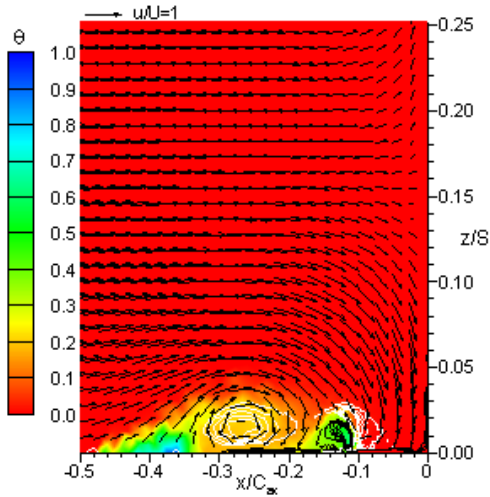
(a) Case #1



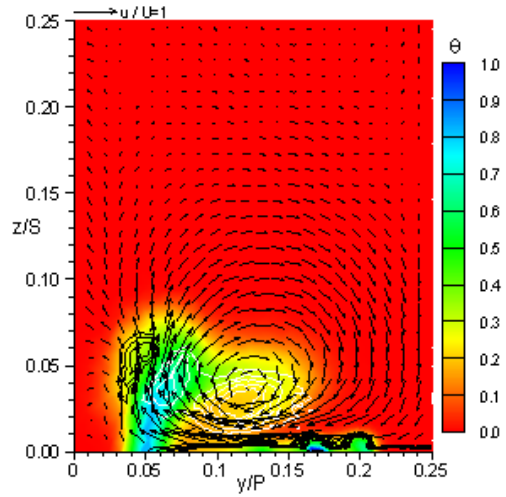
(b) Case #2



(b) Case #2



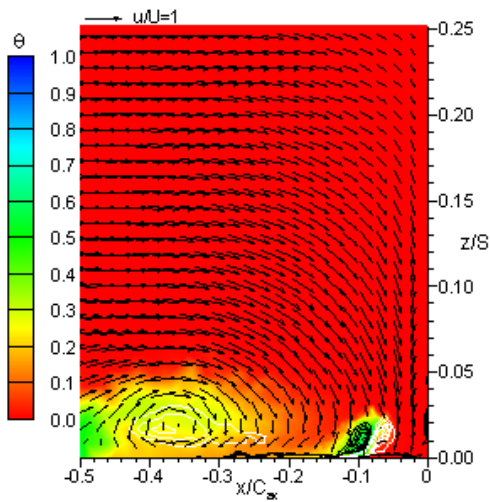
(c) Case #3



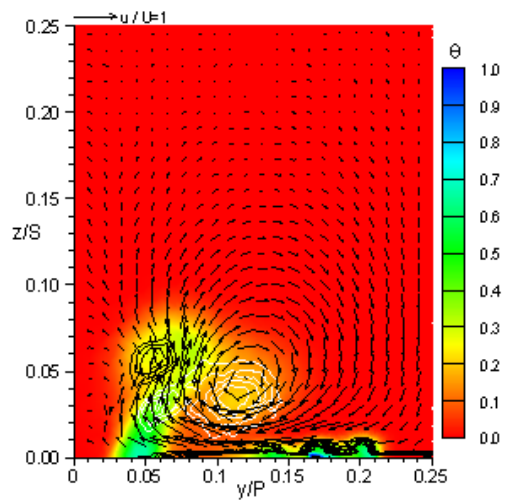
(c) Case #3

Figure C.7: Trial 1 configuration stagnation plane.

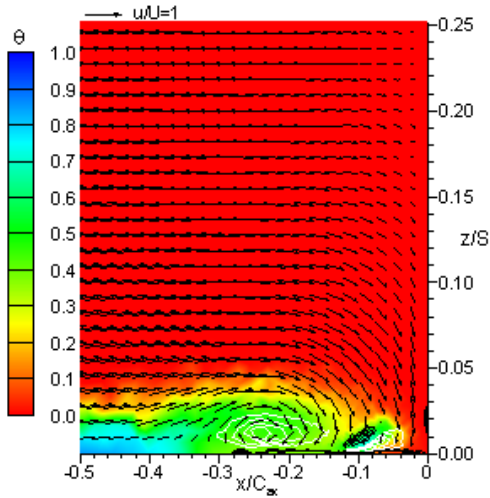
Figure C.8: Trial 1 configuration SS2 plane.



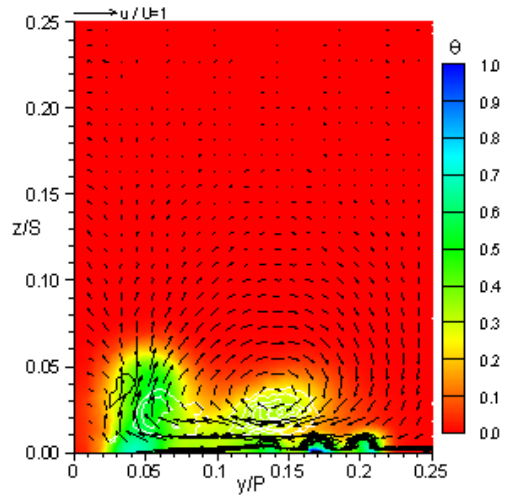
(a) Case #1



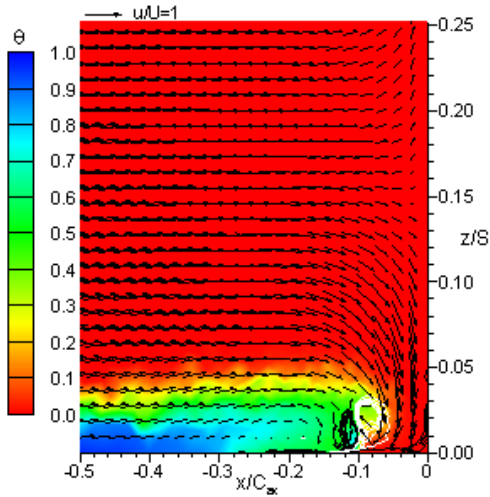
(a) Case #1



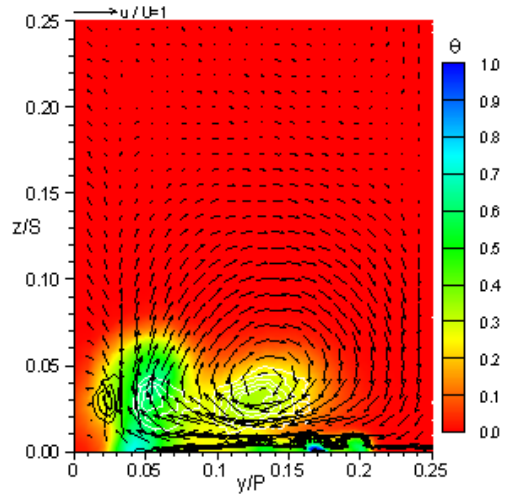
(b) Case #2



(b) Case #2



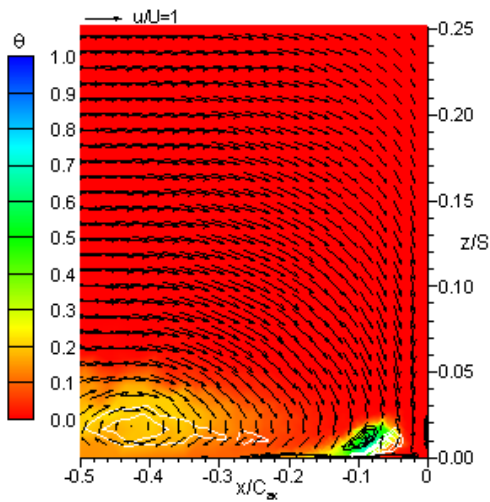
(c) Case #3



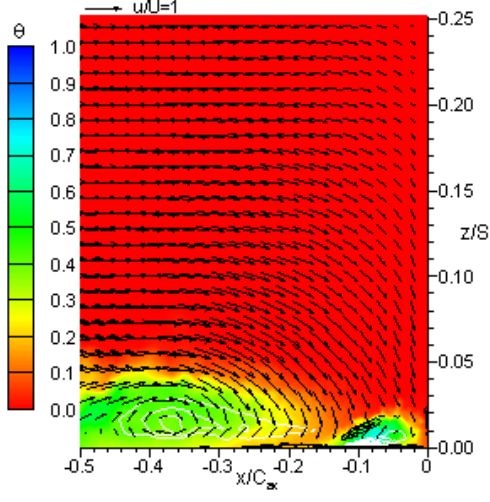
(c) Case #3

Figure C.9: Trial 2 configuration stagnation plane.

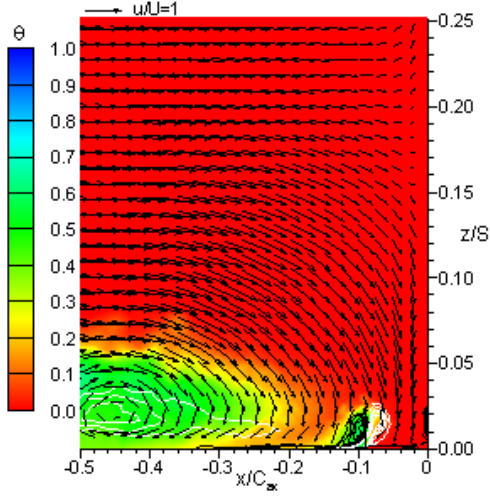
Figure C.10: Trial 2 configuration SS2 plane.



(a) Case #1

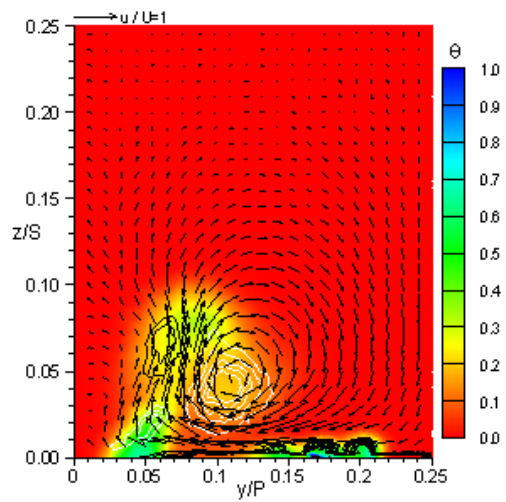


(b) Case #2

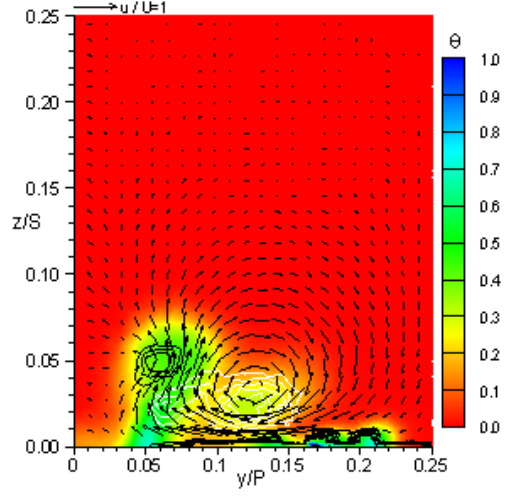


(c) Case #3

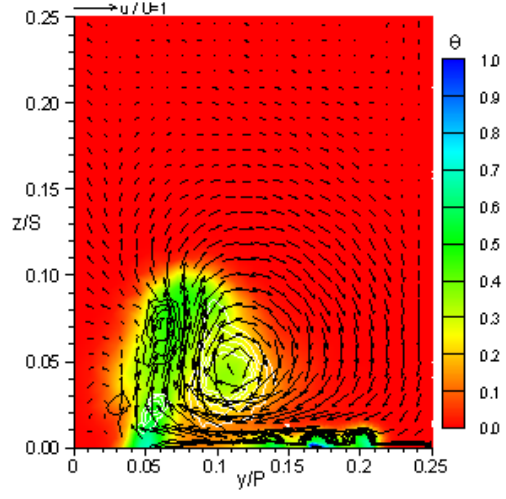
Figure C.11: Trial 3 configuration stagnation plane.



(a) Case #1

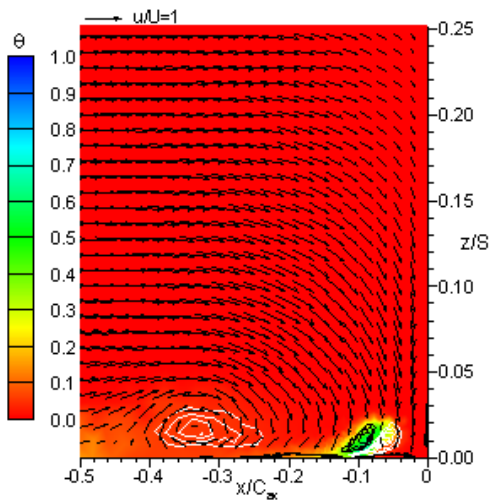


(b) Case #2

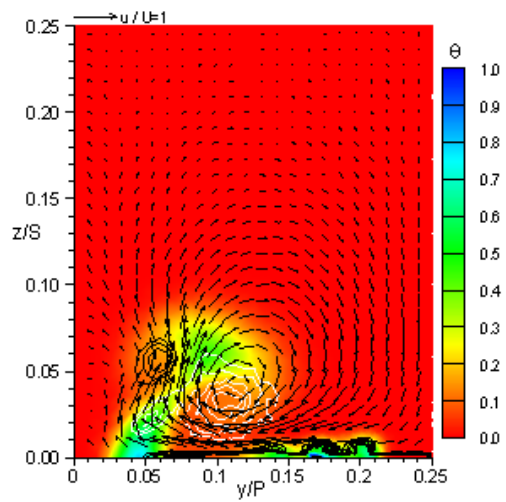


(c) Case #3

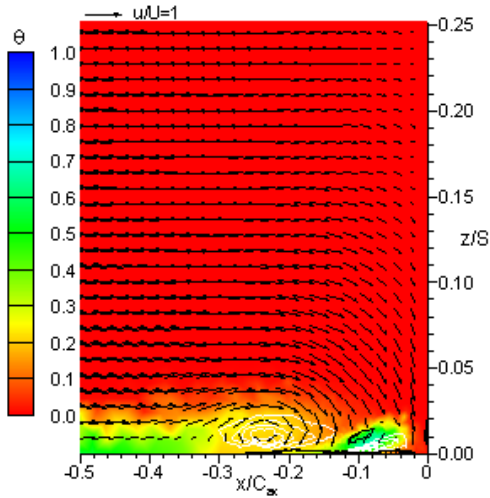
Figure C.12: Trial 3 configuration SS2 plane.



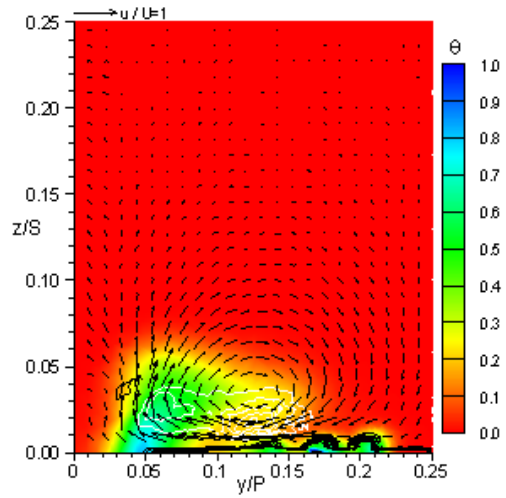
(a) Case #1



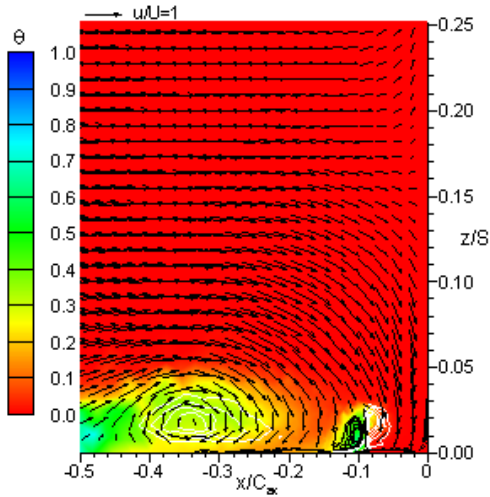
(a) Case #1



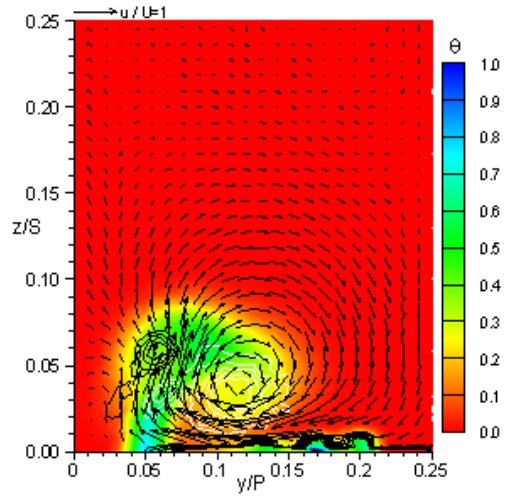
(b) Case #2



(b) Case #2



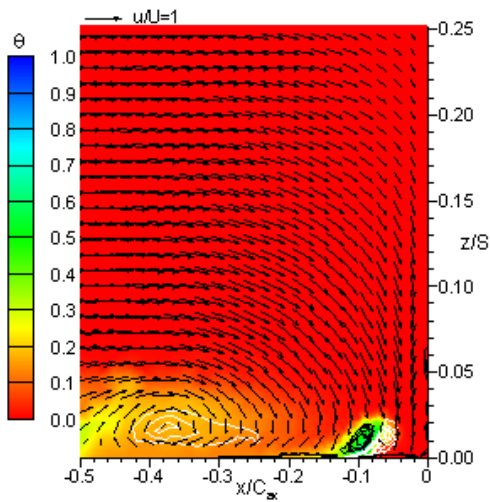
(c) Case #3



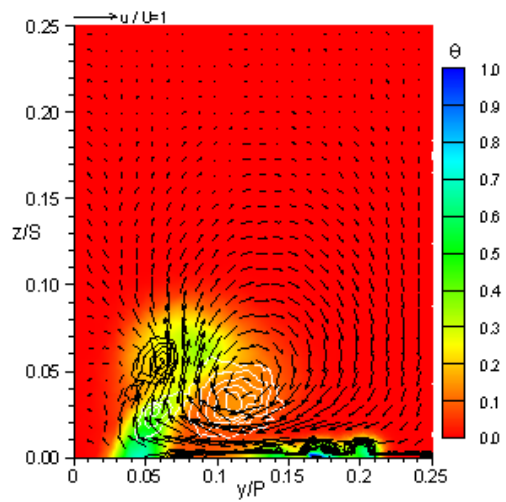
(c) Case #3

Figure C.13: Trial 4 configuration stagnation plane.

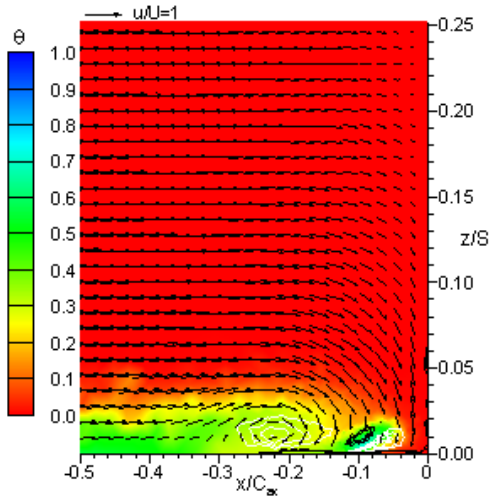
Figure C.14: Trial 4 configuration SS2 plane.



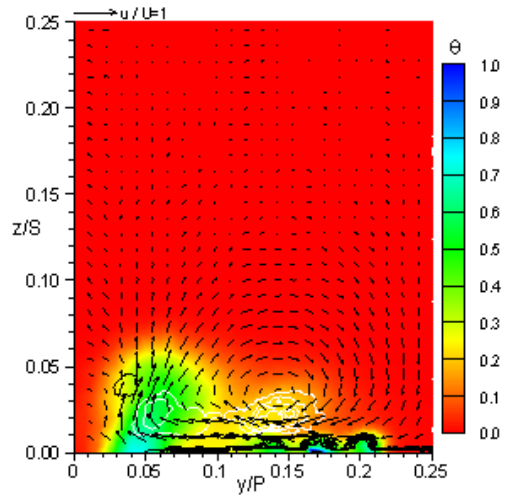
(a) Case #1



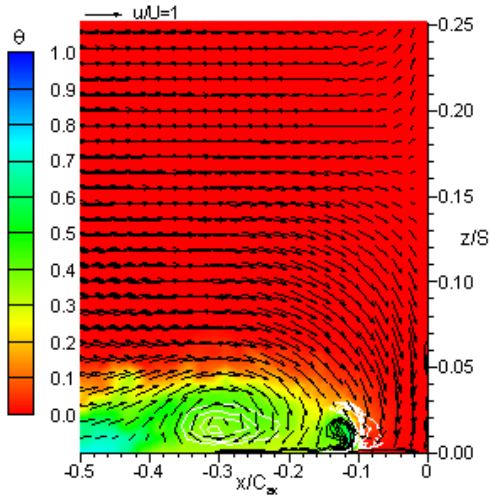
(a) Case #1



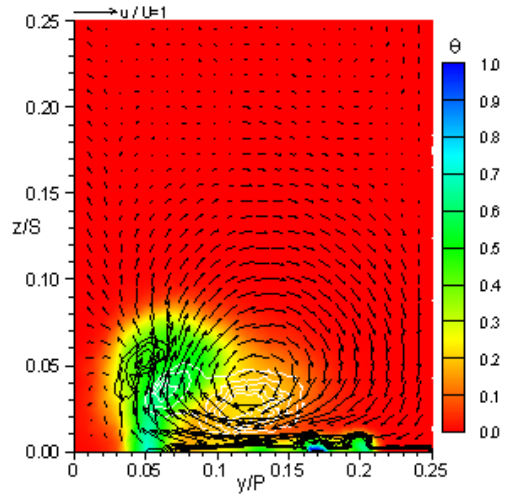
(b) Case #2



(b) Case #2



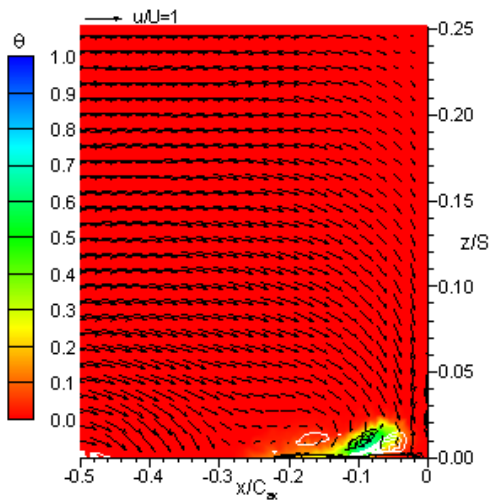
(c) Case #3



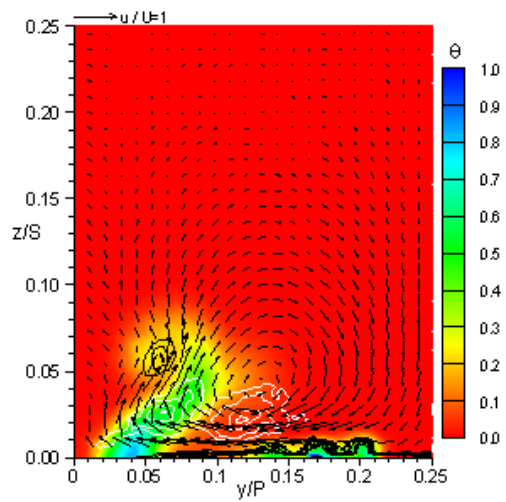
(c) Case #3

Figure C.15: Trial 5 configuration stagnation plane.

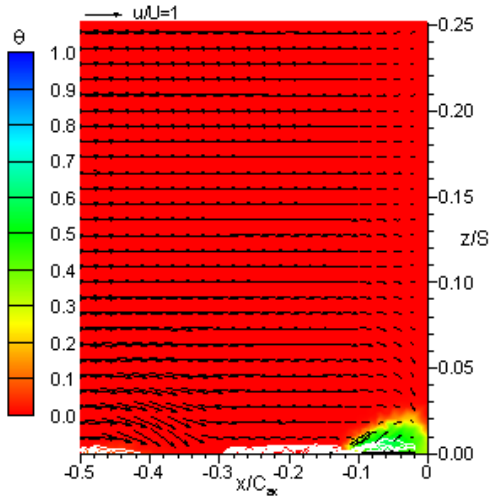
Figure C.16: Trial 5 configuration SS2 plane.



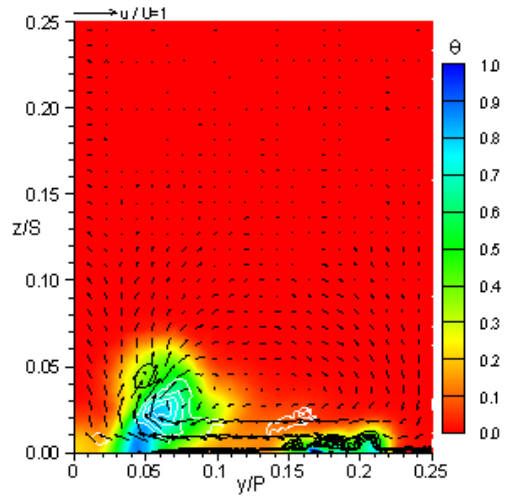
(a) Case #1



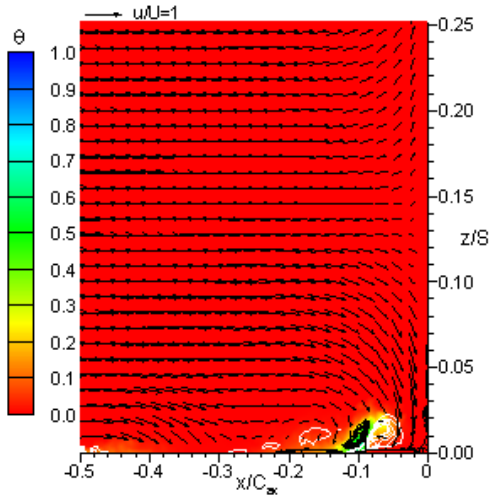
(a) Case #1



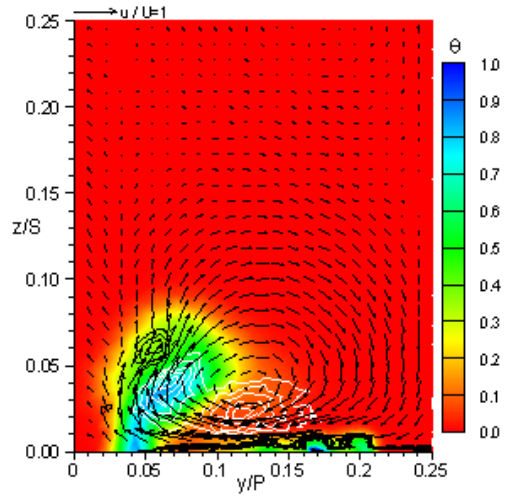
(b) Case #2



(b) Case #2



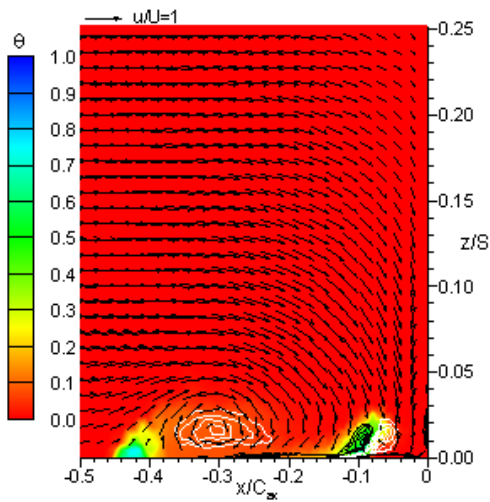
(c) Case #3



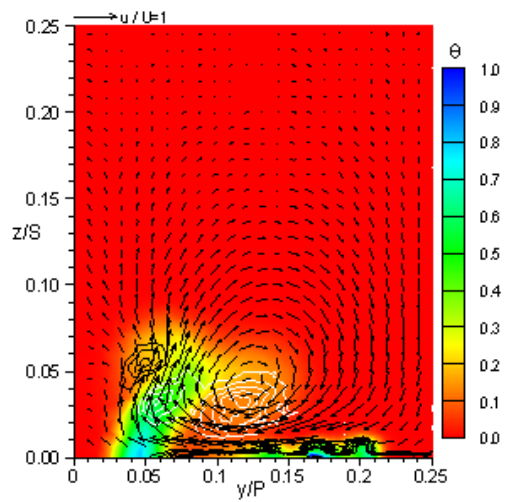
(c) Case #3

Figure C.17: Trial 6 configuration stagnation plane.

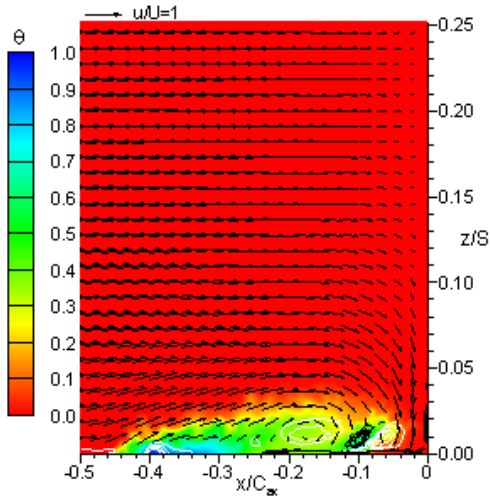
Figure C.18: Trial 6 configuration SS2 plane.



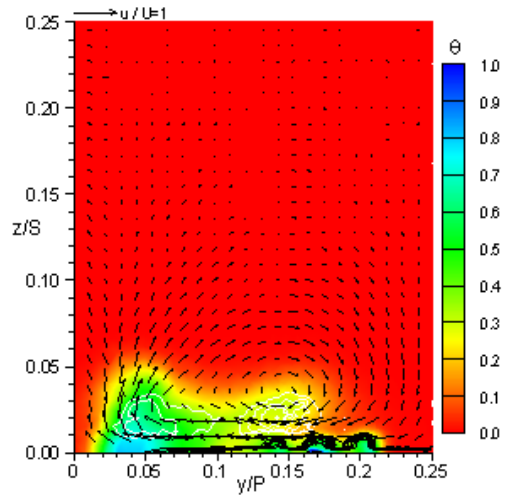
(a) Case #1



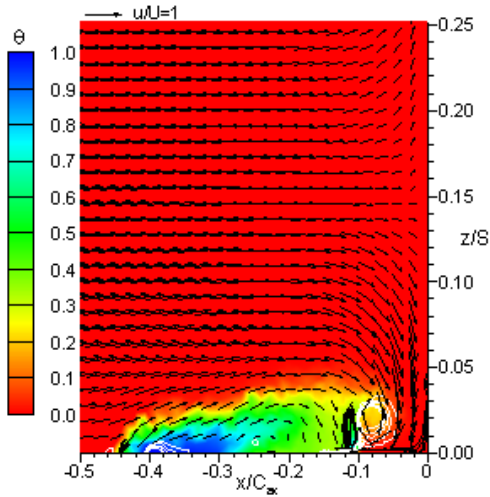
(a) Case #1



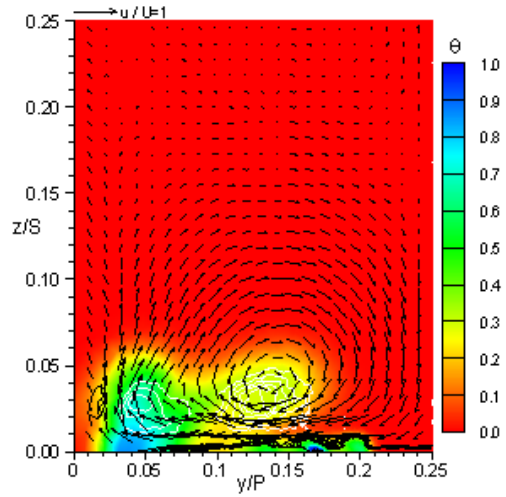
(b) Case #2



(b) Case #2



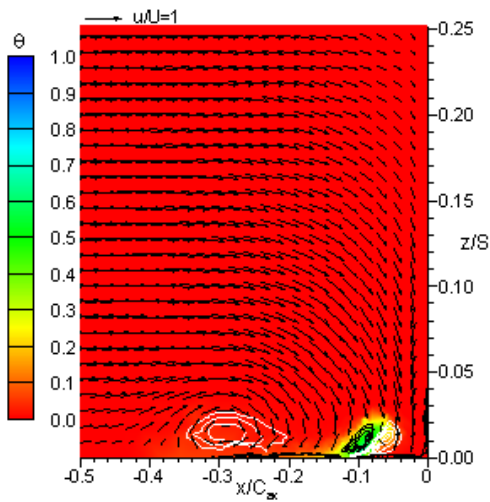
(c) Case #3



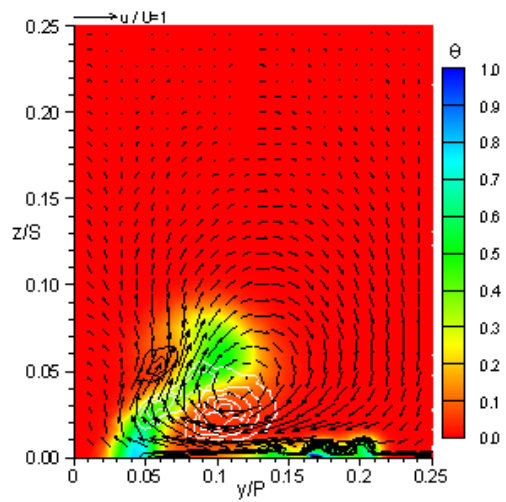
(c) Case #3

Figure C.19: Trial 7 configuration stagnation plane.

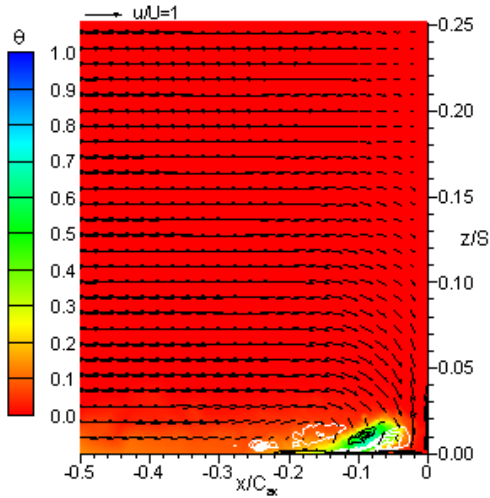
Figure C.20: Trial 7 configuration SS2 plane.



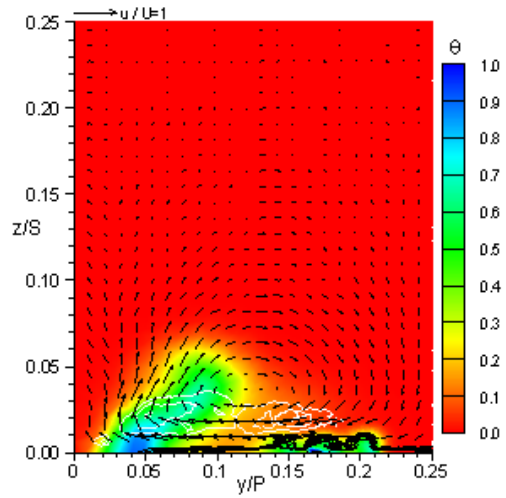
(a) Case #1



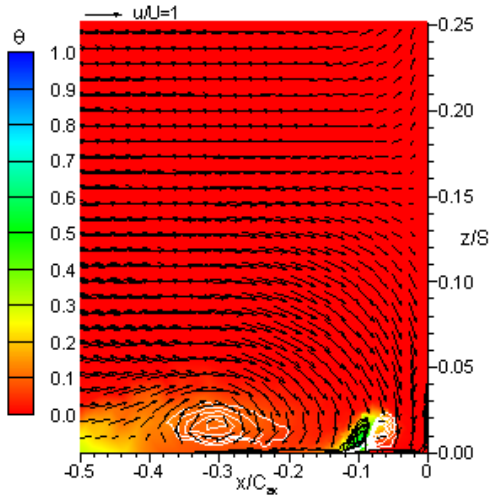
(a) Case #1



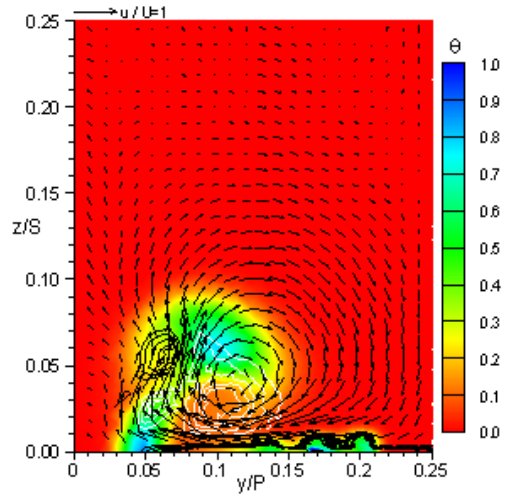
(b) Case #2



(b) Case #2



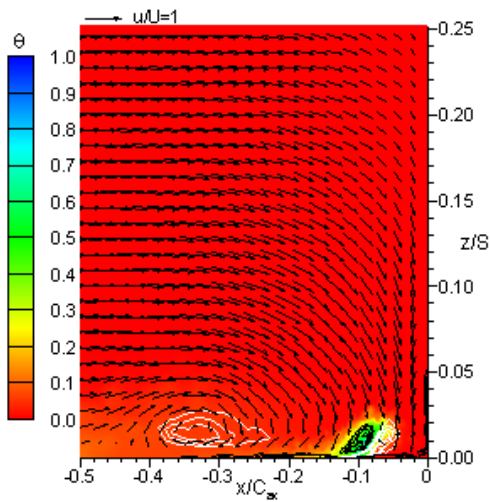
(c) Case #3



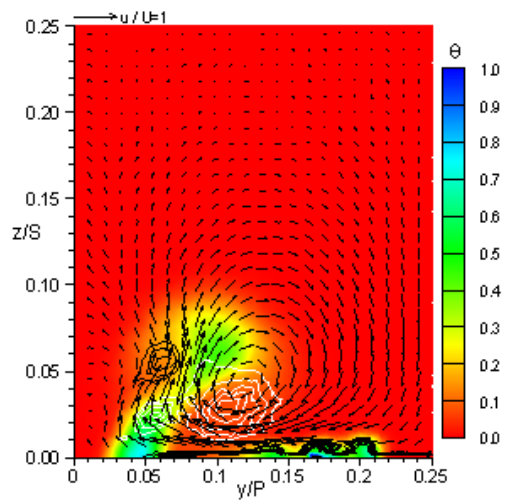
(c) Case #3

Figure C.21: Trial 8 configuration stagnation plane.

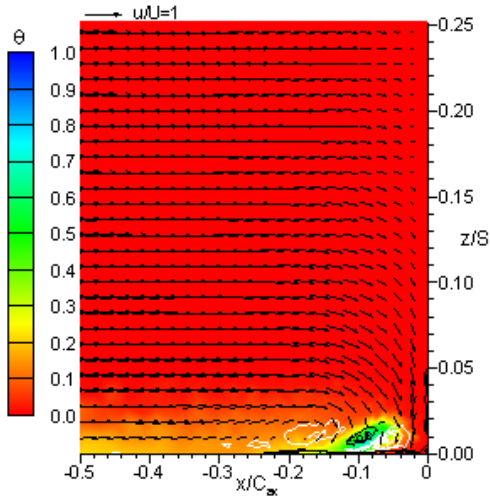
Figure C.22: Trial 8 configuration SS2 plane.



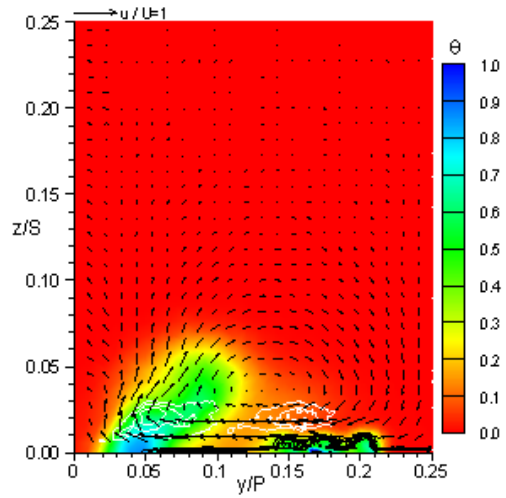
(a) Case #1



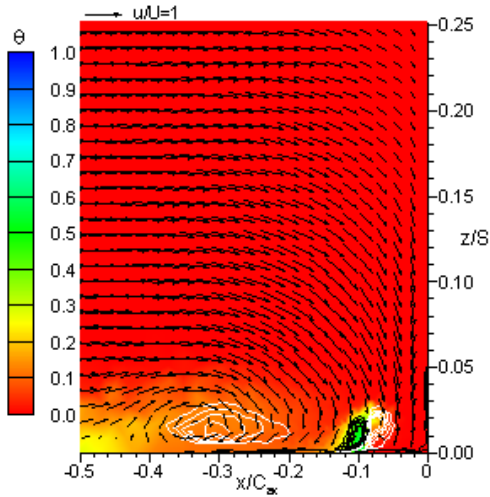
(a) Case #1



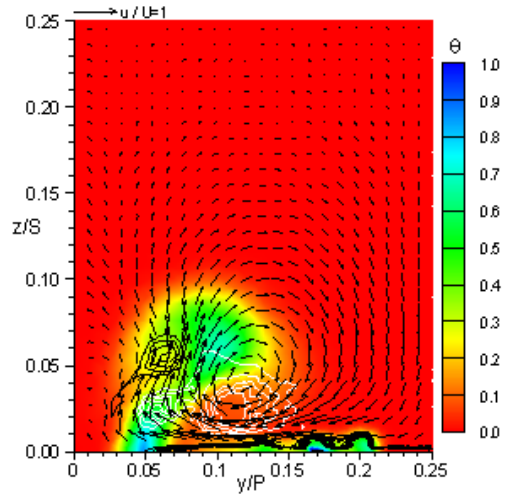
(b) Case #2



(b) Case #2



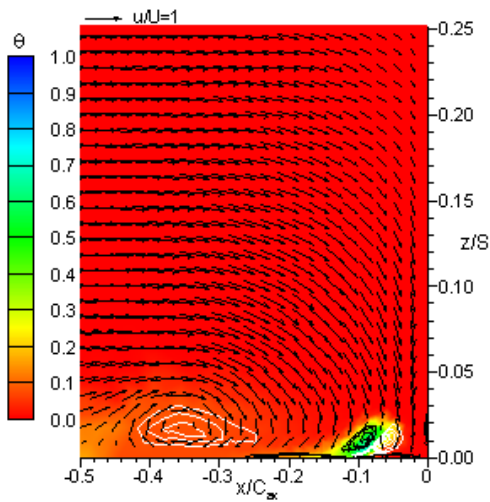
(c) Case #3



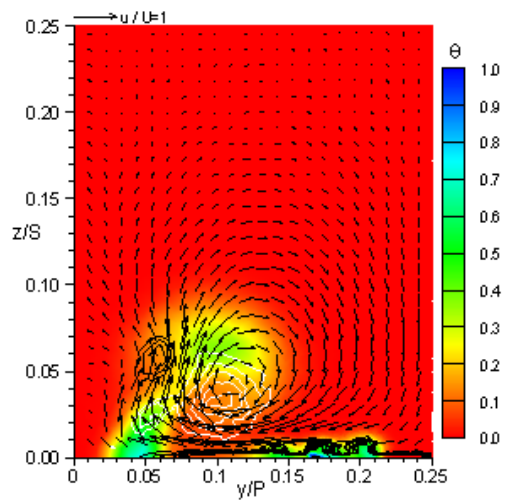
(c) Case #3

Figure C.23: Trial 9 configuration stagnation plane.

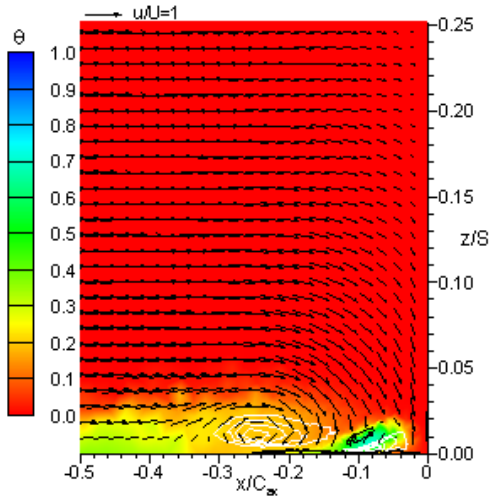
Figure C.24: Trial 9 configuration SS2 plane.



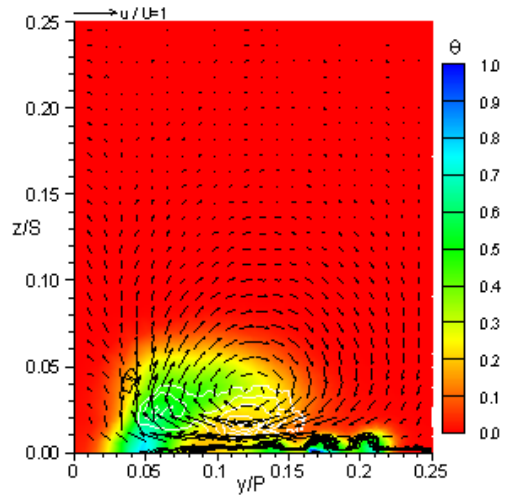
(a) Case #1



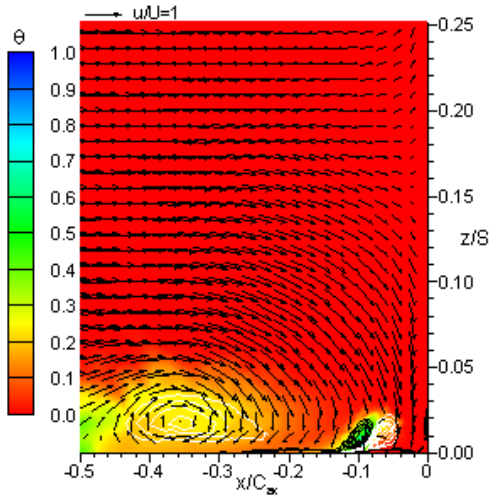
(a) Case #1



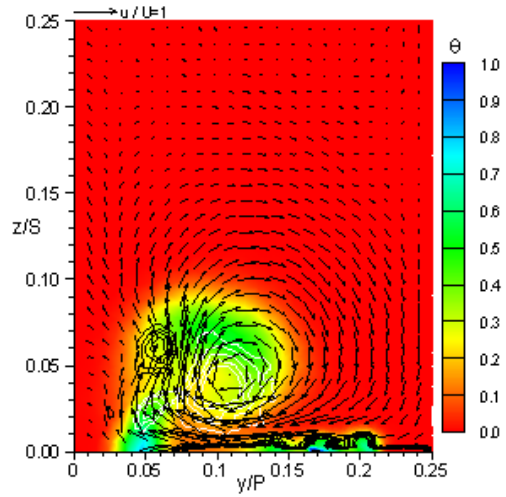
(b) Case #2



(b) Case #2



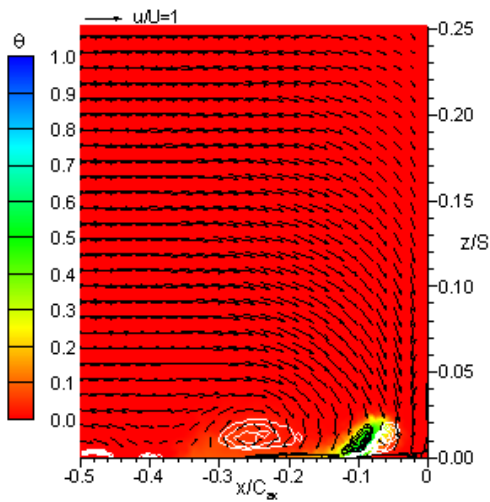
(c) Case #3



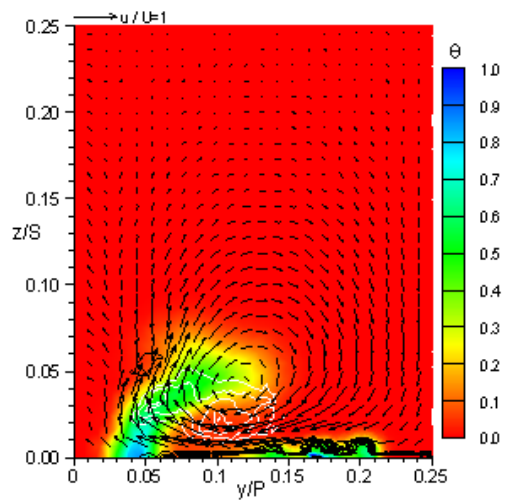
(c) Case #3

Figure C.25: Trial 10 configuration stagnation plane.

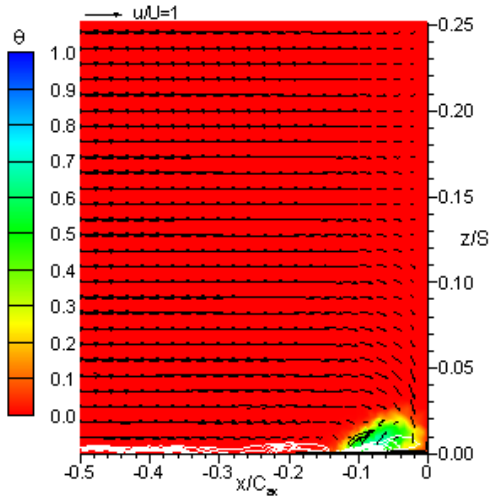
Figure C.26: Trial 10 configuration SS2 plane.



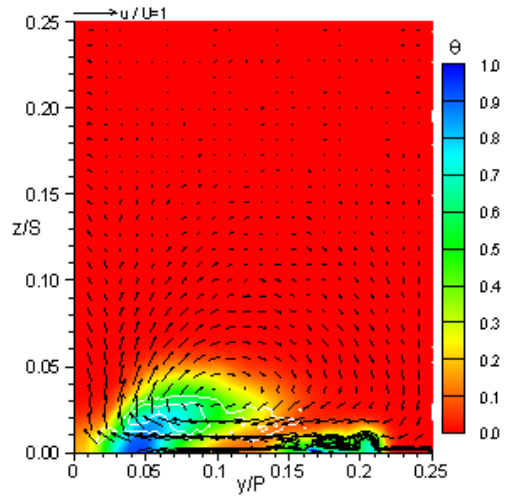
(a) Case #1



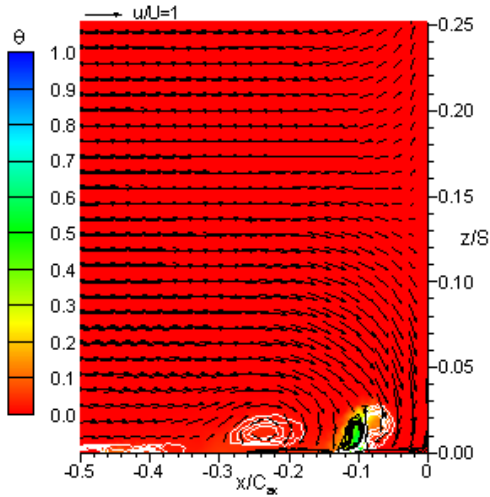
(a) Case #1



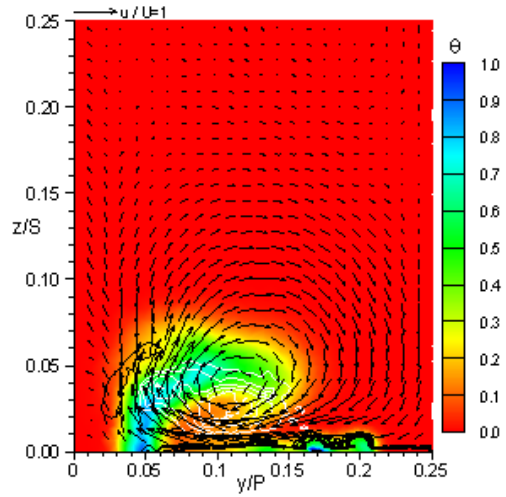
(b) Case #2



(b) Case #2



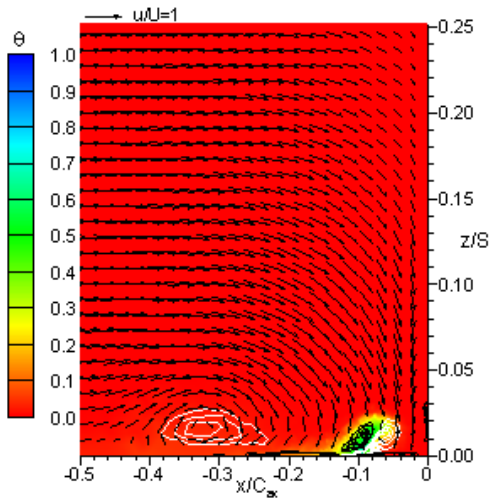
(c) Case #3



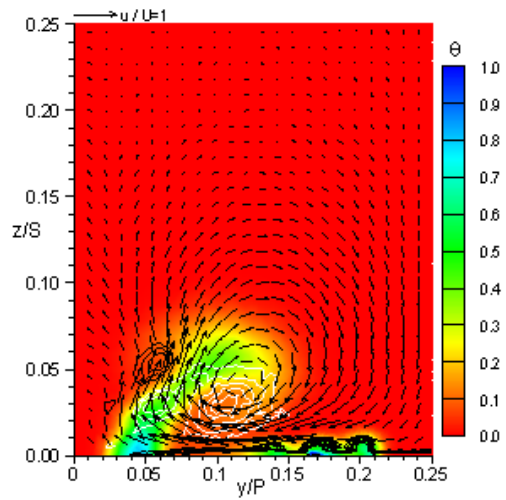
(c) Case #3

Figure C.27: Trial 11 configuration stagnation plane.

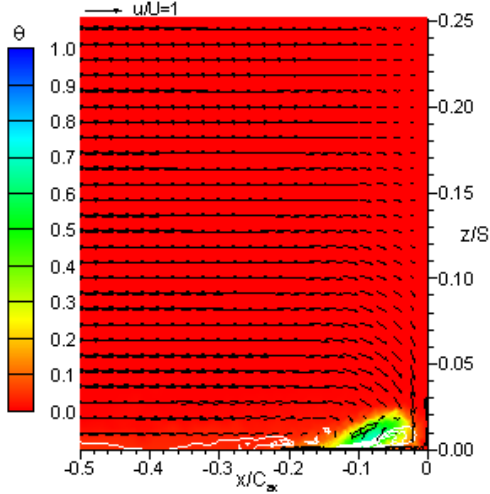
Figure C.28: Trial 11 configuration SS2 plane.



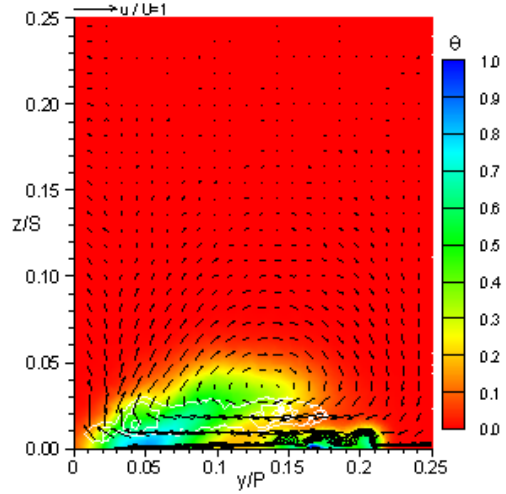
(a) Case #1



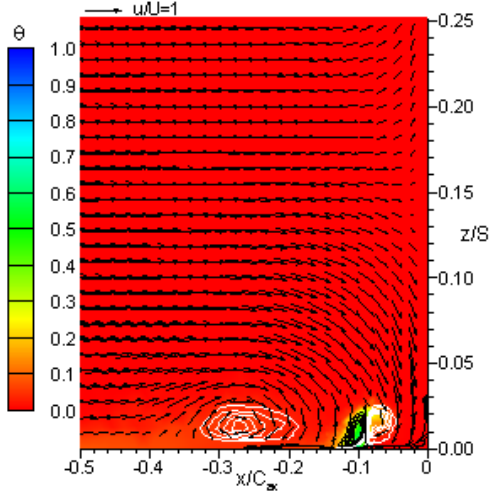
(a) Case #1



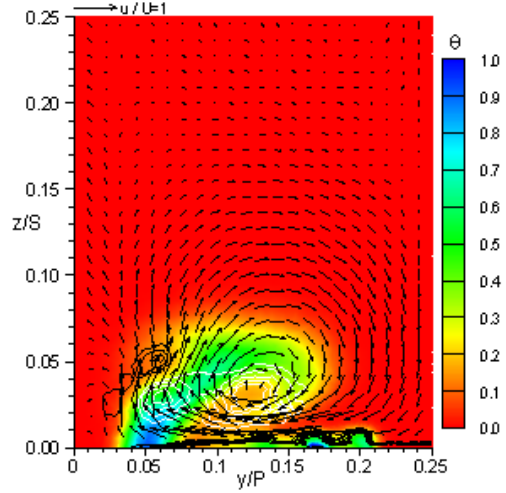
(b) Case #2



(b) Case #2



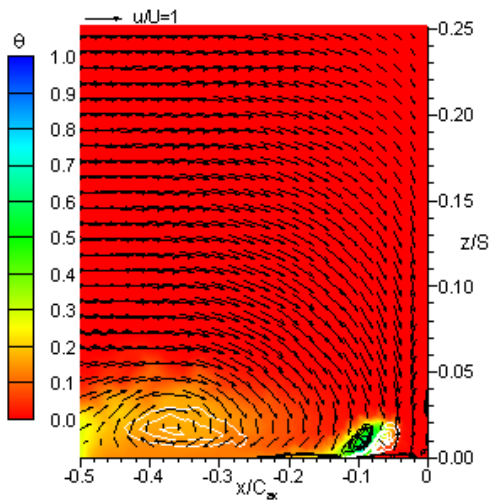
(c) Case #3



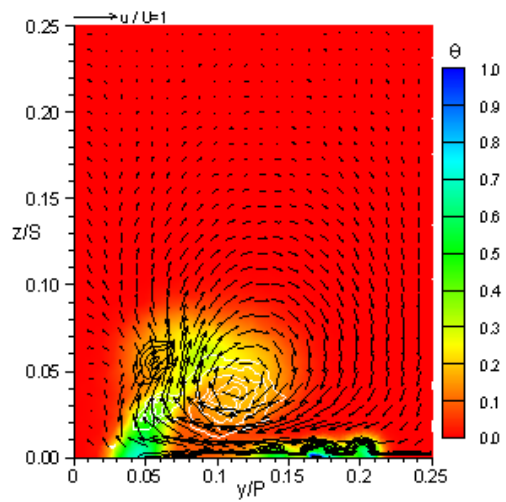
(c) Case #3

Figure C.29: Trial 12 configuration stagnation plane.

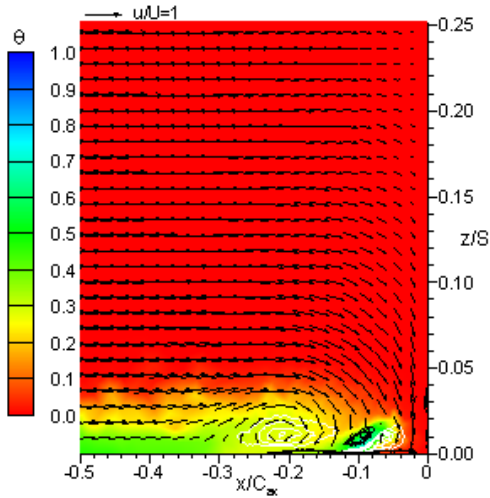
Figure C.30: Trial 12 configuration SS2 plane.



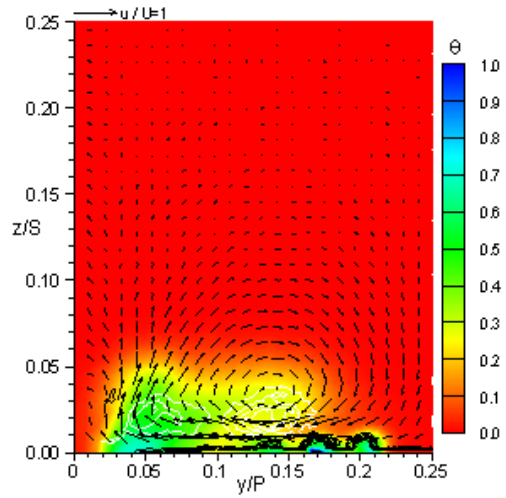
(a) Case #1



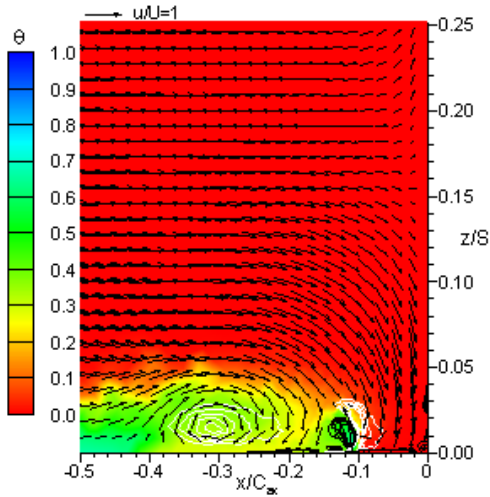
(a) Case #1



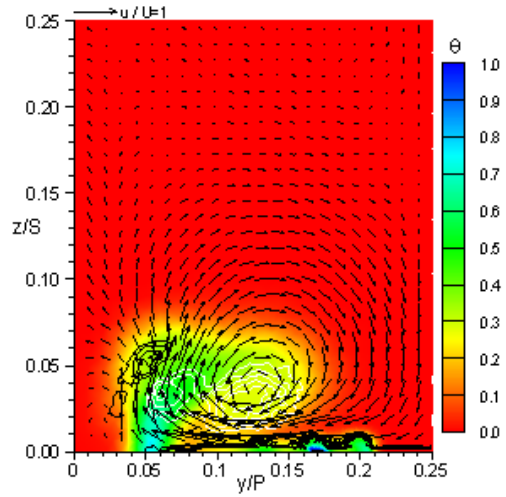
(b) Case #2



(b) Case #2



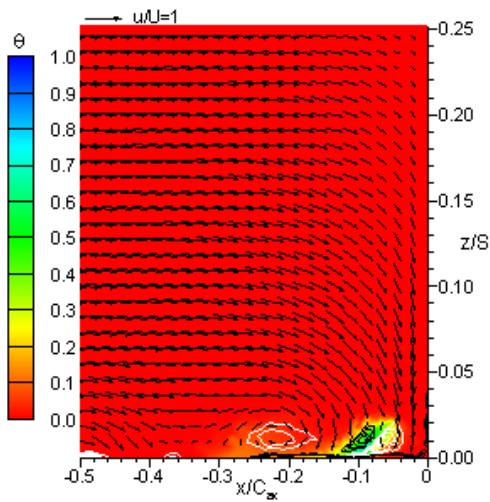
(c) Case #3



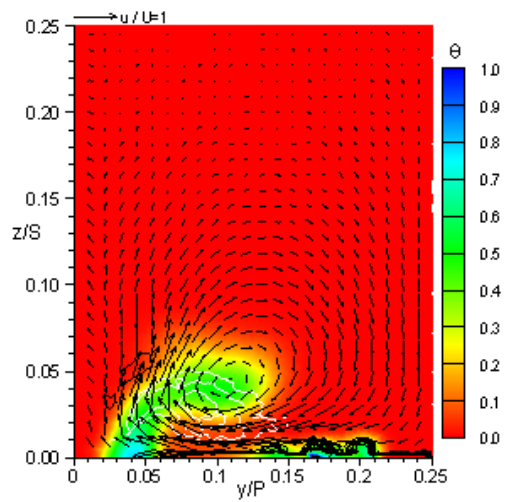
(c) Case #3

Figure C.31: Trial 13 configuration stagnation plane.

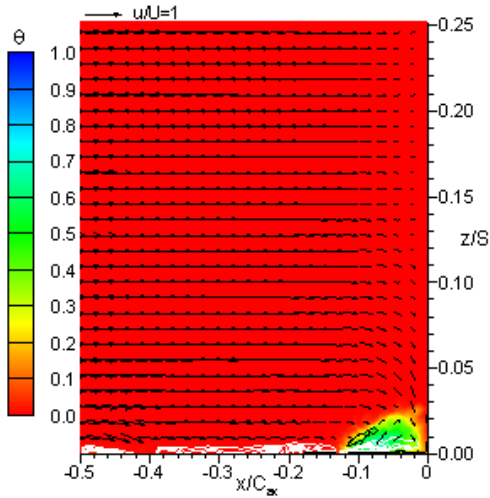
Figure C.32: Trial 13 configuration SS2 plane.



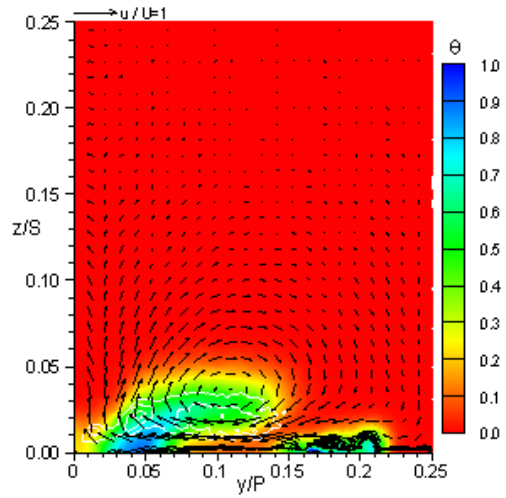
(a) Case #1



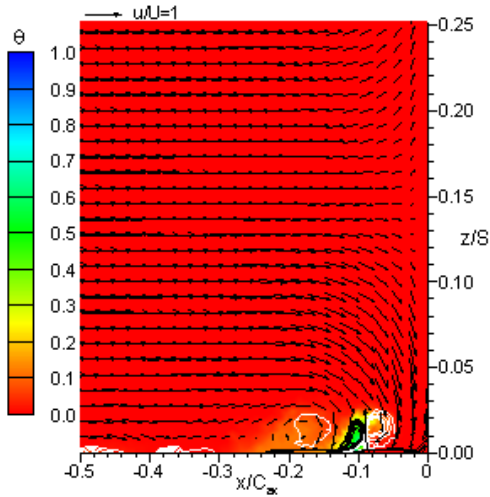
(a) Case #1



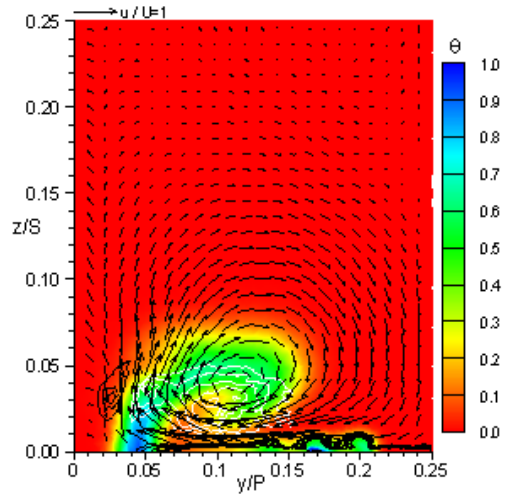
(b) Case #2



(b) Case #2



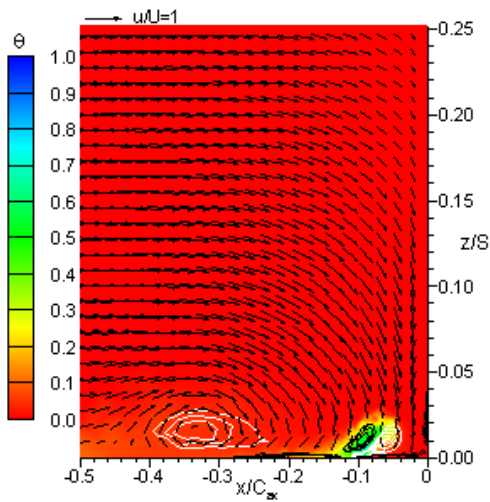
(c) Case #3



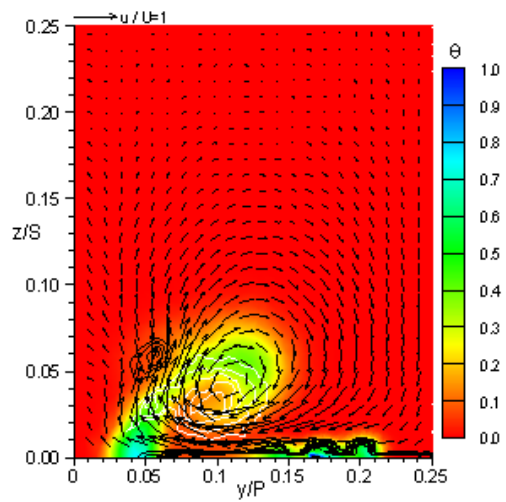
(c) Case #3

Figure C.33: Trial 14 configuration stagnation plane.

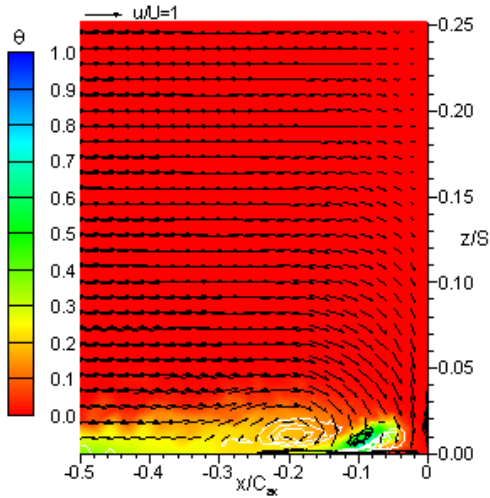
Figure C.34: Trial 14 configuration SS2 plane.



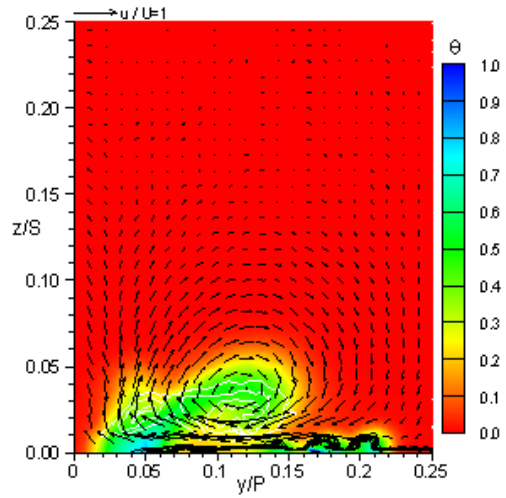
(a) Case #1



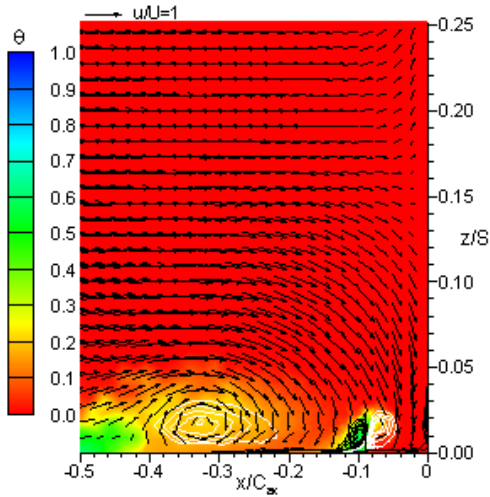
(a) Case #1



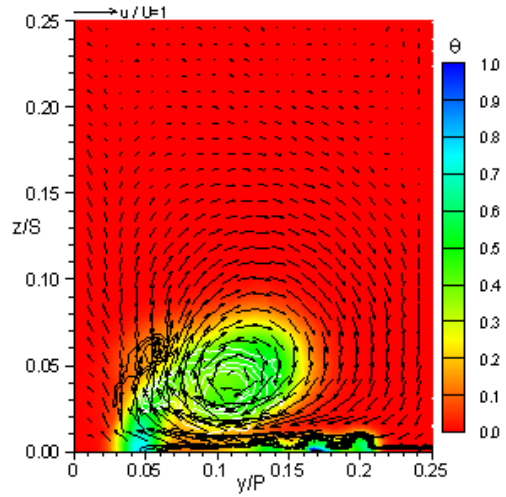
(b) Case #2



(b) Case #2



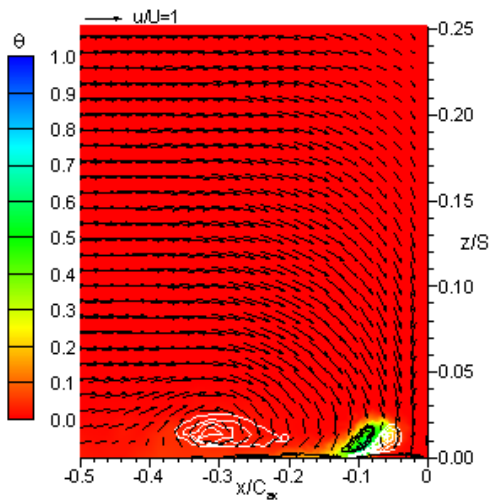
(c) Case #3



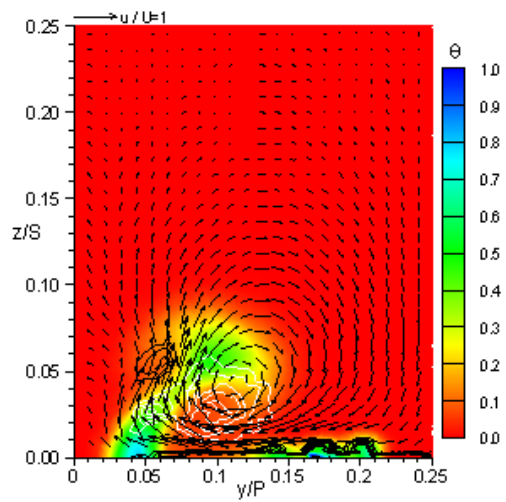
(c) Case #3

Figure C.35: Trial 15 configuration stagnation plane.

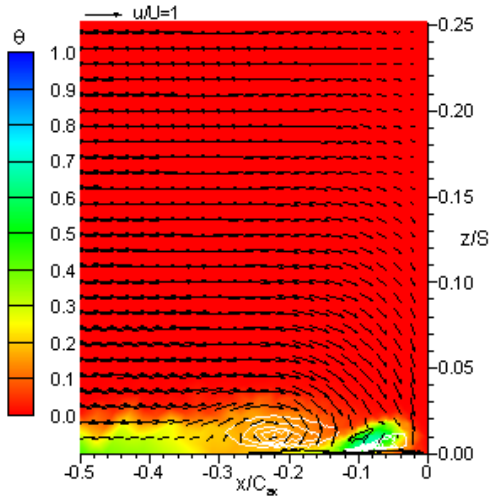
Figure C.36: Trial 15 configuration SS2 plane.



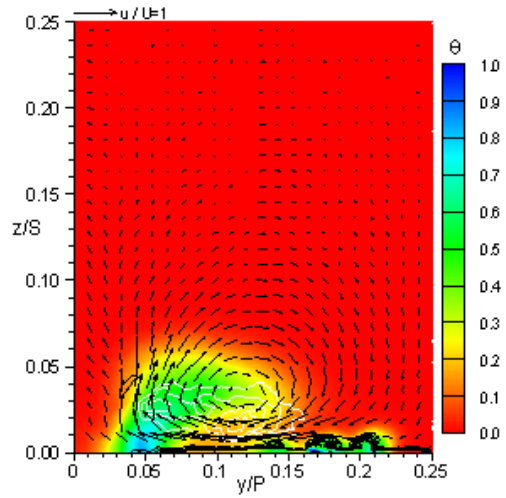
(a) Case #1



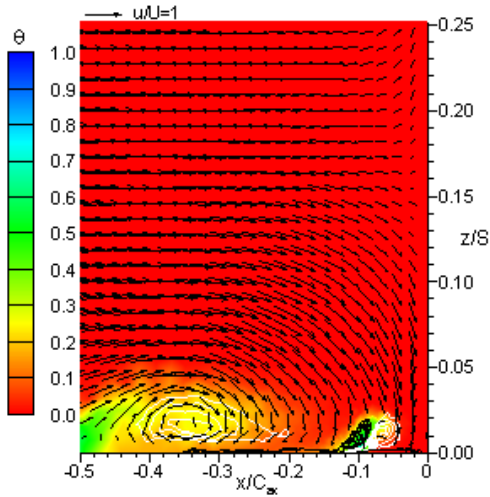
(a) Case #1



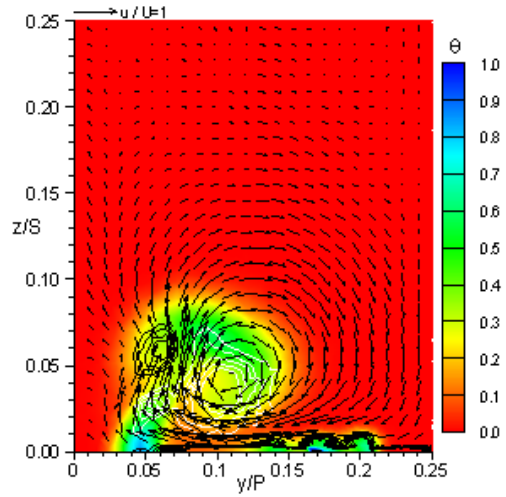
(b) Case #2



(b) Case #2



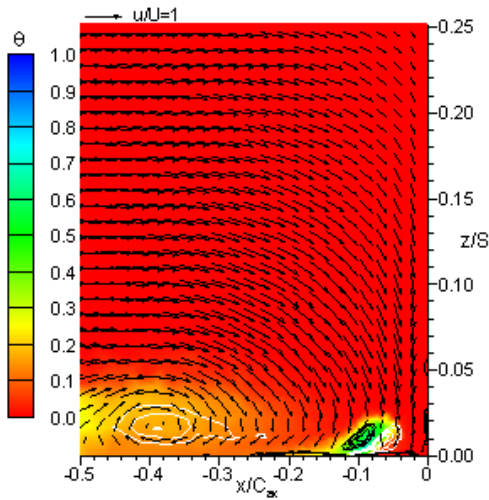
(c) Case #3



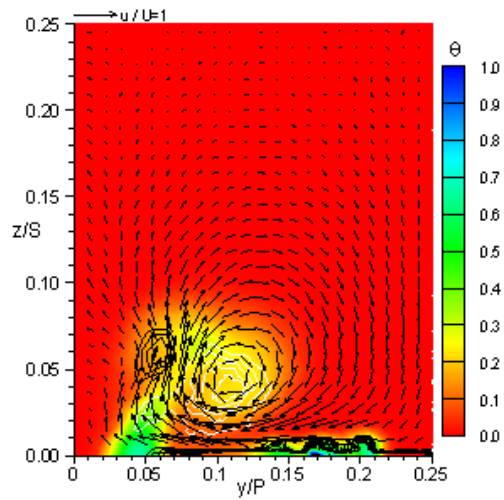
(c) Case #3

Figure C.37: Trial 16 configuration stagnation plane.

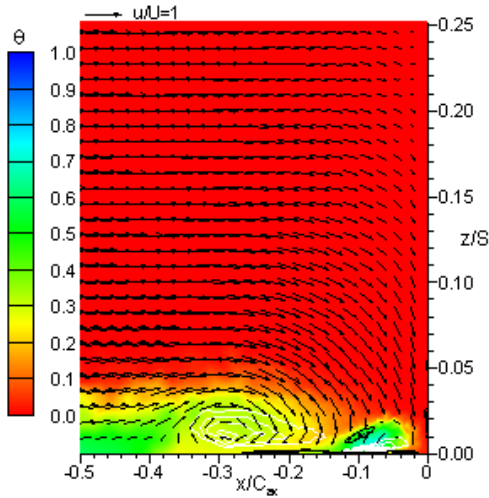
Figure C.38: Trial 16 configuration SS2 plane.



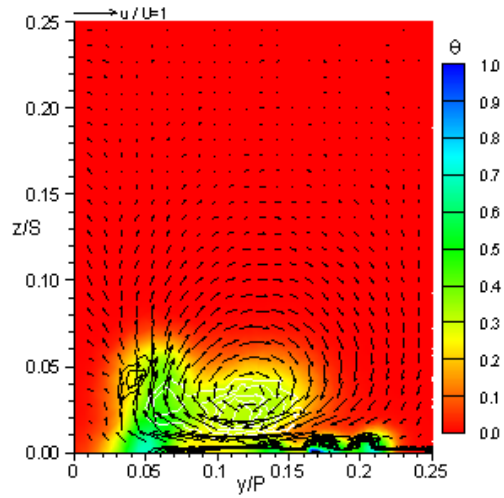
(a) Case #1



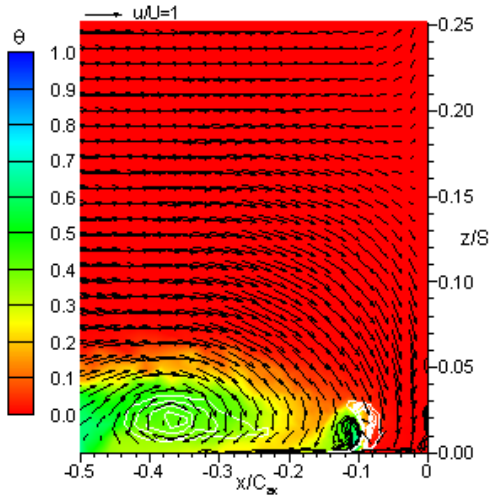
(a) Case #1



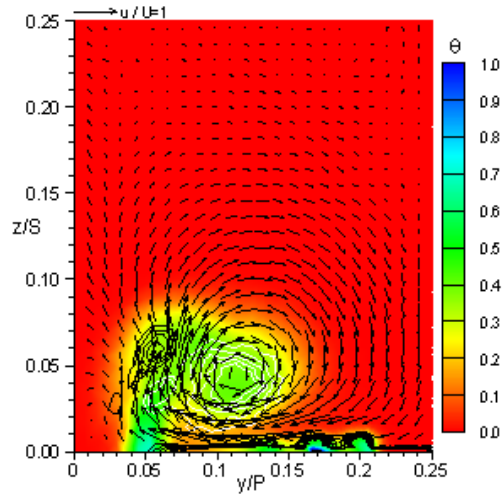
(b) Case #2



(b) Case #2



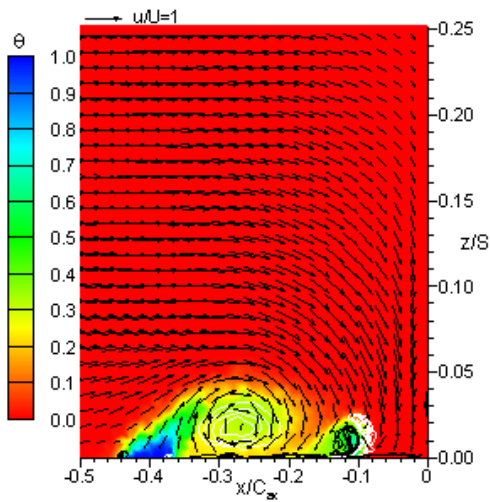
(c) Case #3



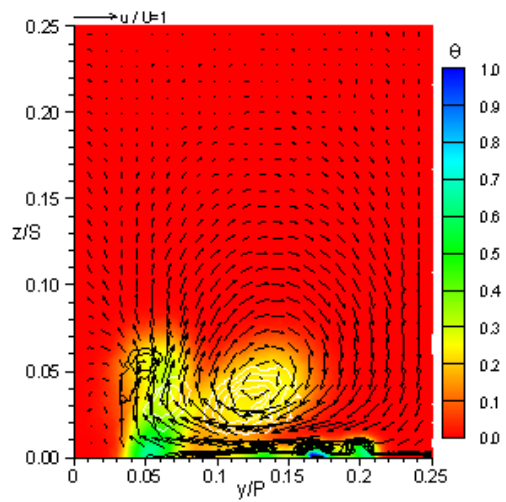
(c) Case #3

Figure C.39: Trial 17 configuration stagnation plane.

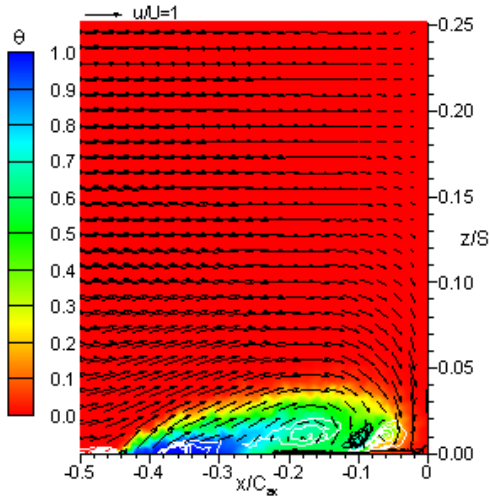
Figure C.40: Trial 17 configuration SS2 plane.



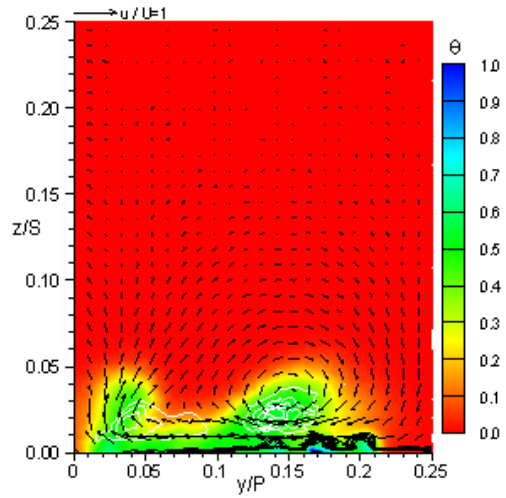
(a) Case #1



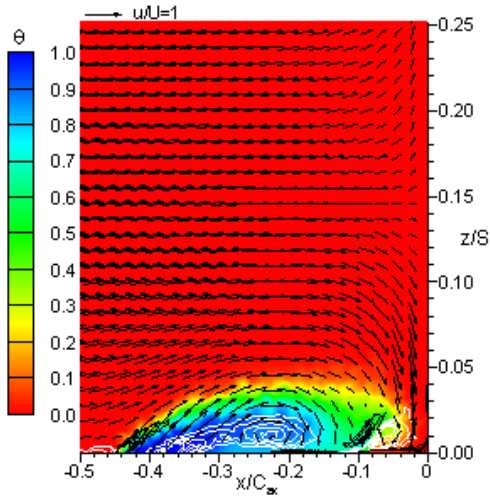
(a) Case #1



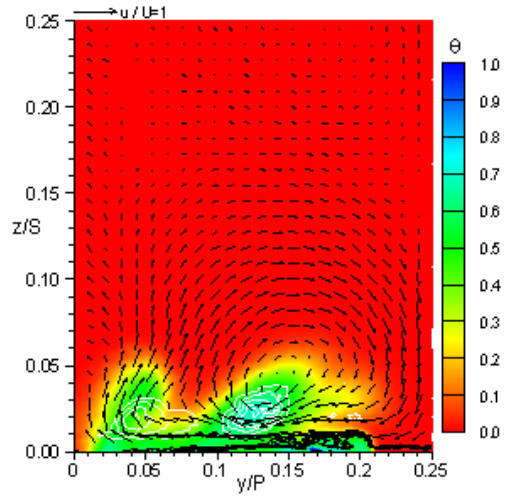
(b) Case #2



(b) Case #2



(c) Case #3



(c) Case #3

Figure C.41: Trial 18 configuration stagnation plane.

Figure C.42: Trial 18 configuration SS2 plane.